Two Particle Angular Correlation Functions of Neutral and Charged Kaons in Pb–Pb collisions at $\sqrt{s_{\mathrm{NN}}} = 5.02$ TeV with ALICE Experiment at the Large Hadron Collider

by
Anjaly Sasikumar Menon

A dissertation submitted to the Department of Physics,

College of Natural Sciences and Mathematics

in partial fulfillment of the requirements for the degree of

Doctor of Philosophy
in Physics

Chair of Committee: Anthony Timmins

Committee Member: Rene Bellwied

Committee Member: Gemunu Gunaratne

Committee Member: Andrew Renshaw

Committee Member: Ricardo Vilalta

University of Houston
August 2024

DEDICATION

This dissertation is dedicated to my family, who are my greatest blessing in life, for their unconditional love, support, and encouragement. Especially to my late grandmother, Narayani Amma, and my parents, Sasikumar and Lalitha Devi, whom I call Acha and Amma. It is with a deep sense of gratitude and accomplishment that I cherish the fact that both my sister (Dr. Arathy S. Menon) and I (Dr. Anjaly S. Menon) hold the title of doctor—she as a medical doctor and I as a Ph.D. To Acha and Amma, I am proud of everything we have achieved as your daughters and thank you for making all this possible.

ACKNOWLEDGMENTS

This Ph.D. journey would not have been the same without the support, guidance and companionship of many individuals. I would like to take this opportunity to express my heartfelt gratitude to all those who have contributed to the successful completion of my Ph.D.

Firstly, I would like to express my deepest gratitude to my advisor, Dr. Anthony Timmins, for his unwavering support and encouragement throughout this time. His kindness and insights have been invaluable. He is hte coolest advisor one can ask for. I am also profoundly thankful to Dr. Rene Bellwied, a great teacher and an exceptional experimental physicist. I would like to thank him for always being available and for the many discussions we've had. His experience, advice and constructive feedback have significantly shaped my research and academic growth.

I am also extremely thankful to Dr. Malgorzata Janik and Daniela Ruggiano, who provided immense support and guidance, helping me to achieve promising results. I would like to extend my sincere thanks to the members of my dissertation committee, Dr. Gunaratne, Dr. Renshaw and Dr. Vilalta for their insightful comments, constructive criticisms, and the time they have devoted to reviewing my research over the past years. A special mention goes to Dr. Gunaratne for his guidance and contributions to the completion of my dissertation. I would also like to thank Dr. Claudia Ratti - an amazing theoretical physicist. I thank her for her support during this journey, especially during my time with the Women in Physics Society at University of Houston (WiPS-UH).

Thank you to CERN and for all the facilities provided. Thanks to members of ALICE collaboration and conveners of PWGs who helped me for progressing with the analysis. Special thanks to Mesut and Lucia for all their help during the approval of my results. I also thank my advisors for giving me the opportunity to travel to various conferences. Those experiences have been invaluable, both academically and personally. The opportunities to

visit CERN in years 2022 and 2023 and assist in data collection were academically fruitful and exciting, adding a significant chapter to this journey.

I am extremely thankful for the friends I have made since arriving in Houston. Despite being very attached to my home in Kerala, I never felt lonely, even during those first few days in a new city, thanks to the friends I made. I want to thank Trevor for his friendship and for giving a sense of home in Houston. I would also like to thank Bikash, who has been my honest critic at all times. Thanks to Angel, who introduced me to many cool things and places in Houston. Also, special mention to Oveis, Lilly, Tony(& Kristena), Pablo(& Evelyn), Joaquin, Francesco and Sumit, who made graduate school fun. A very special appreciation to Sasi and Co. team (whom I have known since my initial days here and are like a family to me) for their amazing friendship, all the fun times, and for always being there when I needed them. Playing badminton with you guys has been a great stress-reliever. Thanks to Tania, with whom I became close friends and gym buddies during the last year. I want to thank Aranya, for his friendship and support during the last few months of my Ph.D. I thank Rutik, who was also my junior during undergraduate studies in India and is now a member of Houston group. Continuing our senior-junior relationship to being roommates has been great along with Navmi, a sweet friend I made at UH. Thanks to Viswa and Vivek, who were my good friends in Houston and continue to be friends, even though they are no longer in Houston. Thanks to Fidha, I remember the wonderful time we spent in Chicago, 3 years ago; it felt like a therapeutic trip to me. Thanks to Ashfia, who also defended in the same month as me and was my first roommate in Houston. Thanks to Kaberi aunty, who is a motherly figure to me while in Houston.

The most support I received while in Houston came all the way from India. I want to thank Neeli, my best friend with whom I share my deepest secrets and more than a decade of cherished memories. I thank Athu, my elder cousin, and Geethu, my little cousin, for the beautiful bond we share and the memories we have created since childhood. I am grateful

for all the love and care you have given me. I also remember my relatives and neighbors in Kerala who always visited me with love and, especially, with delicious food every time I left for Houston. I thank all my teachers who have taught me from childhood to my undergraduate studies in IISER Mohali. The knowledge and experiences you have given me are invaluable.

Lastly but not the least, my deepest appreciation goes to my family, who have provided endless love, support, and patience, to whom this dissertation is dedicated. Their sacrifices have been the foundation of all my achievements throughout this journey, and I hope to have made them proud. Words are not enough to describe the bond I share with my sister, Chinnu. I am very blessed to have her as my sister and extremely proud of her achievements in her career.

Finally, I would like to thank the author of this dissertation -myself- for the dedication and hard work that went into completing this document. Reflecting on both my academic and personal growth over the six years of my Ph.D. journey, I recognize that this experience has been both challenging and rewarding at the same time. My commitment to constant learning, growing, and pushing the boundaries of my knowledge and skills have been the key. This journey has taught me the importance of self-belief, Perseverance and maintaining a positive mindset even in the face of challenges. I am proud of the progress I have made and cherish the lessons learned along the way.

To conclude, I acknowledge the authorized use of copyrighted materials in this dissertation and express my gratitude to the Department of Energy for their grant support.

ABSTRACT

In ultra-relativistic heavy-ion collisions, hadronic matter undergoes transition to a deconfined phase of quarks and gluons, a state of matter widely known as Quark-Gluon Plasma (QGP). It is believed that the universe existed in this new state of matter microseconds after the Big Bang. The QGP state is transient, undergoing collective expansion and eventually hadronizing. Phase transitions in Quantum Chromodynamics (QCD) are also realized in terms of chiral symmetry breaking/restoration. In the confined hadronic phase, chiral symmetry is broken and it is expected to be restored in the deconfined QGP phase. This was verified by Lattice QCD calculations at finite temperatures and zero densities. There have been several experimental evidences for the deconfinement phase transition while the chiral phase transition remains as a mystery for high energy physicists. Observing signals of chiral phase transition is as fundamental a feature of QCD as quark or color confinement and asymptotic freedom.

Recent ALICE measurements have demonstrated large dynamical correlations between produced neutral and charged kaons in Pb–Pb collisions at $\sqrt{s_{\mathrm{NN}}} = 2.76$ TeV. These integrated correlations cannot be described by conventional heavy-ion models, such as HIJING, EPOS-LHC and AMPT; however, they can only be explained by invoking the presence of a condensate. Two candidates for such a condensate are the Disoriented Chiral Condensate (DCC) and Disoriented Isospin Condensate (DIC). They both arise from chiral symmetry restoration in the QGP, which breaks during the phase transition to form a condensate that coherently emits hadrons. To further investigate these anomalous kaon correlations, a differential measurement of two-particle angular correlation functions of charged and neutral kaons as a function of $\Delta\varphi$ and $\Delta\eta$ in Pb–Pb collisions at $\sqrt{s_{\mathrm{NN}}} = 5.02$ TeV is performed in this dissertation. The correlations involving oppositely charged kaons were computed as a baseline. These experimental correlations were then compared with HIJING and AMPT model predictions to determine if the angular correlations exhibited any anomalous behavior.

TABLE OF CONTENTS

LIST OF TABLES

LIST OF FIGURES

Chapter 1

Introduction

1.1 Introduction to Nuclear and Particle Physics

The concept of atomic nucleus as the central core of every atom was first articulated by Ernest Rutherford, marking a pivotal discovery in the field of nuclear physics [1], [2]. This revelation led to a fundamental question: What are these nuclei composed of? Upon closer examination at a more fundamental level, a new type of substructure emerges. It is now well established that atomic nuclei are composed of electrically positive protons and electrically neutral neutrons, collectively known as nucleons. These nucleons are bound together by the nuclear force, the strongest of the fundamental forces. The stability of the nucleus, despite the electrostatic repulsion among the positively charged protons, poses a central question in nuclear physics. The answer lies in the strong nuclear force—an attractive force between nucleons that dominates at short distances and is sufficiently powerful to overcome the electrostatic force between protons. This intricate balance ensures the stability of the atomic nucleus. Further deepening our understanding, the deep inelastic scattering experiments confirmed that protons and neutrons themselves consist of even smaller components called quarks, adding another layer to our understanding of nuclear structure [3].

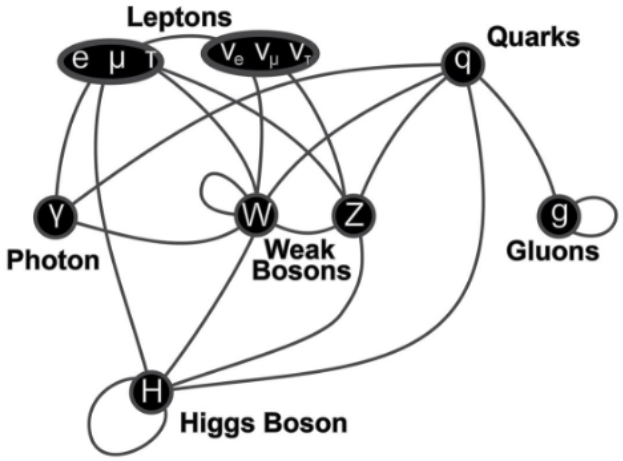

Figure 1.1: A diagram summarizing the tree-level interactions between elementary particles described in the Standard Model. The vertices represent types of particles, and arcs connecting them represent interactions that can take place.

There are four fundamental forces in nature which are strong nuclear force, electromagnetic force, weak nuclear force and gravitational force. As mentioned, the strong nuclear force is the strongest among these. The electromagnetic force governs everything from the orbiting of electrons around the nucleus to the principles of electronics and electromagnetism at macroscopic scales. The Weak Nuclear Force plays a crucial role in radioactive decay and nuclear fission. This force is pivotal in processes that power the sun, providing vital energy for life on Earth. The Gravitational Force, though weak compared to its peers at the particle scale, exerts a profound influence across the cosmos, governing the structure and dynamics of the universe itself, from planetary orbits to the motion of galaxies. The relative strength, range and exchange particles of these four forces are given in the Table 1.1.

Table 1.1: Comparison of the four fundamental forces in nature in terms of strength of interaction, range, and exchange particles involved.

Force	**Relative Strength**	**Range**	**Exchange Particle**
Strong Nuclear Force	1	$\sim 10^{-15}$ meters	Gluons
Electromagnetic Force	$\sim 10^{-2}$	Infinite	Photons
Weak Nuclear Force	$\sim 10^{-13}$	$\sim 10^{-18}$ meters	W and Z Bosons
Gravitational Force	$\sim 10^{-42}$	Infinite	Gravitons (hypothetical)

Nuclear physics and particle physics, introduced in the paragraphs above, were not distinct disciplines 70 years ago. Nuclear physics explores the structures of atomic nuclei, the behavior of finite quantum systems, and the interactions of nucleons. In contrast, particle physics delves into more fundamental and exotic interactions at the subatomic level, often referred to as high-energy physics because understanding the structure of matter at the level of elementary particles requires experiments at extremely high energies. The distinction became more pronounced in 1964 when Murray Gell-Mann and George Zweig independently proposed, while studying the symmetry in strong interactions, that nucleons have an inner structure best described by constituent particles called "quarks," a term coined by Gell-Mann. The physical existence of quarks was later supported by deep inelastic scattering experiments at SLAC (Stanford Linear Accelerator Center) in 1968. These findings are encapsulated in the Standard Model of particle physics, which integrates all four fundamental forces and classifies all elementary particles but does not account for gravity. The model has evolved through the collaborative efforts of numerous scientists worldwide and was solidified in the mid-1970s following experimental validation of quarks. A diagram summarizing the tree-level interactions between elementary particles described in the Standard Model is given in Fig. 1.1.

The Higgs boson, a cornerstone of the Standard Model, is a massive scalar boson with zero spin, positive parity, no electric charge, and no color charge, interacting predominantly with mass. Its existence, predicted to explain why particles have mass, was confirmed in 2012 by the ATLAS and CMS experiments at the Large Hadron Collider (LHC) at CERN [4]. This discovery, following a four-decade search, alongside the identification of the top quark in 1995 [5], the tau neutrino in 2000 [6], and the aforementioned Higgs boson, significantly reinforced the Standard Model. Peter Higgs and François Englert received the 2013 Nobel Prize in Physics for their theoretical predictions.

The elementary particles in the Standard Model are categorized into fermions and bosons,

with four types of gauge bosons mediating forces: photons (electromagnetic interaction), W and Z bosons (weak interaction), and gluons (strong interaction). The hypothesized gravitons intended to mediate gravitational forces remain unconfirmed. Our focus is on the theory of strong interactions known as QCD or Quantum Chromodynamics, described in the next section.

1.2 Theory of Strong Interactions

1.2.1 QCD Vs. QED

Quantum Chromodynamics (QCD) was initially developed analogously to Quantum Electrodynamics (QED), the well-established theory of electromagnetic interactions, which is robustly supported by experimental evidence. The mediators of the strong force in QCD are gluons, similar to photons in QED and the concept of color in QCD is analogous to the electric charge in QED. Additionally, QCD is characterized by its SU(3) symmetry, reflecting the interactions among the three colors of quarks and gluons. Analogously, QED is characterized by its U(1) symmetry, which governs the interactions of electric charges mediated by photons. The Lagrangian density in QCD can be expressed as:

$$\mathcal{L} = -\frac{1}{4} G_a^{\mu\nu} G^a_{\mu\nu} + \sum_{\text{flavours}} \bar{q}_i (i\gamma^\mu D_\mu - m) q_i \tag{1.1}$$

$$D_\mu = \partial_\mu - ig\frac{\lambda_a}{2} A^a_\mu(x), \tag{1.2}$$

$$G^a_{\mu\nu}(x) = \partial_\mu A^a_\nu(x) - \partial_\nu A^a_\mu(x) + f_{abc} A^b_\mu(x) A^c_\nu(x), \tag{1.3}$$

where f_{abc} represents the structure constants of the SU(3) group, λ_a are the Gell-Mann matrices, and $A^a_\mu(x)$ denotes the eight gluon fields that mediate the strong force. In comparison,

the Lagrangian density for QED can be expressed as:

$$\mathcal{L}_{\text{QED}} = -\frac{1}{4}F_{\mu\nu}F^{\mu\nu} + \bar{\psi}(i\gamma^{\mu}\partial_{\mu} - e\gamma^{\mu}A_{\mu} - m)\psi$$

$$F_{\mu\nu} = \partial_{\mu}A_{\nu} - \partial_{\nu}A_{\mu}$$

where $F_{\mu\nu}$ is the electromagnetic field strength tensor, A_{μ} is the photon field, and e is the electric charge. In QCD, the fundamental constituents are the spin-$\frac{1}{2}$ quarks and the spin-1 gluons. Quarks come in six flavors and interact via the exchange of gluons. Unlike QED, which is an Abelian gauge theory with commutative gauge group elements and features only two types of charges (positive and negative), QCD's gauge group elements are non-commutative. This non-Abelian nature leads to the unique property of gluon self-interaction, attributed to the color charge carried by the gluons themselves. Even though gluons are massless and thus would imply a long-range force, their self-interactions and other properties result in the strong force being very short-ranged.

1.2.2 Cornell Potential in QCD

The interaction potential between a quark and an antiquark, known as the Cornell potential in QCD, comprises two terms reflecting both the short-range behavior mediated by gluon exchange and a confining long-range term, highlighting the dual aspects of the strong force.

$$V(r) = -\frac{4}{3}\frac{\alpha_s}{r} + kr. \tag{1.4}$$

The Coulomb potential ($\propto \frac{1}{r}$) dominates at small distance r whereas the linear term is responsible for the confinement. The linear term is also responsible for the production of mesons and baryons. The properties of QCD can be understood by studying the Strong

interaction coupling constant given by,

$$\alpha_s(Q^2) = \frac{4\pi}{(11 - 2n_f/3)\ln(Q^2/\Lambda^2)} \tag{1.5}$$

where Q^2 is the momentum transfer, n_f is the number of quark flavours, and Λ is a scaling parameter. The logarithmic decrease of strong coupling constant, $\alpha_s(Q^2)$ as a function of momentum transfer is depicted in Fig. 1.2. The diagram shows the agreement between the QCD predictions with various experiments. For large values of Q^2, the coupling $\alpha_s(Q^2) \to 0$. This phenomenon at large Q^2 is known as asymptotic freedom. It was first predicted by Politzer [7], Gross and Wilczek [8] in 1973 and they were awarded Nobel prize in the year 2004 for this discovery. For low momentum transfer and large distances, $\alpha_s(Q^2)$ becomes very large and color charged particles cannot be found in isolation. This property of quarks at large distances is called color confinement. A review of constraints on $\alpha_s(Q^2)$ at high Q^2, as predicted by perturbative QCD, and its analytic behavior at small Q^2, based on models of non-perturbative dynamics is done in [9]. As a consequence of these two remarkable features of QCD, as summarised in Fig. 1.3 and Fig. 1.4, the QCD medium at very high temperatures and energy densities is expected to exist in a deconfined state of quarks and gluons called quark-gluon plasma (QGP). Big-Bang theory states that that our Universe originated from a state of almost infinite energy density and temperature. During the first few microseconds of its life the energy density in our Universe was so high that hadrons (color singlet bound states of quarks, antiquarks and gluons), such as the nucleons inside a nucleus, could not form. Instead, the quarks, antiquarks and gluons were deconfined and permeated the entire Universe in the form of QGP. As universe expanded, energy density ($1GeV/fm^3$) and the temperature (T 170 MeV) dropped and colored degrees of freedom became confined into color singlet objects and hadrons were formed. This is described in detail in the context of heavy ion collisions in the Section 1.4

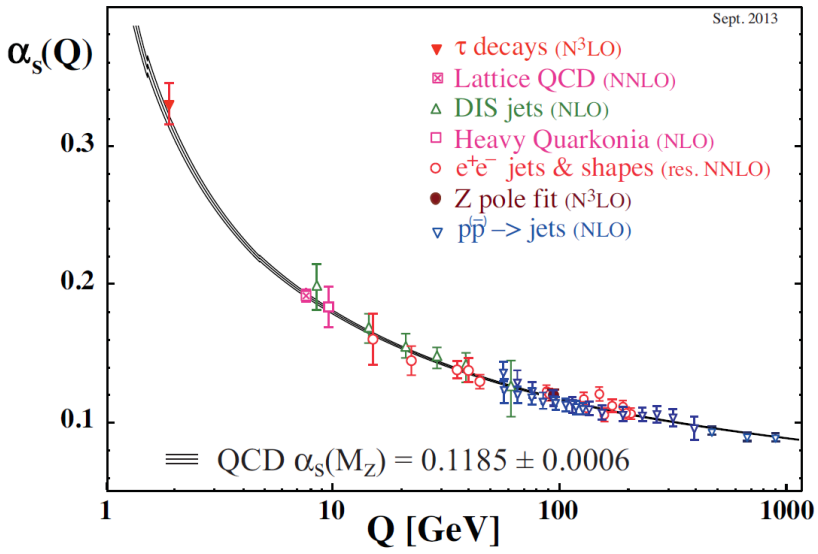

Figure 1.2: The variation of strong interaction coupling constant, $\alpha_s(Q)$ as a function of momentum transfer,Q measured from different experiments,showing agreement with QCD predictions. The black solid lines represent the QCD predictions [10, 11].

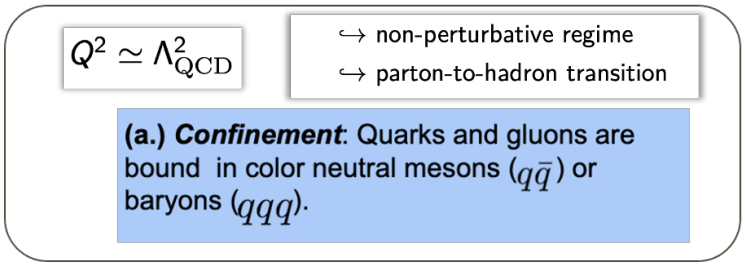

Figure 1.3: QCD properties at low energies, highlighting confinement

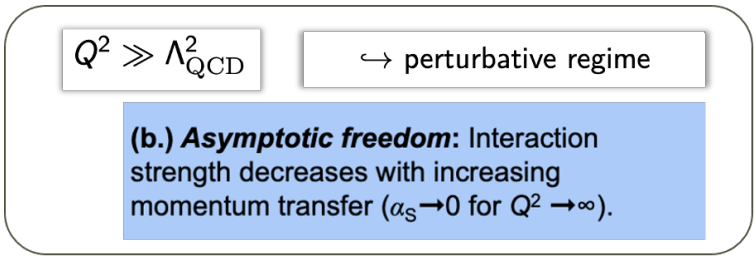

Figure 1.4: QCD properties at high energies, highlighting asymptotic freedom

1.2.3 Nature of QCD Phase Transition

As mentioned in the previous section in the context of running of QCD coupling constant, Lattice QCD predicts a phase transition from a state in which quarks and gluons are confined inside hadrons to a state in which they are deconfined: the quark-gluon plasma (QGP). A phase transition is accompanied by rapid changes in the properties of the medium continuously or discontinuously. Based on this, a phase transition can be either first order, second order or a crossover. A phase diagram in QCD illustrating regions of hadronic matter, quark-gluon plasma, and possible critical points or transitions between these states at various temperatures (T) and net baryon densities (μ_B) is given in Fig. 1.5.

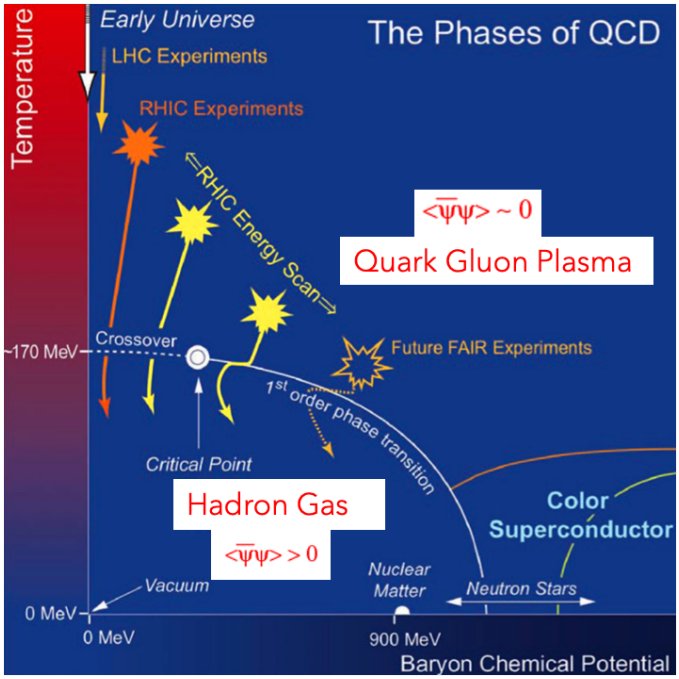

Figure 1.5: QCD T–μ_B phase diagram displaying the regions investigated by current and future experimental facilities. The three arrows in the figure indicate the starting point of the heavy ion beams and the targeting area of the phase diagram that they access. Figure taken from reference [12].

Understanding the QCD phase diagram and exploring various states of QCD matter is among the most challenges in particle physics community since its formulation. Even with tremendous improvements and predictions in theory, experimental observations remain limited and it is crucial to distinguish the differences between the experimental observations and hypothetical regions, when we see a QCD phase diagram.

Non-perturbative Lattice QCD calculations using first principles predict that the transition from hadronic to QGP phase is a smooth crossover at large T and vanishing μ_B [13–15]. However, phenomenological models suggest that at finite μ_B, this transition could be first order, which may further indicate the presence of a critical point [16]. The point on the T vs. μ_B diagram, where the first-order phase transition changes to crossover, is called the QCD critical point. Due to the asymptotic freedom of QCD, various quantities including the Equation of State (EOS) of QCD can be calculated directly from the QCD Lagrangian at extremely high densities and/or T using perturbation theory. The first results for the EOS came more than four decades ago for massless quarks and then modified models came including strange quark masses. There are several QCD based models [17], [18], [19] and lattice QCD calculations [20, 21] at finite μ_B that places lower bounds on the critical point. The Beam Energy Scan program at RHIC and other accelerators vary the collision energy to map out the phase diagram in the T-μ_B plane. A central goal of Beam energy scan program (BES) is to measure the beam energy dependence of fluctuation observables and identify a possible critical point in the QCD phase diagram. For each collision energy, thermal models are used to extract freeze-out parameters from experimental data. Discontinuities or non-monotonic behavior in these parameters as a function of energy could signal the critical point. A T–μ_B phase diagram with the interpretation of experimental data (from net-particle fluctuation measurements using STAR BESI program), dynamical simulations and chiral transition (shown in red) using lattice calculation, is shown in Fig 1.7.

There are thermal models which uses statistical mechanics framework to describe the

hadron production by assuming that the system reaches thermal and chemical equilibrium at the time of hadronization. The reason for the validity of the "thermal model" description for hadron yields in relativistic heavy ion collisions is widely discussed in ref [22]. To describe the continuous evolution of the system from QGP phase to freeze-out, hydrodynamic models are used. These models consider QGP as a relativistic fluid and provides a dynamic evolution and collective behavior of the matter which is not present in thermal models.

The thermal models, including the Hadron Resonance Gas (HRG) model (treats the hadronic matter as a gas composed of all known hadrons and resonances), are highly successful in reproducing the ratios of different particle species observed in experiments. The HRG models match well also with lattice QCD calculations at low temperatures (Fig.1.6). The most important application is the determination of freeze-out temperature and baryon chemical potential by fitting particle yields. Hydrodynamic models are able to capture the anisotropic expansion of the QGP, which is sensitive to the initial conditions and the viscosity of the medium. The collective flow phenomena, such as elliptic flow (v_2), triangular flow (v_3), and higher-order flow coefficients are reproduced by these models. Despite considerable theoretical and experimental efforts, the nature of the finite-temperature QCD transition—whether it is first-order, second-order, or an analytic crossover—remains ambiguous.

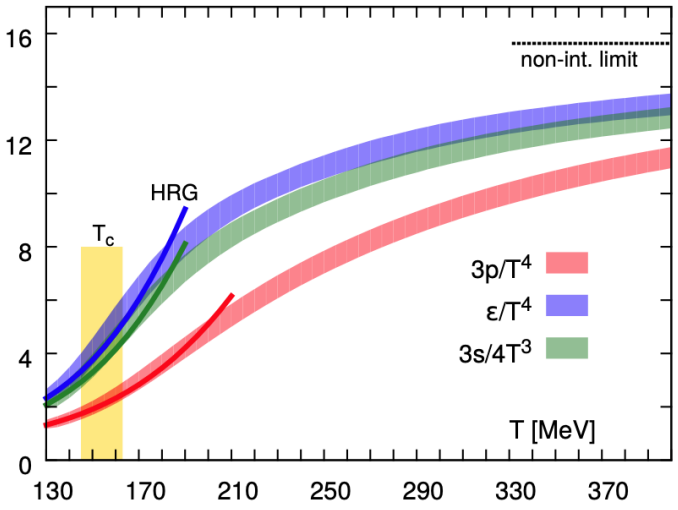

Figure 1.6: This shows normalized pressure, energy density, and entropy density to characterize the QCD equation of state as a function of the temperature calculated by HotQCD Collaboration. The dark lines show the prediction of the HRG model [21].

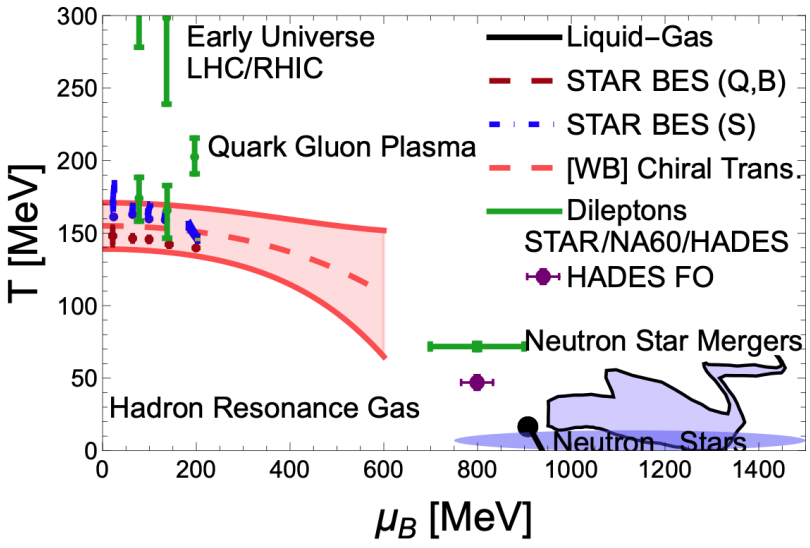

Figure 1.7: QCD T–μ_B phase diagram with the interpretation of experimental data (First phase of BES scan) and dynamical simulations of regions probed by various systems is shown [23].

1.3 Symmetry and Symmetry Breaking in QCD

Symmetry has always been a guiding light for physicists since the turn of the 20^{th} Century, and is at the root of all of our modern technologies. While perturbation theory enables us to perform calculations in the high-T deconfined phase, it fails to provide insights into the low-T hadronic phase. In addition to the phase transition to a deconfined phase, a second type of phase transition is expected from Lattice QCD calculations, the restoration of chiral symmetry. Referring to the Fig. 1.5, chiral symmetry is broken in the hadronic phase and as QGP is formed, the chiral symmetry is expected to be restored. Eventhough, there is significant experimental evidence for deconfinement, chiral phase transition remains as an area that still requires experimental validation. In this section, the objective is to review some of the relevant symmetry aspects of QCD that can shed light on the nature of chiral phase transition and particle production mechanisms.

QCD is built upon local SU(3) color gauge invariance. The interaction between quarks and gluons is completely determined by this gauge symmetry. It is independent of the various quark flavors (u, d, s , . . .) , so that the distinction between quarks, as far as their strong interactions are concerned, comes only from their different masses. Apart from its local color gauge symmetry, QCD has a number of global unitary symmetries which govern the strong interactions of hadrons. The significance of these symmetries is that they impose a well defined order on the spectrum of eigenstates of the QCD Hamiltonian, and that they imply conserved currents which set important constraints on the dynamics of strongly interacting systems.

1.3.1 Chiral Symmetry and Symmetry Breaking

Chiral Symmetry in QCD: In the context of QCD, chiral symmetry refers to the symmetry of the Lagrangian under the transformation of left-handed and right-handed components

of the quark fields. In other words, chirality is the Lorentz invariant generalization of helicity (handedness) of a particle where helicity is defined as the projection of spin to the momentum of the particle. Mathematically it is given by,

$$H = \frac{\vec{S} \cdot \vec{P}}{P} \tag{1.6}$$

If the particles have zero mass, chirality and helicity are the same. If the direction of the particle spin is same as the direction of its motion, we say that the particle has right handed helicity. Similarly, the particle has left handed helicity, if its spin and direction of motion are opposite to each other. In order to define handedness or helicity, the particle should have some finite mass. However, the mathematical definition of chirality is more abstract as it is determined by whether the particle transforms in a right- or left-handed representation of the Poincaré group. It is important to note that helicity and chirality are distinct for massive particles [24–26]. So, chiral symmetry is a symmetry of QCD in the limit of vanishing quark masses. We also know that the current quark masses are finite. But compared with hadronic scales the masses of the up and down and strange quarks, are small, so that chiral symmetry can be considered as an approximate symmetry of the strong interactions. To understand more about this, we will focus on the mathematical definitions of chiral symmetry and its role in particle physics and QCD. We said that symmetries of the Lagrangian lead to conserved quantities or currents. Consider a transformation of fields under which the Lagrangian is symmetric.

$$\Phi \rightarrow \Phi + \delta\Phi \tag{1.7}$$

$$\delta\mathcal{L} = \mathcal{L}(\Phi + \delta\Phi) - \mathcal{L}(\Phi) = 0 \tag{1.8}$$

Then the Lagrange's equation under this transformation would lead to following conservation equation.

$$\partial_\mu J^\mu = 0 \implies J_\mu = \frac{\partial \mathcal{L}}{\partial(\partial_\mu \Phi_i)} \delta\Phi_i \tag{1.9}$$

J_μ is the conserved current. Corresponding to this conserved current, it is also possible to define a conserved charge. Now consider adding a small symmetry breaking term to the Lagrangian. $\mathcal{L} = \mathcal{L}_0 + \mathcal{L}_1 = \mathcal{L}_0 + (-m\bar{\Psi}\Psi)$ Where the term $\mathcal{L}_0$ is symmetric with respect to the transformation and $\mathcal{L}_1$ breaks the symmetry. Therefore, $\delta\mathcal{L} = \delta\mathcal{L}_1$.

$$\delta\mathcal{L}_1 = \partial_\mu J^\mu \tag{1.10}$$

Because $\mathcal{L}_1$ is the symmetry breaking term, $\delta\mathcal{L}_1 \neq 0$. Correspondingly the current, J_μ would not be conserved. This says that whenever there is symmtery breaking in Lagrangian, there will be non-conservation of current. Now we will look at the definition of chiral symmetry in QCD using Lagrangian formalism. For simplicity, consider the Lagrangian of two flavors of massless fermions. $\mathcal{L} = i\bar{\Psi}\gamma^\mu\partial_\mu\Psi$ The index j refers to different flavors of fermions, for example up and down quarks. Consider the following transformations of fermion field, Ψ where $\vec{\sigma}$ refers to Pauli-spin matrices and γ_5 is the gamma matrix.

$$\Lambda_V : \Psi \to e^{-i\frac{\vec{\sigma}}{2}\cdot\vec{\theta}}\Psi \quad \text{and} \quad \Lambda_V : \bar{\Psi} \to e^{+i\frac{\vec{\sigma}}{2}\cdot\vec{\theta}}\bar{\Psi} \tag{1.11}$$

$$\Lambda_A : \Psi \to e^{-i\gamma_5\frac{\vec{\sigma}}{2}\cdot\vec{\theta}}\Psi \quad \text{and} \quad \Lambda_A : \bar{\Psi} \to e^{-i\gamma_5\frac{\vec{\sigma}}{2}\cdot\vec{\theta}}\bar{\Psi} \tag{1.12}$$

The Lagrangian for massless quarks under both the transformations given in Eqn. (1.11) and Eqn. (1.12) are invariant. Therefore, massless QCD is invariant under both Λ_V and Λ_A. And the symmetry due to these transformations is known as chiral symmetry. In group structure notation, it is denoted as $SU(2)_V \times SU(2)_A$. Λ_V exhibits invariance of the mass

term while Λ_A does not. Thus Λ_A is not a good symmetry if quarks have finite mass but can be considered as an approximate symmetry as long as quark masses are small. The mathematical form of conserved currents corresponding to Λ_V and Λ_A are referred to as 'vector current' and 'axial vector current' respectively.

$$V_\mu = \bar{\Psi}\gamma_\mu \frac{\vec{\sigma}}{2}\Psi \quad ; \quad A_\mu = \bar{\Psi}\gamma_\mu\gamma_5 \frac{\vec{\sigma}}{2}\Psi \tag{1.13}$$

The underlying symmetry associated with vector current is the isospin symmetry of the strong interaction and hence the hadronic vector current is identified as isospin current. Often, chiral symmetry is simply implied to refer to the axial transformation, Λ_A. This is because of the special role it plays, as it is spontaneously broken in the ground state, which will be discussed in the following section.

Spontaneous Symmetry Breaking Not only symmetries, but also breaking of symmetries provide deep insights. Symmetry breaking can be distinguished into two types, explicit and spontaneous symmetry breaking. Explicit symmetry breaking is when the Lagrangian and the equations of motion of the system does not respect the symmetry. Spontaneous symmetry breaking is when the ground state (GS) fails to be invariant under the transformation. In other words, vacuum or GS does not exhibit the symmetry that is displayed by Hamiltonian and is also known as hidden symmetry. One of the examples for explicit symmetry breaking is parity violation in weak interactions. The first time that the concept of spontaneous symmetry breaking came to be perceived as a general principle was when Yoichiro Nambu (1921) introduced this mechanism into particle physics using an analogy with superconductivity [27]. Other examples of physis mechanisms explained using SSB are ferromagentism (popular example from condensed matter physics) and mass generation in Higgs field [28]. A compelling explanation for SSB is possible using a "Mexican hat" potential and rotation symmetry. Consider two rotationally invariant potentials as given in 1.8. In Fig1.8(a), the

ground state is in the middle and the entire system including the GS are invariant under rotations. On the other hand in Fig1.8(b), the ground state is at finite distance away from the center. The center point of the potential is at a maximum and hence it is unstable. In this case, the ground state can be any point on the valley and by picking up one of these points, the rotational symmetry of the ground state is spontaneously broken. Even though the Lagrangian for this system will have rotational symmetry, it is spontaneously broken in GS. So, the second potential displays SSB and motion of the particle around the valley does not cost any energy (no resistance to the excitations and therefore massless), whereas moving radially does (massive). This leads to the famous Goldstone theorem which states

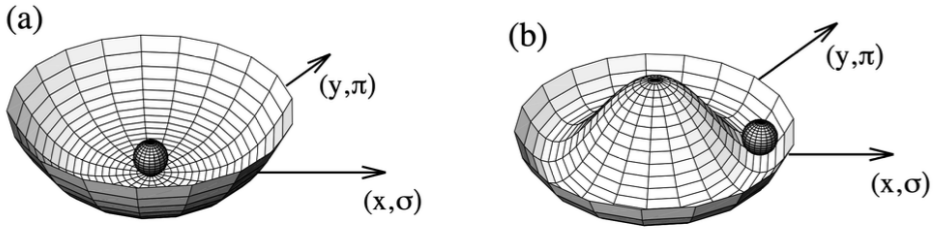

(a) No spontaneous breaking of symmetry (b) Spontaneous breaking of symmetry

Figure 1.8: The classical mechanics example using Mexican hat potential to describe spontaneous symmetry breaking in a rotationally invariant system.

that the spontaneous breaking of a continuous global symmetry is always accompanied by the appearance of a massless scalar particle called Nambu-Goldstone boson [29]. In QCD, the massless Goldstone-bosons are pions assuming we are dealing with a two flavor quark model. If chiral symmetry was a perfect symmetry, the pions would be massless. However, the chiral symmetry is only approximate which causes the pion to have a finite but smaller mass compared to other hadrons [25].

1.3.2 QCD Vacuum and Chiral Condensate

We defined the chiral symmetry of QCD, denoted by $SU(2)_V \times SU(2)_A$ above and also saw that Λ_V exhibits invariance of the mass term while Λ_A does not. There is evidence both from low-energy hadron phenomenology and from lattice QCD calculations that chiral symmetry is spontaneously broken: ie, the ground state (vacuum) of QCD does not share the chiral symmetry of the Lagrangian. If the ground state were symmetric, both vector and axial charge operators would annihilate the vacuum. Under these transformations, hadrons exhibit certain properties depending on their spin and parity. The combination of quark-antiquark (meson) fields that carry relevant quantum numbers are given below. Here, the vector sign for pion and ρ meson indicates the iso-vector nature of the mesons i.e. these particles transform like a vector under isospin rotations.

$$\text{pion-like state :} \quad \vec{\pi} \equiv i\bar{\Psi}\vec{\tau}\gamma_5\Psi; \tag{1.14}$$

$$\text{sigma-like state :} \quad \sigma \equiv \bar{\Psi}\Psi \tag{1.15}$$

$$\text{rho-like state :} \quad \vec{\rho}_\mu \equiv \bar{\Psi}\gamma_\mu\vec{\tau}\Psi; \tag{1.16}$$

$$a_1 \text{ - like state :} \quad \vec{a}_{1\mu} \equiv \bar{\Psi}\gamma_\mu\gamma_5\vec{\tau}\Psi \tag{1.17}$$

Under Λ_V, the pion-like state transforms to another pion-like state and sigma-like state transforms into itself as.

$$\vec{\pi} \to \vec{\pi} + \vec{\Theta} \times \vec{\pi} \tag{1.18}$$

$$\sigma \to \sigma \tag{1.19}$$

Under Λ_A, pion and sigma-meson are rotated into each other as,

$$\vec{\pi} \to \vec{\pi} + \vec{\Theta}\sigma \tag{1.20}$$

$$\sigma \to \sigma - \vec{\Theta} \cdot \vec{\pi} \tag{1.21}$$

Naively, this would imply, that states which can be rotated into each other by Λ_A should have the same Eigenvalues, i.e the same masses. This, however, is clearly not the case. We do not expect that the explicit symmetry breaking due to the finite current quark masses is responsible for this splitting. The resolution to this problem is spontaneous breakdown of the chiral symmetry. There are also evidences from PCAC (Partial Conservation of Axial Current) relation for this. Now, the analogy using mexican hat potential example from previous section can be used to understand the chiral symmetry breaking in QCD. The QCD analog of spacial rotations of classical mechanic example will be axial vector rotation, Λ_A that rotates $\vec{\pi}$ into σ as we saw before. If the QCD effective potential at high-T has a shape similar to Fig1.8(a), the system is in stable equilibrium and symmetry is not broken. If the QCD effective potential at low-T has a shape similar to Fig1.8(b), the system has spontaneous symmetry breaking and the vacuum condensate or the vacuum expectation value of $q - \bar{q}$ pairs will be non-zero. Pions are the massless modes along the valley and sigma mesons are the massive excitations along the radial direction.

It means that the QCD vacuum contains at any given time a certain number of $\bar{q}q$ pairs, the so-called *chiral condensate*. These $\bar{q}q$ pairs can interact with a (massless) quark traversing the vacuum and change its helicity, as if it has mass. Simply speaking, the helicity, hence the momentum, is flipped back and forth by the vacuum, the quark "slows" down, as if it gained mass. This is most likely the origin of the so-called *constituent* quark masses of $m_{u,d} \approx m_{\text{nucleon}}/3$, which are two orders of magnitude larger compared to the current quark masses derived for asymptotically free quarks.

An additional consequence as already discussed of each spontaneously broken global symmetry is the existence of massless bosons, the so-called Goldstone bosons. When we incorporate strange quarks also into the model, there can be eight pseudo-scalar mesons $(\pi^{\pm}, \pi^0, K^{\pm}, K^0, \bar{K}^0, \eta)$, the eight lightest hadrons. The fact that they are not massless reflects that the masses of the three lightest quarks are small, but non-zero, the explicit breaking of the symmetry. **This is relevant for us because the motivation for this thesis depends on approximating the kaons as possible Goldstone bosons of the theory.**

1.3.3 Flavor and Isospin Symmetry

The fundamental symmetry of QCD is the local SU(3) gauge invariance, which dictates the interactions between quarks and gluons. It is responsible for the rich structure of the theory, including the confinement of quarks and gluons within hadrons. QCD also exhibits various global symmetries, such as flavor symmetries among quarks, which play significant roles in determining the properties of hadrons. With regard to the flavor structure, we can simply ignore the gluons since they are flavor independent. The distinction between different quarks only comes from their masses. If the masses of all quark flavors were equal, the Lagrangian would have an additional SU(N_f) flavor symmetry. This is not realized in nature, where the spectroscopy of hadrons deduces that there are several types of quark, currently six, with different masses, having the same properties with respect to the gluon fields. This quantum number is called flavor, a term coined by Murray GellMann [30] and Harald Fritzsch [31] in the early 1970s. Murray GellMann has played a crucial role in the development of the quark model, which allowed to classify the quarks in a systematic way and better understand the standard model.

The mass term of the QCD Lagrangian is not invariant under SU(6) flavor symmetry. The

Eqn. (1.23) shows that the non-conservation of current is due to the mass differences within the representation multiplet. If the mass differences between the quarks under consideration is smaller than the interaction scales, the mass term in the $\mathcal{L}_q$ of (1.22) can be treated as a perturbation term. This approximate symmetry involving up an down quarks is known as SU(2) isospin symmetry. Isospin is a quantum number that was originally introduced in 1930s to describe the symmetry between protons and neutrons. It treats the proton (uud) and neutron (udd), which belong to an isospin doublet and have nearly identical masses, as two states of the same particle. In the quark model, isospin symmetry refers to the symmetry between the up(u) and down(d) quarks, which have similar masses and strong interactions. If we include s quarks, it becomes an SU(3) isospin symmetry that talks about kaon multiplets. This is an approximate symmetry as the mass differences between the particles within the multiplet breaks the symmetry. Pions form a single iso-triplet. Kaons form two doublets of 1/2 isospin.

$$\mathcal{L}_q = \sum_{a=1}^{N_f} \bar{\psi}_a \left(i\gamma^\mu (\partial_\mu + igA_\mu) - m_a \right) \psi^a. \tag{1.22}$$

$$\partial^\mu j_\mu^A = -i \sum_{a,b=1}^{N_f} (m_a - m_b) \bar{\psi}_a (T^A)_b^a \psi^b \neq 0. \tag{1.23}$$

1.4 Heavy Ion Collisions and Space-Time Evolution

1.4.1 Big Bang and Early Evolution of Universe

The Big Bang theory is the prevailing cosmological model explaining the origin and early evolution of the universe. According to this theory, the universe began as an incredibly hot and dense point approximately 13.8 billion years ago and has been expanding ever since. One of the most compelling pieces of evidence supporting the Big Bang theory is the cosmic microwave background (CMB) radiation, which is the afterglow of the Big Bang. The

CMB provides a snapshot of the universe when it was just 380,000 years old, offering critical insights into its early conditions and subsequent evolution [32, 33]. Another key piece of evidence comes from the abundance of light elements such as hydrogen, helium, and lithium. Predictions of nucleosynthesis during the first few minutes after the Big Bang match the observed abundances of these elements in the universe today. Additionally, the observed large-scale structure of the universe, including the distribution of galaxies and the cosmic web, supports the theory of an expanding universe from an initial hot, dense state [34]. Observations of distant galaxies also provide evidence for the Big Bang. Edwin Hubble's discovery in the 1920s that galaxies are moving away from us in all directions led to the realization that the universe is expanding. This expansion implies that the universe was once much smaller and denser, consistent with the Big Bang model [35]. Modern observations using the Hubble Space Telescope and other instruments have further confirmed this expansion and provided more detailed insights into the universe's history and structure. The Fig. 1.9 shows the evolution of universe over 13.8 billion years to what we see today.

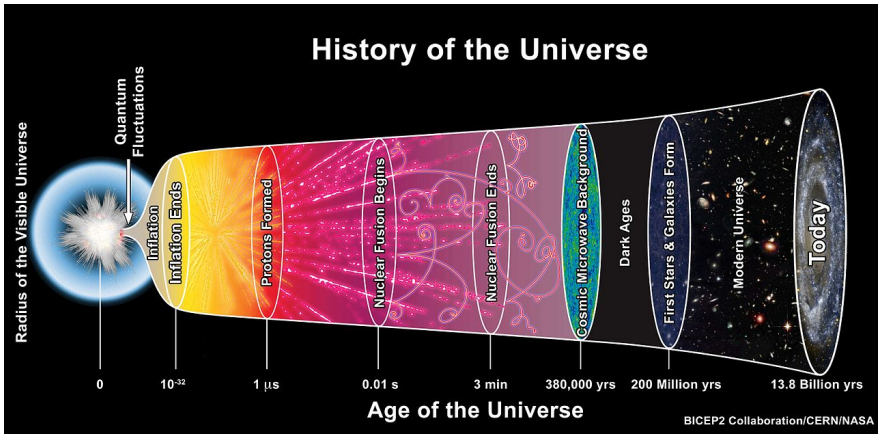

Figure 1.9: Illustration of the history of the universe. About one microsecond (μs) from the Big Bang, protons formed from the quark–gluon plasma. (Image: BICEP2 Collaboration/CERN/NASA)

1.4.2 Relativistic Heavy Ion Collisions

Relativistic heavy-ion colliders are the only tools that humankind has built to recreate the early moments of the universe in a laboratory environment. After the Big Bang, at high temperatures and densities, matter existed in the QGP phase. Heavy-ion colliders, such as the Large Hadron Collider (LHC) and the Relativistic Heavy Ion Collider (RHIC), are capable of producing QGP by accelerating heavy ions to nearly the speed of light and colliding them. The energy released in these collisions is so immense that the resulting temperature is about 100,000 times hotter than the core of the sun. These conditions allow the study of QGP, providing a unique opportunity to investigate the properties of strongly interacting matter under extreme conditions.

There is significant experimental evidence for the production of QGP in ultra-relativistic heavy-ion collisions, as measured by RHIC and LHC experiments. Results from various experiments, such as BRAHMS (RHIC) [36], STAR (RHIC) [37], PHOBOS (RHIC) [38], PHENIX (RHIC) [39], and ALICE (LHC) [40], highlight the compelling nature of these discoveries. Each experiment contributes insights and confirms the robustness of QGP detection. Experiments have shown that the enhanced production of strange hadrons (particles containing at least one strange quark), which is traditionally viewed as a signature of the QGP, arises gradually in proton–proton and proton–lead collisions as the number of particles produced in the collisions, or "multiplicity", increases. Another case in point is the gradual onset of a flow-like feature with the shape of a ridge with increasing multiplicity, which was first observed by CMS experiment in proton–proton and proton–lead collisions. This result was further supported by ALICE and ATLAS observations of the emergence of double-ridge features in proton–lead collisions.

The Fig. 1.10 shows heavy ions smashed into each other and its space-time evolution. At LHC, Lead (^{208}Pb) is utilized, it has an intriguing nucleus that is neutron-rich, containing

82 protons and 126 neutrons. When these heavy ions are accelerated to relativistic speeds, their shapes undergo a transformation due to Lorentz contraction. At such high velocities, the nuclei appear flattened like pancakes along the direction of motion. This effect is a direct consequence of special relativity, which states that objects contract in the direction of their travel as they approach the speed of light. The initial energy density is immense and the matter melts into QGP phase. As the system expands and cools, it undergoes hadronization and the system enters the hadron gas phase and continues to cool. During this phase, inelastic collisions among hadrons cease, leading to what is known as kinetic freeze-out. At this point, the momenta of the hadrons are fixed, and they begin to free-stream towards the detectors without further interactions. Finally, the particles produced in the collisions, such as pions ($\pi^{\pm}$), kaons ($K^{\pm}$), protons ($p, \bar{p}$), photons (γ), and electron-positron pairs ($e^{+}e^{-}$), are detected and analyzed. These final detected particle distributions provide critical information about the initial conditions, evolution, and properties of the QGP, allowing scientists to explore the fundamental aspects of strong interactions and the early universe.

Hadronization is fundamentally a non-perturbative process. This is because it involves the formation of bound states, a scenario where the strong coupling constant becomes significant, rendering perturbative QCD techniques inapplicable. The transition from a deconfined to a confined state of quarks and gluons is not adequately described by perturbative methods within QCD. Understanding hadronization in relativistic heavy ion collisions is essential for probing the early universe's conditions. It offers insights into how matter behaved under extreme conditions like those just after the Big Bang. To explore this complex phenomenon, researchers rely on experimental data and theoretical approaches, including non-perturbative methods like lattice QCD simulations, which provide valuable frameworks for interpreting the dynamics of quark and gluon confinement.

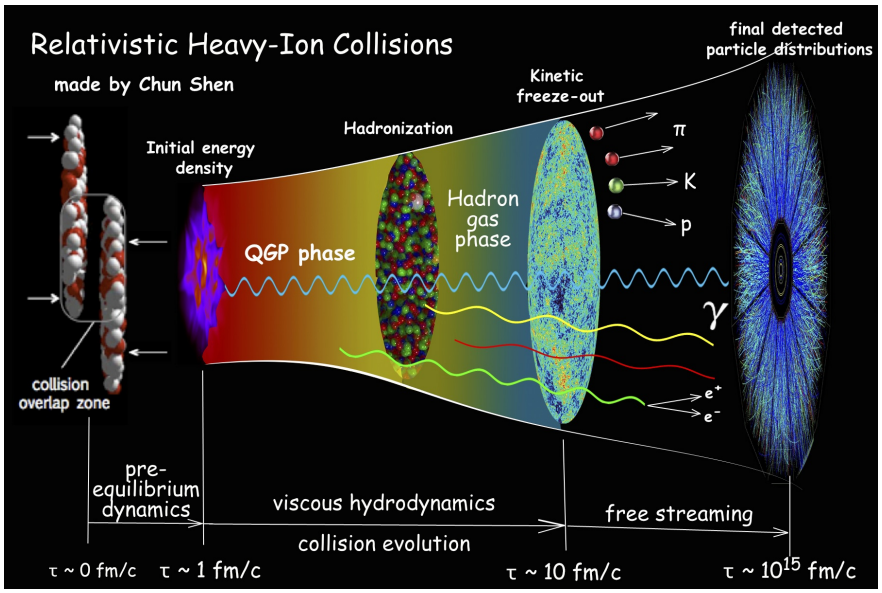

Figure 1.10: The schematic of relativistic heavy ion collision, showing various stages during its space-time evolution.

1.4.3 Experimental Probes of QGP

The QGP produced in heavy-ion collisions have a very short lifetime ($\approx 10\,\mathrm{fm}/c \approx 10^{-23}\,\mathrm{s}$), therefore it can not be studied directly, and we can only access the properties of the final systems produced in these colllisions as seen by detectors. However, theoretical models suggest certain observables that can be studied as signatures of QGP formation. This section provides a concise overview of the properties of kaons, the lightest strange hadrons central to our analysis. Additionally, we discuss relevant physics mechanisms, including the strangeness enhancement and the collective expansion of the fireball, experimental probes that signals the production of QGP.

Kaons and their Strangeness

Kaons are the lightest strange mesons and falls into one of the four types. There are neutral kaons, which are K^0, $\bar{\mathrm{K}}^0$ and charged kaons, K^+, and K^- with the quark strcuture masses as given in the Table 1.2. Kaons were discovered in 1947 in cosmic rays. Kaons have played

a distinguished role in our understanding of fundamental conservation laws: CP violation, a phenomenon generating the observed matter–antimatter asymmetry of the universe, was discovered in the kaon system in 1964 (which was acknowledged by a Nobel Prize in 1980). Parity violation in weak interactions was discovered through K^+ decays. This is called the famous $\tau - \theta$ puzzle. Kaons also hold much importance in our understanding of CP violation, one of the fundamental laws of symmetry that explains the observed matter–antimatter asymmetry of the universe. CP violation was first discovered in kaons in 1964, for which nobel prize was awarded. CP violation was discovered in the context of neutral kaon mixing which are two separate physics mechanisms. We know that K^- is antiparticle of K^+ and in case of neutral mesons, they are antiparticle of same particle. Just like neutral pions are antiparticle of same. The same can not be achieved in case of neutral kaons as they contain strangeness quantum number. There is an additional quantum number that needs to be conserved. This is how there are two types of neutral kaons which can turn from one into another through the weak interactions. A time evolution of neutral kaon states by assuming CP violation (it was thought that even though parity is violated in weak decays of kaons, CP symmetry is still respected) showed that there are two eigen states which are the K^0_S and K^0_L. The long-lived neutral kaon decays primarily into three pions, and the short-lived neutral kaon is called the decays primarily into two pions. If a beam of neutral kaons is left alone, all the K^0_S will decay and eventually there will be only the long lived K^0_L. It was observed that by passing this neutral kaon beam through matter, it is possible to regenerate K^0_S as the two neutral kaon states (K^0, $\bar{K}^0$) undergo different interactions. While looking for the confirmation of this observation, they observed a rare case of K^0_L decaying into two pions and thereby breaking the CP symmetry. Cronin and Fitch received the Nobel Prize in Physics (1980) for this observation of indirect CP violation.

Kaon Type	Quark Structure	Mass (MeV/c^2)
K^0	$d\bar{s}$	497.611
$\bar{K}^0$	$\bar{d}s$	497.611
K^+	$u\bar{s}$	493.677
K^-	$\bar{u}s$	493.677

Table 1.2: Types of Kaons, their quark structures, and masses are shown.

Strangeness Enhancement

The enhanced production of strange particles in heavy-ion collisions with respect to minimum bias pp collisions was proposed as a signature of QGP formation by Johann Rafelski and Bernt Muller in 1982 [41]. The strangeness enhancement is defined as the ratio of the yield of a strange or multi-strange particle relative to a non-strange particle. The experimental evidence of enhancement of various strange particles measured using Pb-Pb collisions at the LHC is displayed in Fig. 1.11. Statistical thermal models which assume a grand canonical ensemble approach are able to successfully describe this enhancement observed in heavy-ion collisions. The enhanced production of strange particles has also been observed in high multiplicity pp collisions at the LHC [42]. It is also seen that this enhancement increases with an increase in the strangeness content of hadrons.

Collective Expansion

In this section, we discuss the collective behavior of the QGP medium, highlighting its fluid-like nature and providing the most direct evidence of hydrodynamic behavior [44]. The matter created in heavy-ion collisions undergoes collective expansion due to a large pressure gradient. This collective expansion is known as anisotropic flow, one of the prime signatures of the QGP medium [44], [45]. First, we define a central concept used in characterizing heavy ion collisions, known as centrality. Nuclei are extended objects and the volume of the interacting region while they collide depends on the impact parameter, b of the collision,

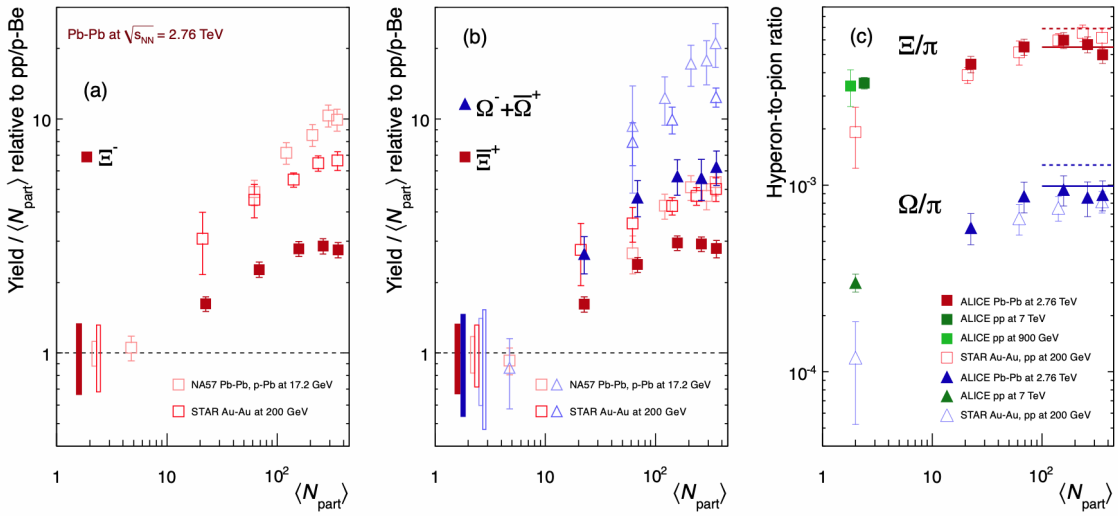

Figure 1.11: The enhancement of the multi-strange particles as a function of the mean number of participants shown for ALICE (full symbols), RHIC and SPS (open symbols)data. The figure taken from [43]

defined as the distance between the centres of the two colliding nuclei in the plane transverse to the beam axis. The schematic shown in Fig. 1.13 displays impact parameter. Centrality is directly related to impact parameter. Central collisions are head on collisions with maximum overlap region or impact parameter as zero whereas non-central or peripheral collisions are when impact parameter is large or there is minimum overlap between the nuceli. The collective flow is classified into radial flow and anisotropic flow. Radial flow is the only transverse flow in central collisions. The anisotropic flow becomes relevant in non-central collisions. A simple diagram depicting the pattern of radial flow and elliptic flow or v_2, which contributes dominantly to the azimuthal anisotropy is given in Fig. 1.12.

In non-central collisions (with non-zero impact parameter), nuclear overlap region of two colliding nuclei forms an initial spatial anisotropy, which is transformed, during the expansion of the subsequently created medium, into anisotropy in momentum-space (Refer to the Fig. 1.14 taken from [46]. This momentum anisotropy could be expressed as the coefficients of the Fourier expansion of the azimuthal momentum distribution of the produced

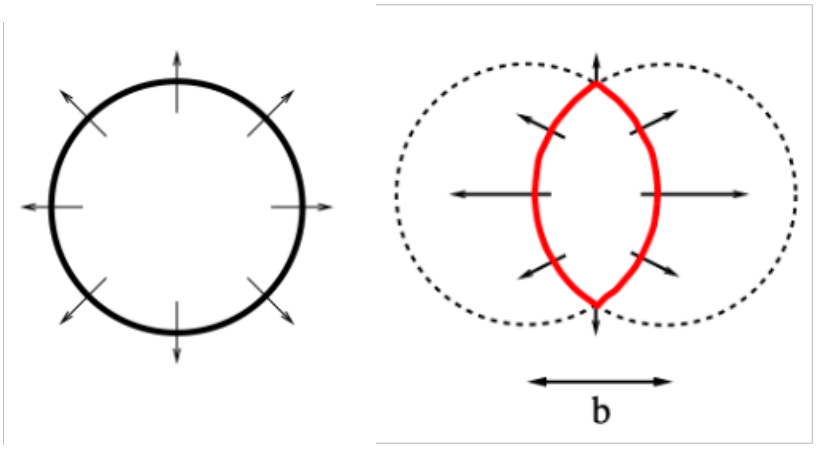

(a) (b)

Figure 1.12: Schematic of (a) Radial flow patterns and (b) Elliptic flow (v2) patterns in systems created in heavy ion collisions. b is the impact parameter of the collision.

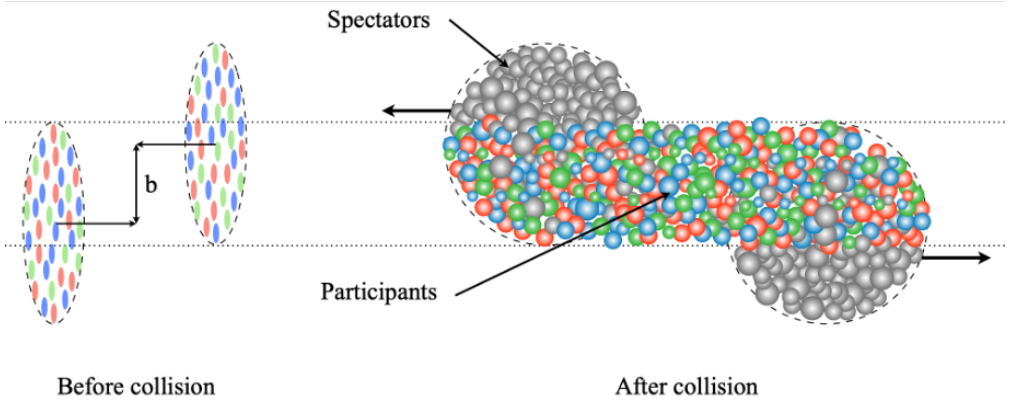

Figure 1.13: Schematic of heavy ion nuclei before and after the collision.

particles as given in Equation [47].

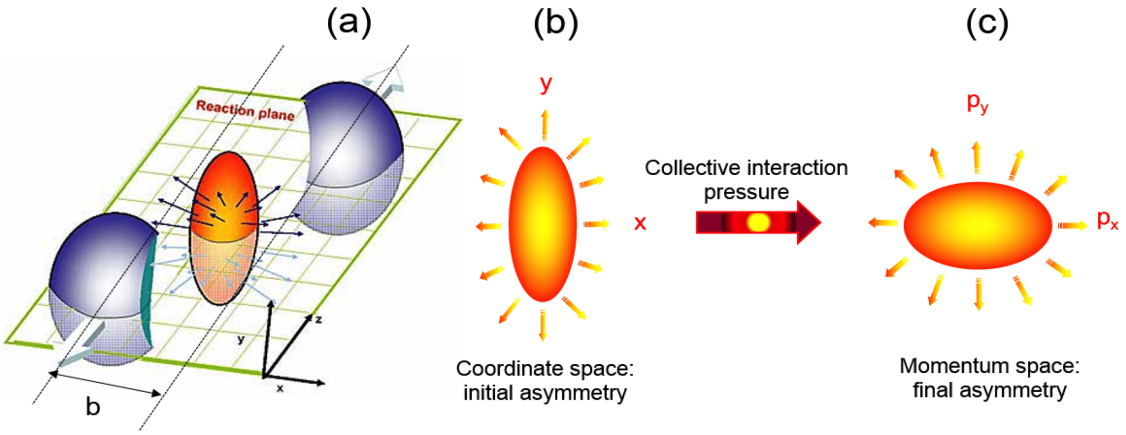

Figure 1.14: The schematic diagram illustrating the development of anisotropic flow in heavy-ion collisions, showing the transformation from initial spatial anisotropy to final momentum space asymmetry.

$$\frac{dN}{d\phi} \propto f(\phi) = \frac{1}{2\pi}\left[1 + 2\sum_{n=1}^{\infty} v_n \cos(n[\phi - \Psi_n])\right], \tag{1.24}$$

where ϕ is the azimuthal angle of the emitted particles, Ψ is the n^{th} order flow symmetry plane and $v_n = \langle\cos(n[\phi - \Psi_n])\rangle$ the n^{th} anisotropic flow coefficient. Here, $\langle \dots \rangle$ denotes an average over all particles in a single event. Together the v_n and Ψ_n define the n^{th} order (complex) anisotropic flow $V_n \equiv v_n e^{in\Psi_n}$, with $v_n = |V_n|$ representing the magnitude of V_n and Ψ_n its angle. Directed flow is the first harmonic coefficient in the Fourier expansion of the azimuthal distribution. Finite azimuthal anisotropy has been well observed in heavy-ion collision experiments so far [48–50]. Directed flow provides information about the initial geometry and is sensitive to the pressure gradients and the early-time interactions between the colliding nuclei. The second-order flow coefficient, also known as the elliptic flow (v_2), which is believed to be driven mainly by the geometry of the distributed nucleons in the nuclear overlap region during a non-central heavy-ion collision, has the dominant contribution to the overall azimuthal anisotropy. The third order flow coefficient is known as triangular flow (v_3).

1.5 Physics Motivation

1.5.1 Motivation from Previous Analysis: ALICE Result

The motivation behind this analysis comes from a previous ALICE publication that shows large dynamical correlations between the produced neutral and charged kaon particles in Pb–Pb collisions at $\sqrt{s_{\rm NN}} = 2.76$ TeV [51]. The measurement is performed using a fluctuation observable ν_{dyn}, where a and b corresponds to the distinct type of particles considered.

$$\nu_{dyn}(a,b) = R_{aa} + R_{bb} - 2R_{ab} \tag{1.25}$$

$$R_{aa} = \frac{< N_a^2 > - < N_a >^2 - < N_a >}{< N_a^2 >}; \quad R_{ab} = \frac{< N_a N_b > - < N_a >< N_b >}{< N_a >< N_b >} \tag{1.26}$$

The first two terms are called variance that measures the correlations between the particles of same type. The third term is called the covariance term which measures the correlations between a and b. It was Gavin and Kapusta [52] who proposed this statistical dynamical observable for studying the isospin fluctuations in the strange sector. For uncorrelated particles, all the terms in ν_{dyn} will vanish which consequently leads to $\nu_{dyn} = 0$. An example for uncorrelated production of particles is Poissonian. Any deviation in ν_{dyn} from zero indicates the presence of dynamic correlations that are of interest and it is also shown in literature that the magnitude of ν_{dyn} is expected to scale inversely with the number of sources, N_S which is proportional to the total multiplicity of heavy-ion collisions [53]. If the $\nu_{dyn} > 0$, detection of one particle biases the next particle to be of same type. And if $\nu_{dyn} < 0$ the detection of one particle biases the next particle to be of opposite type. Our focus is on the correlations between neutral and charged kaons and therefore we denote the terms by replacing a with c and b with 0 in Eqn. (1.25). R_{cc} measures the strength of

correlations between charged koans. R_{00} measures the strength of neutral kaon correlations, and R_{c0} is sensitive to charged-neutral kaon correlations. Together, the three terms measure the strength of relative fluctuations. Thus, $\nu_{dyn}[K^0_S, K^{\pm}]$ is sensitive to fluctuations of the neutral fraction f_K which was introduced in the earlier section in discussions related to DCC. In Fig 1.16, the measured values of ν_{dyn} are plotted as a function of collision centrality for $\mathrm{K^0_S K^{\pm}}$ (top trend) and $\mathrm{K^+K^-}$ (bottom trend). Both K^0_S and $K^{\pm}$ are selected in a rapidity interval of $|\eta| < 0.5$. A p_T cut of (0.2,1.5) (GeV/c) is applied for selecting $K^{\pm}$ and for K^0_S, minimum p_T is increased to 0.4 GeV/c. The data points are compared with HIJING, EPOS-LHC and AMPT models and are shown as dashed lines. Three different tunes of the AMPT event generator are used for the comparison.

- String Melting ON (SON) hadronic rescattering OFF (ROFF).
- String Melting OFF (SOFF) hadronic rescattering ON (RON).
- STRING Melting ON (SON) hadronic rescattering ON (RON).

The values of $\nu_{\mathrm{dyn}}[K^0_S, K^{\pm}]$ estimated from HIJING show a slightly increasing trend from central to peripheral collisions. The values obtained from AMPT (SOFF, RON and SON, RON) are in agreement with HIJING in each centrality bin. The values are slightly higher for SON and ROFF case compared to other two tunes. The ROFF mode switches off the decay of resonance particles, which can affect the number of produced kaons and hence influence $\nu_{\mathrm{dyn}}[K^0_S, K^{\pm}]$. This shows that ν_{dyn} is sensitive to the production dynamics. The values of $\nu_{\mathrm{dyn}}[K^0_S, K^{\pm}]$ are underestimated by the models (approximately factor of two in peripheral collisions and by an order of magnitude in most central collisions) whereas $\nu_{\mathrm{dyn}}[K^+, K^-]$ is in agreement with the models in all centralities except the last bin where some discrepancy is seen. In Fig. 1.15, ν_{dyn}/α is plotted as a function of collision centrality.

The parameter α is defined as the a multiplicity factor defined as below.

$$\alpha \equiv < K_S^0 >^{-1} + (< K^{\pm} >^{-1}$$

In case of K^+K^-, the model predictions and data are in agreement and the values do not show dependence on centrality/multiplicity. However the scaled ν_{dyn} depicted in Fig 1.16 of $K_S^0K^{\pm}$ shows a very surprising result. The data values show large deviation from the model predictions (factor of two in most central collisions) and shows a strong centrality dependence as we go from central to peripheral collisions. Both HIJING and AMPT models show no dependence on centrality. So, data shows a strong violation in ν_{dyn} from the expected $1/N_S$ scaling. To investigate if this scaling violation originates from which term in ν_{dyn}, a ratio plot of HIJING and data is made for the individual terms in the ν_{dyn} observable. In Fig 1.17, the individual contributions from data/HIJING ratios of R_{00}, R_{cc} and R_{c0} are plotted. We can see that it is indeed the ratio $R_{c0}^{\rm data}/R_{c0}^{\rm HIJING}$ that shows largest deviation from unity and a scaling violation (dependence on centrality) that is consistent with the violation observed in case of ν_{dyn}. The ratio $R_{00}^{\rm data}/R_{00}^{\rm HIJING}$ exhibits deviation from unity, but is independent of centrality whereas ratio $R_{cc}^{\rm data}/R_{cc}^{\rm HIJING}$ is closest to unity but features a collision centrality dependence. However, this scaling is insufficient to explain the centrality dependence observed in ν_{dyn}. Therefore, it is the term that measures the dynamical correlations between the produced neutral and charged kaons that shows the anomalous behavior that is not understood with the known physics mechanisms.

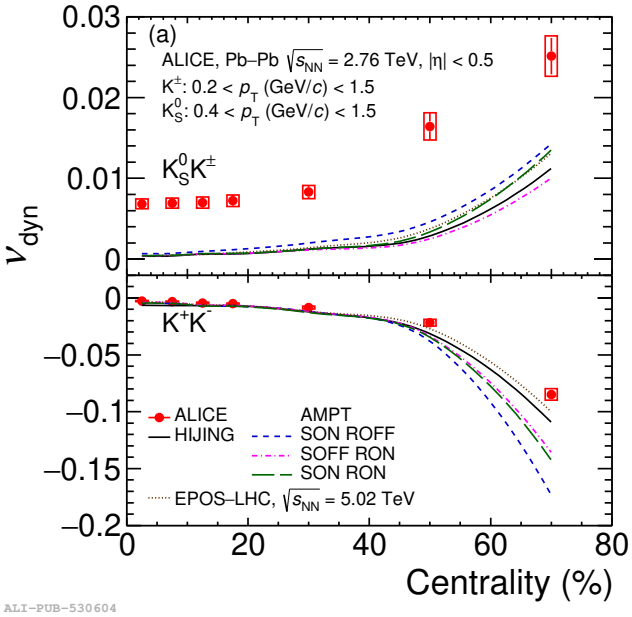

Figure 1.15: Measured values of $\nu_{\rm dyn}[K^0_S, K^{\pm}]$ (top) and $\nu_{\rm dyn}[K^+, K^-]$ (bottom) compared with HIJING and AMPT model calculations of these observables at generator level. The values are obtained using the Pb–Pb collision data at $\sqrt{s_{\rm NN}} = 2.76$ TeV.

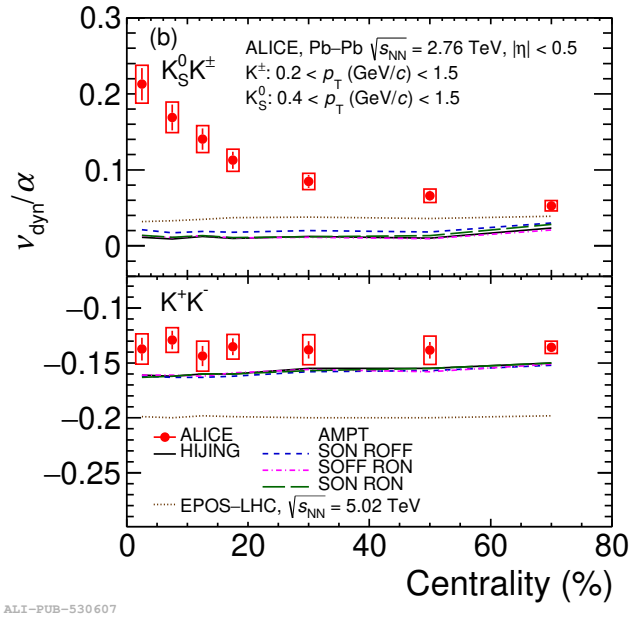

Figure 1.16: Measured values of $\nu_{\rm dyn}[K^0_S, K^{\pm}]$ (top) and $\nu_{\rm dyn}[K^+, K^-]$ (bottom) scaled by α compared with HIJING and AMPT model calculations of these observables at generator level. The values are obtained using the Pb–Pb collision data at $\sqrt{s_{\rm NN}} = 2.76$ TeV.

The correlation observed by ALICE is anomalous in its magnitude, in its extent in rapidity, and in its multiplicity dependence. These integrated correlations, not described by conventional heavy-ion models, such as EPOS and AMPT need further studies. So far, these measurements can only be described by invoking the presence of condensates. Two possible candidates are Disoriented Chiral Condensate (DCC) and Disoriented Isospin Condensate (DIC). These are discussed in detail in the next two sections.

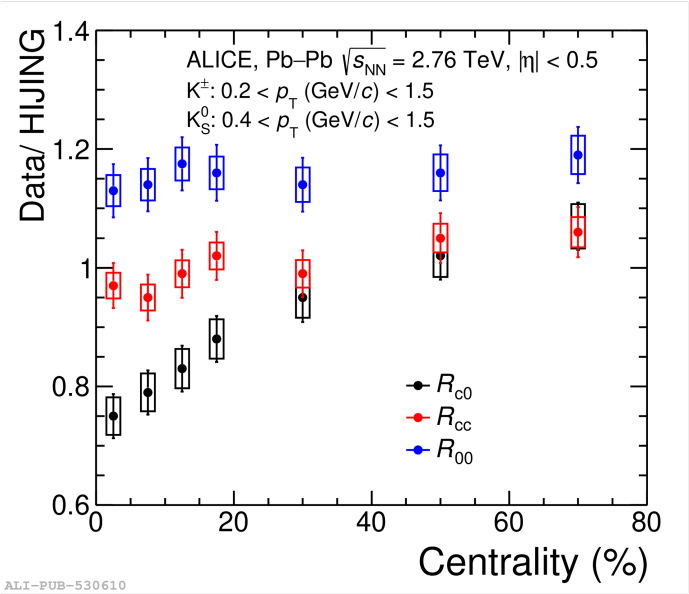

Figure 1.17: The ratio (Data/HIJING) of individual terms of $\nu_{\rm dyn}[K^0_S, K^{\pm}]$ as a function of centrality in Pb–Pb collision data at $\sqrt{s_{\rm NN}} = 2.76$ TeV.

1.5.2 DCC and Fluctuations of Neutral and Charged Particles

History of DCC Search: The restoration of chiral symmetry in QGP phase, followed by its relaxation back to the normal vacuum state, is thought to create transient regions where the chiral order parameter (vacuum expectation value) differs from that of the surrounding medium. These regions are known as Disoriented Chiral Condensates (DCC) [54], [55], [56]. The idea of possible formation of DCCs in relativistic heavy ion collisions was proposed by J.D Bjorken in 1990s [57]. Bjorken hypothesized that during the rapid expansion and cooling of the QGP, regions with misaligned chiral fields could form. This misalignment would result in domains where the chiral order parameter differs significantly from the surrounding vacuum, leading to observable consequences in particle production. Since the hypothesis of DCCs, it attracted a lot of interest and there have been significant theoretical and experimental efforts to detect and study these phenomena. since its existence was hypothesized. One of the notable experimental efforts was the Minimax experiment at the Fermilab collider. This experiment was specifically designed to measure charged particle and photon multiplicities in the forward direction, with the primary intent to look for DCCs in heavy ion collisions [58]. Additionally, there have been signals from cosmic ray studies indicating large asymmetry in the production of photons versus charged particles. These are called "Centauro" events where clusters consisting of almost exclusively charged pions and no neutrals have been observed, could be explained by DCC formation [59–61]. The decay of DCCs is expected to result in significant event-by-event fluctuations in the ratio of neutral to charged particles. These fluctuations provide a unique signature that experimentalists can look for in collision data. The formation and decay of DCCs can be explained using the potential of the linear sigma model at finite temperature [62]. The model involves scalar (σ) and pseudoscalar (π) fields, which represent the sigma meson and the pion triplet, respectively and these fields

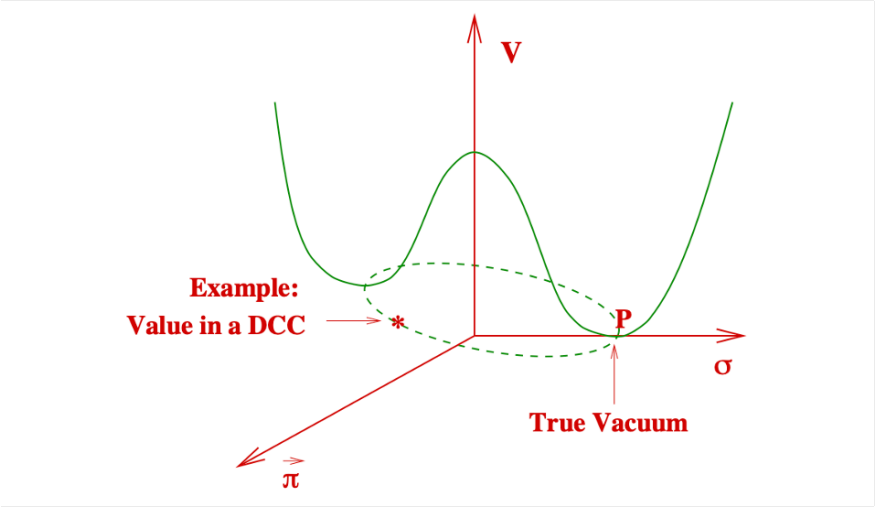

Figure 1.18: Effective potential of linear sigma model indicating the chiral symmetry broken phase.

are allowed to interact with each other.

$$V_{\text{eff}} = \frac{\lambda}{4}(\sigma^2 + \vec{\pi}^2)^2 - \frac{\lambda(\sigma^2 + \vec{\pi}^2)}{2}\left(f_\pi^2 - \frac{m_\pi^2}{\lambda} - \frac{T^2}{2}\right) - f_\pi m_\pi^2 \sigma. \tag{1.27}$$

As QGP produced in the heavy ion collisions cools down, chiral symmetry is spontaneously broken and there will be a non-vanishing order parameter (considering only up (u) and down (d) quarks in the model). When the field moves from a higher potential (excited state) to lower potential (lower energy), it emits pions of different isospins. This redistribution of energy is shown as the tilt in the potential or the disorientation of mexican hat potential as shown in Fig 1.18. In a generic particle production scenario, because of isospin conservation in the strong interaction, the production of π^+, π^-, and π^0 are equally probable. The concept of neutral pion fraction is introduced in the literature in this context.

Initial DCC searches focused on the pion sector, but no experimental evidence has yet supported DCC production. By extending the model to include strange quarks and employing SU(3) symmetry, the chiral condensate takes a different form, shifting the focus to the fluctuations of neutral and charged kaons. The chiral condensate's form and the distribution

of neutral particle fraction in both the pion and kaon sectors are discussed below.

$$\text{Chiral condensate in SU(2):}\langle\sigma\rangle \sim \langle\bar{u}u + \bar{d}d\rangle \tag{1.28}$$

$$\text{Chiral condensate in SU(3):}\langle\sigma\rangle \sim \langle\cos\theta(\bar{u}u + \bar{d}d) + \sin\theta(\bar{s}s)\rangle \tag{1.29}$$

$$\text{Neutral pion fraction:} f_\pi = \frac{n_{\pi^0}}{n_{\pi^0} + n_{\pi^\pm}}. \tag{1.30}$$

$$\text{Neutral kaon fraction:} f_k = \frac{n_{K^0} + n_{\bar{K^0}}}{n_{K^0} + n_{\bar{K^0}} + n_{K^\pm}} \tag{1.31}$$

Where, n_{π^0} is the total number of neutral pions and $n_{\pi^\pm}$ is the total number of charged pions. In case of thermal production, neutral pion follows a binomial distribution with a mean of 1/3. Whereas if pions are produced from DCC decay, they will have a different distribution for the neutral pion fraction as given below [63].

The normal kaon production would lead to a binomial distribution of the neutral kaon fraction, with a mean of 1/2. Here, $n_{K^0} + n_{\bar{K^0}}$ corresponds to the total number of neutral kaons and $n_{K^\pm}$ corresponds to the total number of charged kaons. On the other hand, production of kaons from DCC would follow a constant probability function and the proof is given in [64].

$$\text{Generic/thermal production in SU(2):} \quad P(f_\pi) \text{ follows Binomial with mean of } 1/3. \tag{1.32}$$

$$\text{Generic/thermal production in SU(3):} \quad P(f_k) \text{ follows Binomial with mean of } 1/2. \tag{1.33}$$

$$\text{DCC production in SU(2):} \quad P(f_\pi) = \frac{1}{2\sqrt{f_\pi}}, \quad 0 < f_\pi \leq 1. \tag{1.34}$$

$$\text{DCC production in SU(3):} \quad P(f_k) = 1, \quad 0 < f_\pi \leq 1. \tag{1.35}$$

The evolution of DCC domains can affect the strange particle production and therefore cause fluctuations in the number of neutral and charged kaons. Measurement of kaon isospin fluctuations at LHC energies is of interest even though past searches in the pion sector

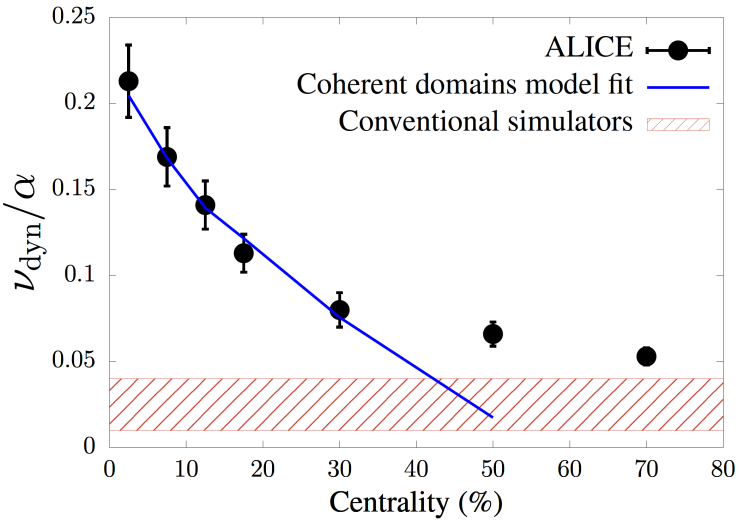

Figure 1.19: The ALICE data is compared with two parameter model to the five highest multiplicity bins. The two parameter fit is given in Equation. (1.36)

have yielded no evidence of DCC production. The STAR Collaboration did a measurement using ν_{dyn} observable between photons and charged particles. The charged particles (ch) are considered as a proxy for the charged pions and photons (γ) are treated as a proxy for neutral pions. The results [65] show that ν_{dyn} has a multiplicity dependence in case of both (ch+–ch-) and (photon-charged) combinations. This motivated ALICE to do this ν_{dyn} measurement in the kaon sector and the details of this analysis strategy are described in [66]. ALICE observed anomalous behavior that would support DCC formation with theoretical evidence from [67] indicating melting and refreezing of QCD vacuum. This two-parameter model includes multiple independent domains of condensates where each has a flat neutral kaon fraction probability distribution $P(f_k)$ =1 as shown in Eq.(1.36), where τ_{av}/τ_0 is the fireball lifetime. The comparison of ALICE data with this model is given in Fig.1.19.

$$\frac{v_{\rm dyn}}{\alpha} = \frac{2}{3} b \left(\frac{\tau_{\rm av}}{10\tau_0}\right) \left[\frac{b}{3a}\left(\frac{\tau_{\rm av}}{10\tau_0}\right) - 1\right]. \tag{1.36}$$

1.5.3 DIC and Fluctuations of Neutral and Charged Particles

This is a more recent theoretical framework that explains the possible fluctuations in the number of neutral kaons vs charged kaons as resulting from the formation of structures called Disoriented Isospin Condensate or DIC [68]. This paper investigates the possibility of isospin fluctuations in kaon sector coming from the fluctuations in the event-by-event fluctuations of the $\langle \bar{u}u \rangle$ vs. the $\langle \bar{d}d \rangle$ condensates. This is referred as DIC. In literature, it is always assumed that $\bar{u}u = \bar{d}d$. But at finite temperatures, their relative magnitudes can fluctuate.

- If there are only $\langle \bar{u}u \rangle$ domains, when it loses energy due to cooling, combination with strange quarks (s) and anti-quarks ($\bar{s}$) results in charged kaons.
- If the domain contains $\langle \bar{d}d \rangle$ then combination with strange quarks (s) and anti-quarks ($\bar{s}$) results in neutral kaons.

Considering scalar condensates of all forms created from up and down quark and anti-quark fields, $\langle \bar{u}u \rangle$, $\langle \bar{d}d \rangle$, $\langle \bar{u}d \rangle$ and $\langle \bar{d}u \rangle$, these can form scalar fields with $I = 1$ isotriplet and $I_3 = 0$ isosinglet. The quark combinations of isotriplet scalar fields are $\langle \bar{d}u \rangle$, $(\langle \bar{u}u \rangle - \langle \bar{d}d \rangle)/\sqrt{2}$, and $\langle \bar{u}d \rangle$. The isosinglet scalar field is $(\langle \bar{u}u \rangle + \langle \bar{d}d \rangle)/\sqrt{2}$. The vacuum condensate or lowest energy configuration can be isosinglet (proposed in this paper). But if energy barriers are low, this can excite to isotriplet directions and can result in fluctuations of $\langle \bar{u}u \rangle$ and the $\langle \bar{d}d \rangle$ condensates. This subsequently leads to the fluctuations of kaon flavor (neutral vs charged kaon). The anomaly observed in the ν_{dyn} measurement by ALICE can be better explained using this formulation [69].

DCC involves disorientation and emission from kaon fields i.e., in the strange quark sector while DIC involve disorientation in the light quark sector. Existence of iso-singlet field is easier to motivate and is related to chiral symmetry breaking.

In Fig.1.20, the evolution of light and strange quark condensate as a function of T is shown as calculated by the theory group, Hot QCD Collaboration [70]. The strange quark

condensate melts more slowly compared to the light quark condensate with T as expected because of the larger strange quark mass.

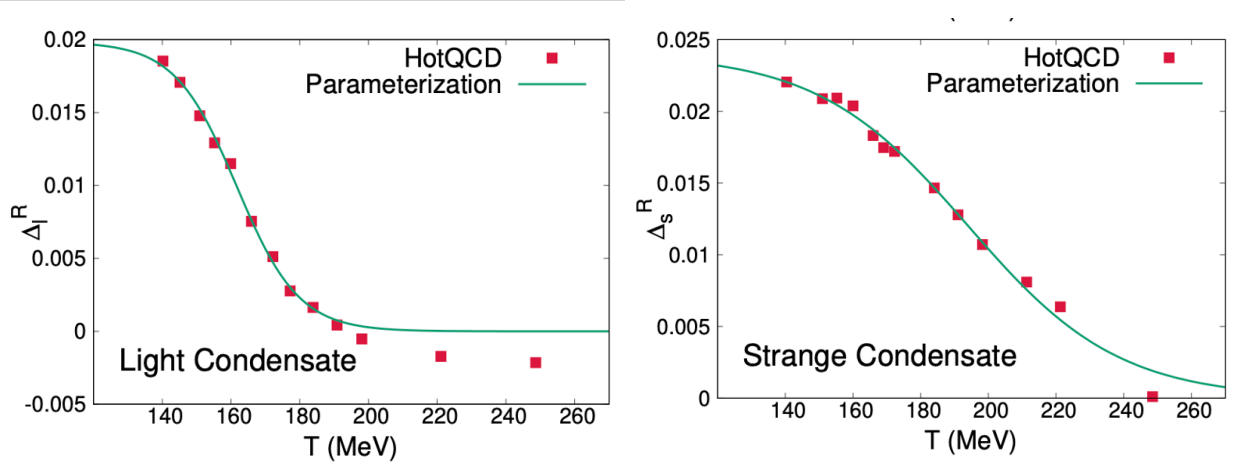

Figure 1.20: The light quark (left) and strange quark (right) condensates in dimensionless lattice units vs. temperature (T) as calculated by the Hot QCD Collaboration [70].

1.6 Analysis Objectives

The physics motivation behind this analysis derived from ALICE experimental result and its theoretical interpretations is described in the previous Section. 1.5. Here, we outline the specific objectives and goals of this analysis and detail the expected results we aim to achieve in this dissertation. The goal is to perform an independent measurement of two-particle angular correlation functions of neutral and charged kaons ($K^0_S K^{\pm}$) as a function of $\Delta\eta$ and $\Delta\varphi$ (where, $\Delta\eta$ is the pseudorapidity difference and $\Delta\varphi$ is the azimuthal angle difference between two particles) to investigate whether they exhibit any anomalous behavior, as observed in the ν_{dyn} measurement described in Section. 1.5. The angular correlation functions involving oppositely charged kaons (K^+K^-) is also computed as a baseline to the $K^0_S K^{\pm}$ correlation. The ν_{dyn} analysis was an integrated measurement whereas we aim for a differential analysis focusing on the third term in the definition of ν_{dyn} that measures the

correlations between the specific type of particles considered.

Historically, two-particle angular correlation functions have been extensively studied in RHIC and LHC experiments, as documented in numerous studies [71–82]. The visual representation and the ability to simultaneously explore various physics mechanisms behind particle production makes the study of angular correlation functions compelling. The baseline physics mechanism underlying all correlations is the global conservation of energy, momentum and quantum numbers such as strangeness, baryon number, and electric charge. Other specific phenomena that can contribute to the overall shape of such correlations include mini-jets, collective effects such as flow, Bose-Einstein correlations, resonance decays etc. Each effect produces a characteristic distribution in $\Delta\eta\Delta\varphi$ space. The final shape of the correlation function is determined by the baseline together with these additional contributions.

An example of an angular correlation function measured by the proton-proton collision data is shown in Fig. 1.21 along with different physics mechanisms contributing to various shapes. The nearside peak and the away side ridge shown by blue and red dashed lines are due to jets. Jets are collimated spray of particles produced by a high momentum quark or gluon in high-energy particle collisions. The near side peak is caused by particles coming from the same jet. Since both particles are going in almost the same direction, there is a small difference between their angles which results in a peak in $(\Delta\eta\Delta\varphi) \approx (0,0)$. If the pairs of particles come from back-to-back jets traveling in opposite direction, $\Delta\varphi$ is close to 180 deg and there is no correlation in $\Delta\eta$ which leads to a uniform structure in $\Delta\eta$ and is called as away side ridge. Bose-Einstein correlations occur when the correlations are computed between identical particles. In this analysis, correlations involve non-identical particles and therefore contribution from Bose-Einstein correlations will not be present. Then there are resonance decays that can contribute to the near side peak when correlations are measured between possible resonance decay products. In case of K^+K^- correlation, we expect to see a major contribution from $\Phi(1020)$ resonance that decays to K^+ and K^- with a branching ratio

of 48.9 ± 0.5%. Furthermore, $a_0(980)$, $f_1(1285)$ are resonances with decay channel resulting in K^0_S and $K^{\pm}$ and consequently can contribute to the $K^0_S K^{\pm}$ correlation. Since we aim to measure these correlations using the Pb–Pb collision data, we expect to see effects due to collective expansion leading to flow structures in both K^0_S and $K^{\pm}$ and K^+K^- correlations. Finally, the critical question concerns the type of signal in these correlations that would indicate the possible formation of condensates. Equally important is determining our expectations based on observations from the $\nu_{\rm dyn}$ analysis. The positive values of $\nu_{\rm dyn}[K^0_S, K^{\pm}]$ indicate that detecting a K^0_S biases the detection of the second particle to be of the same type, suggesting an anti-correlation between the produced K^0_S and $K^{\pm}$. Thus, we expect a possible anti-correlation structure in the $K^0_S K^{\pm}$ correlation. An example of anti-correlation structure observed in angular correlation functions is shown in Fig. 1.22.

To explore if there is any anomalous behavior in these correlations, the idea is to compare the results from the collision data to the predictions from Monte-Carlo simulations. This dissertation considers HIJING and AMPT models for this purpose. The analysis is conducted using the ALICE Pb–Pb collision data collected in 2018 at collision energy of 5.02 TeV.

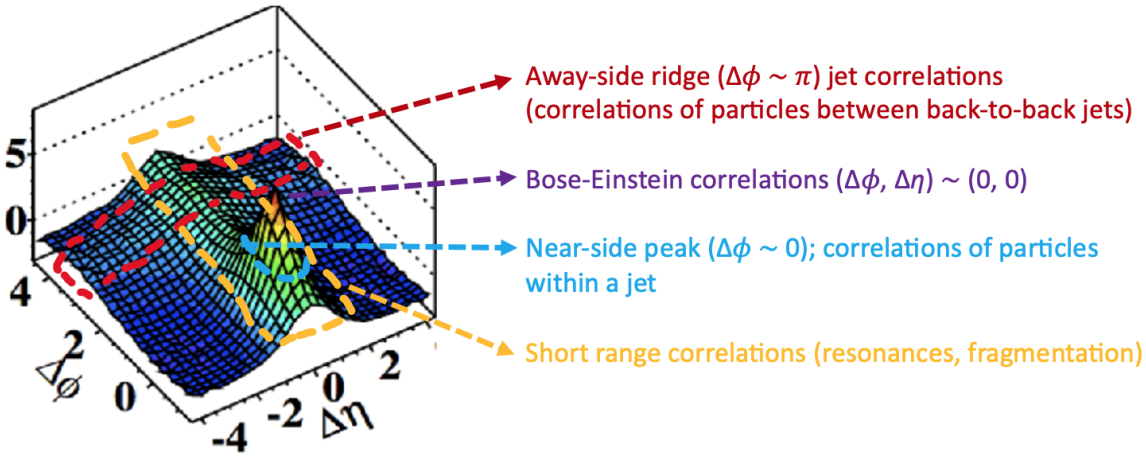

Figure 1.21: An example for a correlation function using pp collision data at $\sqrt{s_{\rm NN}} = 7$ TeV. Figure taken from reference [75].

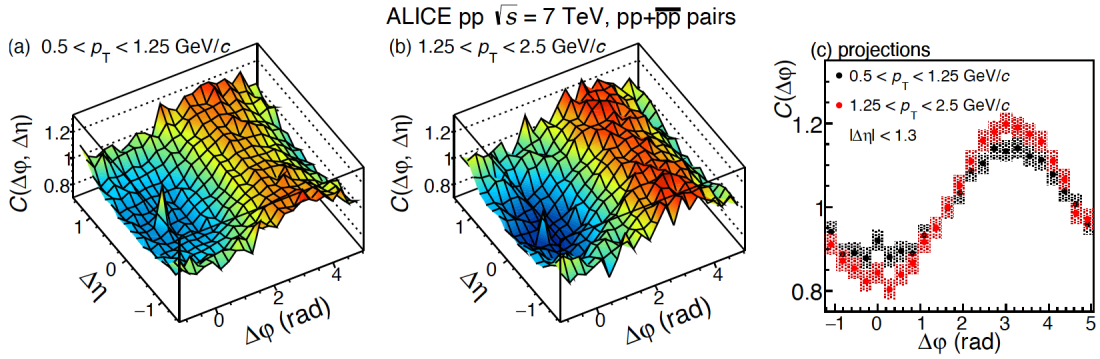

Figure 1.22: An example for angular correlation function showing anti-correlation signal. Panel (a) and (b) shows correlation functions for pp + p$\overline{\rm p}$ particle pairs using pp collision data at $\sqrt{s_{\rm NN}} = 7$ TeV. Panel (c) shows $\Delta\eta$ integrated projections of (a) and (b).

1.7 Organization of Dissertation

This dissertation measures the 2D and 1D two particle angular correlation functions of pairs of neutral and charged kaons ($K^0_S K^{\pm}$) and oppositely charged kaons (K^+K^-) using experimental Pb–Pb collision data at $\sqrt{s_{NN}} = 5.02$ TeV with the ALICE detector at the LHC. Chapter 2 presents an overview of ALICE experiment, including relevant sub-detectors, centrality estimation, and vertex reconstruction. The details of analysis strategy and methodology used to identify the neutral and charged kaons and to construct the correlation functions is given in chapter 3. Chapter 4 discusses the 2D and 1D correlation results, comparing them to HIJING and AMPT MC predictions and providing interpretations. Chapter 5 summarises the various investigations carried out in this analysis. Chapter 6 is dedicated to the future studies and preliminary results obtained.

Chapter 2

ALICE Experiment at the LHC

ALICE (A Large Ion Collider Experiment) is one of the nine detector experiments at the Large Hadron Collider (LHC) at CERN, along with ATLAS, CMS, TOTEM, LHCb, LHCf, MoEDAL, FASER, and SND@LHC. This chapter provides an introduction to particle accelerators and the accelerator complex at CERN, and offers a brief overview of the features of the ALICE detectors that are relevant for this analysis. This analysis utilizes ITS for vertex and track reconstruction, TPC and TOF for particle identification (SDD layer of ITS is also involved in particle identification) and V0 detector for centrality/multiplicity estimation. For specifications and more detailed descriptions of the ALICE experiment, refer to [83].

2.1 Particle Accelerators at CERN

Particle physics research heavily relies on particle accelerators, sophisticated devices that utilize electromagnetic fields to propel charged particles to extremely high speeds and energies while confining them within precise beams. The most prominent of these machines is the Large Hadron Collider (LHC), the world's largest and most powerful collider accelerator. Situated in a tunnel with a circumference of 27 kilometers beneath the France-Switzerland

border near Geneva, the LHC accelerates two beams of particles in opposite directions within separate, ultrahigh vacuum beam pipes before making them collide at speeds close to the speed of light. Inside the accelerator, two high-energy particle beams travel at close to the speed of light before they are made to collide. The beams travel in opposite directions in separate beam pipes – two tubes kept at ultrahigh vacuum. A strong magnetic field maintained by superconducting electromagnets is used to guide the beams around the accelerator ring. This requires chilling the magnets to -271.3°C – a temperature colder than outer space. For this reason, much of the accelerator is connected to a distribution system of liquid helium, which cools the magnets, as well as to other supply services. The Large Hadron Collider (LHC), built by the European Organization for Nuclear Research (CERN) is the world's largest and highest-energy particle collider. It lies in a tunnel 27 kilometres in circumference and as deep as 175 metres beneath the France–Switzerland border near Geneva. The Large Hadron Collider (LHC) is the world's largest and most powerful particle accelerator. It consists of a 27-kilometre ring of superconducting magnets with a number of accelerating structures to boost the energy of the particles along the way. The accelerator complex at CERN is a series of machines that accelerate particles to increasingly higher energies. Each machine boosts the energy of a beam of particles before injecting it into the next machine in the sequence. In the Large Hadron Collider (LHC)- the last element in this chain, the particle beams reach the final energies and are provided for collisions.

Linear accelerator 4 (Linac4) became the source of proton beams for the CERN accelerator complex in 2020. It accelerates negative hydrogen ions to 160 MeV to prepare them to enter the Proton Synchrotron Booster (PSB). The ions are stripped of their two electrons during injection from Linac4 into the PSB, leaving only protons. These are accelerated to 2 GeV for injection into the Proton Synchrotron (PS), which pushes the beam up to 26 GeV. Protons are then sent to the Super Proton Synchrotron (SPS), where they are accelerated up to 450 GeV.

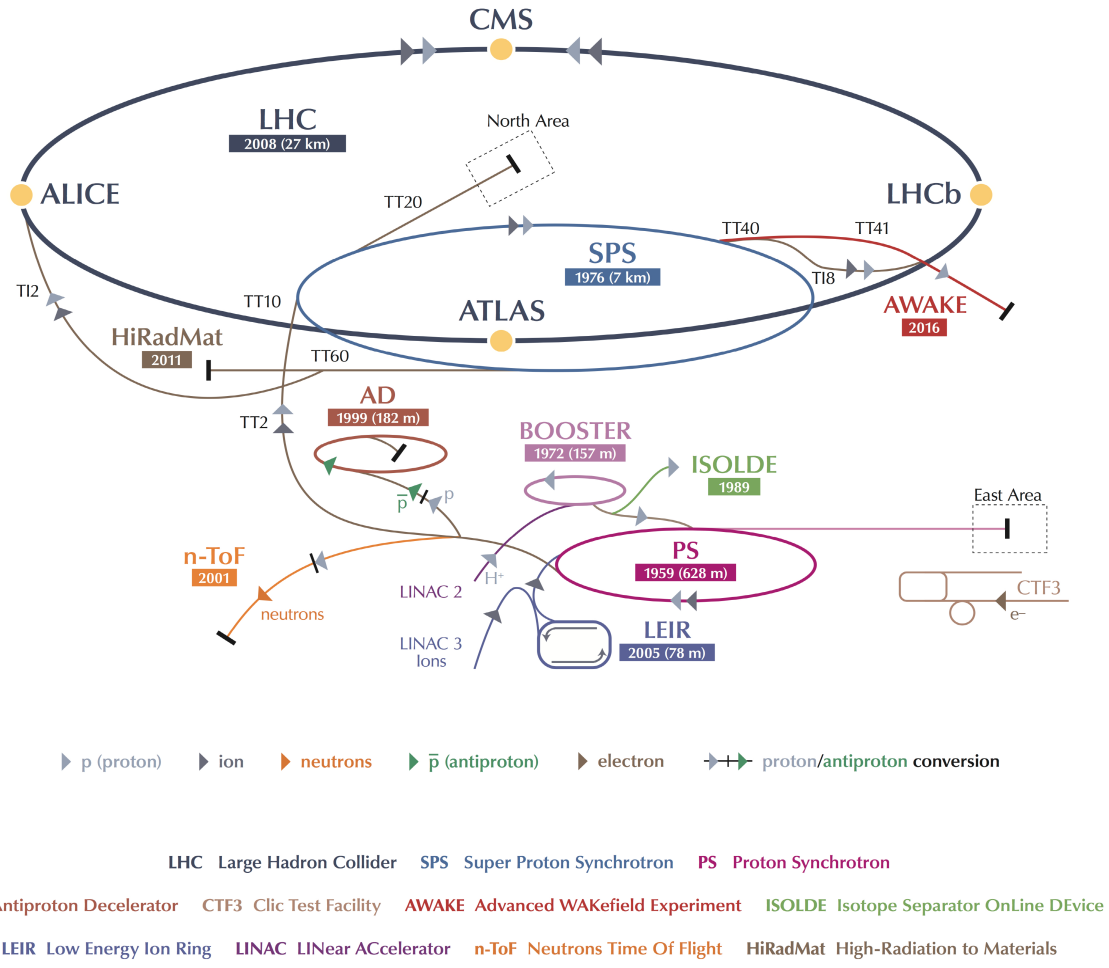

Figure 2.1: The schematic diagram of LHC ring at CERN's accelerator complex [84]

The protons are finally transferred to the two beam pipes of the LHC. The beam in one pipe circulates clockwise while the beam in the other pipe circulates anticlockwise. It takes 4 minutes and 20 seconds to fill each LHC ring, and 20 minutes for the protons to reach their maximum energy of 6.5 TeV. Beams circulate for many hours inside the LHC beam pipes under normal operating conditions. The two beams are brought into collision inside four detectors – ALICE, ATLAS, CMS and LHCb – where the total energy at the collision point is equal to 13 TeV. Protons are not the only particles accelerated in the LHC. Lead ions for the LHC start from a source of vaporised lead and enter Linac3 before being collected and accelerated in the Low Energy Ion Ring (LEIR). They then follow the same route to maximum energy as the protons.

2.2 ALICE Detector at LHC

ALICE is one of the major experiments at the LHC, CERN, comprising 17 sub-detectors as illustrated in Figure 2.2. These are categorized into three groups: central-barrel detectors, forward detectors, and the MUON spectrometer. ALICE was specifically designed to study the quark-gluon plasma (QGP) and thus is equipped to handle the high particle densities expected in central Pb–Pb collisions at the LHC." The details of the ALICE sub detectors used in this analysis are given below. The Fig. 2.3 displays the particle trajectories and energy deposition in the ALICE detector during the lead–lead collisions of the second LHC run.

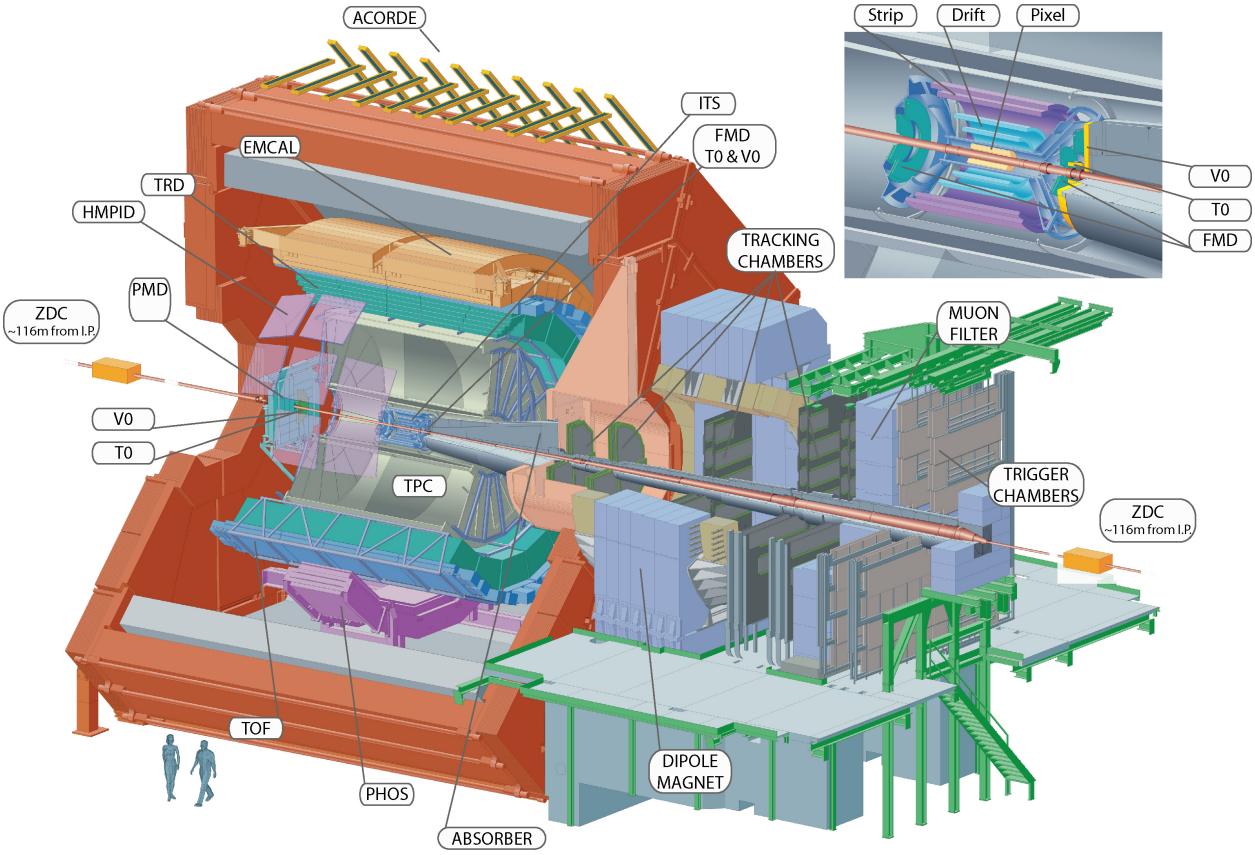

Figure 2.2: The ALICE experiment at the CERN LHC. The central-barrel detectors (ITS, TPC, TRD, TOF, PHOS, EMCal, and HMPID) are embedded in a solenoid with magnetic field B = 0.5 T and address particle production at midrapidity. The cosmic-ray trigger detector ACORDE is positioned on top of the magnet. Forward detectors (PMD, FMD, V0, T0, and ZDC) are used for triggering, event characterization, and multiplicity studies.

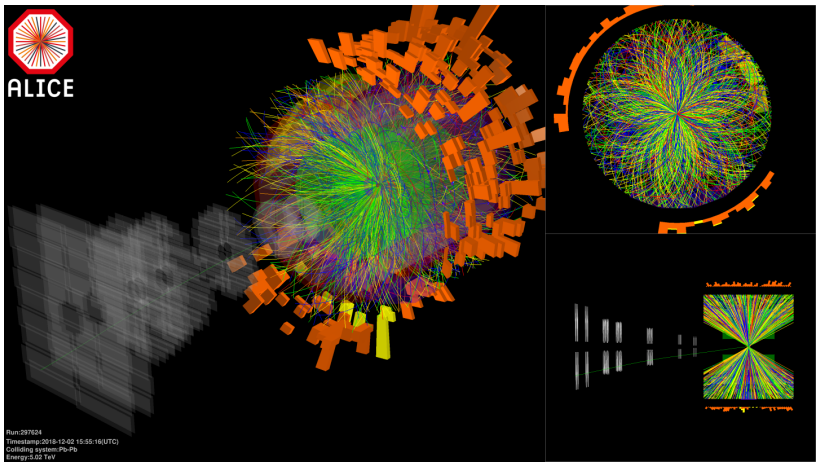

Figure 2.3: Particle trajectories and energy deposition in the ALICE detector during the lead–lead collisions of the second LHC run. (Image: CERN)

2.3 Central Barrel Detectors Relevant for this Analysis

2.3.1 Inner Tracking System (ITS)

The ALICE Inner Tracking System (ITS) is a critical component of the ALICE experiment at the LHC, designed to offer precise tracking and vertexing capabilities. This is the detector closest to the interaction point surrounding the beam pipe that is capable of determining the primary vertex with a resolution better than 100 micrometer. The ITS consists of six layers of silicon detectors, divided into three different technologies: Silicon Pixel Detectors (SPD), Silicon Drift Detectors (SDD), and Silicon Strip Detectors (SSD).

The SPD, comprising the two innermost layers, has a radial position of 3.9 cm and 7.6 cm, respectively. It provides high granularity and a fast response time, crucial for identifying primary vertices and detecting secondary vertices from heavy-flavor decays and photon conversions. The SDD, forming the next two layers at radial positions of 15.0 cm and 23.9 cm, offers good position resolution and energy loss measurements (dE/dx), essential for particle identification, especially at low transverse momenta ($p_T < 200$ MeV/c) as these tracks can not be reconstructed in TPC detector due to the larger bending caused by magnetic

field. The SSD, making up the outermost two layers at radial positions of 38 cm and 43 cm, ensures extended tracking capabilities and contributes to the overall momentum resolution of charged particles.

The ITS plays a pivotal role in the initial stage of track reconstruction by determining the primary interaction vertex using clusters in the first two SPD layers. The track finding in the ITS follows an inward-outward-inward scheme, starting from the outer layers of the Time Projection Chamber (TPC) and propagating tracks inward through the ITS layers. The ITS is instrumental in matching tracks with other central barrel detectors, ensuring accurate reconstruction of particle trajectories and enhancing the identification of various particle species through combined measurements of energy loss and momentum. The role of the ITS in the event, track and secondary vertex reconstruction, and the comparison of the resolution on the track impact parameter to the collision point in run2 data and Monte Carlo simulations is reported in [85].

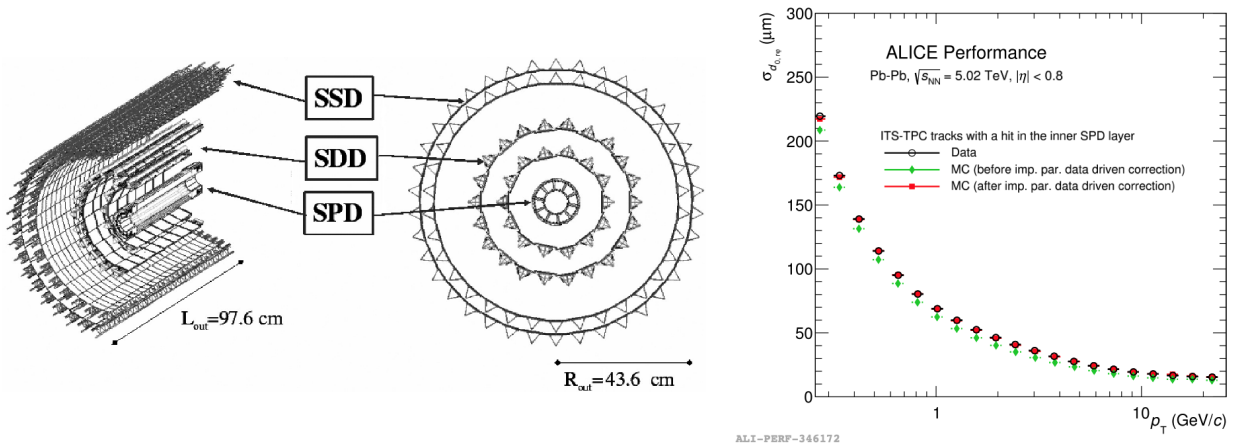

Figure 2.4: (a) A schematic of the Inner Tracking System detector (ITS 1) used during Run 1 and Run 2 data taking at the LHC is shown, illustrating the SPD, SDD, and SSD detectors, each with two layers.
(b) Impact parameter resolution in the transverse plane as a function of p_T for ITS-TPC tracks with a hit in the inner SPD layer in Pb–Pb collisions at $\sqrt{s_{\rm NN}} = 5.02$ TeV (pass1). The resolution in data (black) is compared with the same quantity in MC before (green) and after (red) the data-driven correction applied on reconstructed tracks.

2.3.2 Time Projection Chamber(TPC)

The Time Projection Chamber (TPC) at LHC is the primary tracking and particle identification detector for the ALICE experiment [86]. It is a cylindrical gaseous chamber with volume close to 90 m^3, containing Ne–CO gas mixture. It has full azimuthal acceptance except for the dead zones and it covers a pseudo-rapidity range of $|\eta| < 0.9$. The inner and outer radius of the cylindrical volume of TPC are about 85 cm and 250 cm, respectively and has an overall length of 5 m along the beam direction. The readout chambers are installed at the two end plates of the cylinder. Their design is based on the Multi-Wire Proportional Chamber (MWPC) technique with pad readout. A schematic of the TPC detector is given in 2.5. With a spatial resolution of 800 µm (drift) and 120 µm (transverse), the TPC ensures precise track reconstruction. It identifies particles via the technique of specific ionization energy loss (dE/dx) across a wide momentum range. Operating in a 0.5 T magnetic field, the TPC handles high track densities, crucial for studying the quark-gluon plasma and heavy-ion collisions.

Within the drift volume of the TPC, an electric field of 400 V/cm is achieved by applying a voltage of 100 kV at the central electrode. The finely segmented field cage at the inner and outer wall of the TPC provides a very high level of homogeneity of the drift field. The readout at the end caps is divided into 18 trapezoidal sectors in ϕ. In each sector, there is an inner (outer) readout chamber called IROC (OROC) with an active area between 84.8 cm and 132.1 cm (134.6 cm and 246.6 cm) in radial direction. The anode wires are arranged azimuthally around the cylinder axis and their signals provide the radial coordinate. The pads provide the hit coordinate along the wires above them. The third coordinate is obtained from the arrival time of the signals. It is important to produce a homogeneous electric field E along the axis of the cylinder and to align this parallel to the magnetic field B of the solenoid surrounding the TPC, in order to provide an undeformed projection of the original

ionization track onto the MWPC plane.

Precise reconstruction of particle tracks in the TPC requires a thorough understanding of the drift velocity and any inhomogeneities in the drift field. A non-uniform electron drift can be caused by mechanical or electrical imperfections in the field cage and readout chambers, whereas deviations of the electron drift from the ideal paths inside the gas volume are caused by temperature variations, relative misalignment of the electrical and magnetic fields and local variations of the electric field from moving charges (space-charge effects). To calibrate the drift field parameters against a known standard, a laser calibration system was built, using a large number of narrow ultraviolet rays at predefined positions inside the drift volume to generate tracks. The system was designed to make fast and accurate measurements of time varying drift velocities. It will run every half hour interspersed between physics events to measure the drift velocity and assess space charge effects. A schematic view of the TPC and the laser system is given in 2.6.

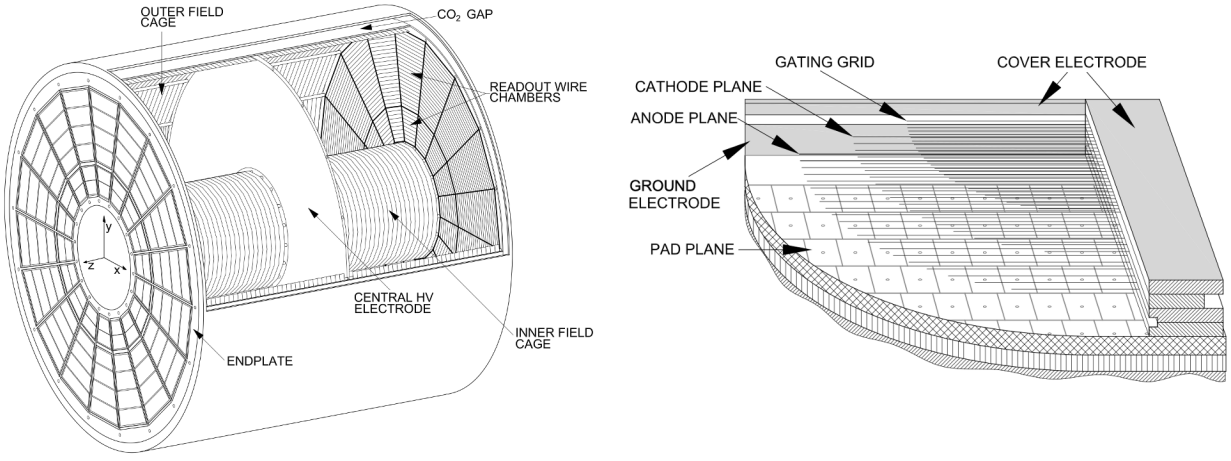

Figure 2.5: 3D view of the TPC field cage. The high voltage electrode is located at the center of the drift volume. The end- plates with 18 sectors and 36 readout chambers on each end are shown(left). The Cross section through a readout chamber showing the pad plane, the wire planes and the cover electrode (right).

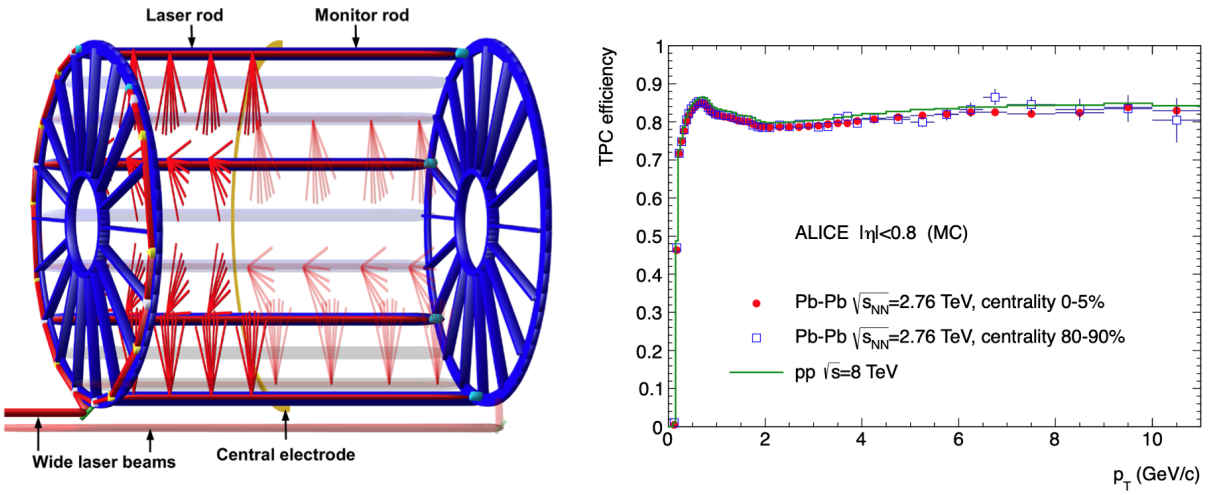

Figure 2.6: Schematic 3D view of the TPC laser system (left). TPC track finding efficiency for primary particles in pp and Pb–Pb collisions (simulation). The efficiency does not depend on the detector occupancy (right).

Particle identification is performed by comparing the measured energy loss of the particles with the theoretical prediction of the energy loss of charged particles described by the Bethe-Bloch formula given below.

$$\left\langle \frac{dE}{dx} \right\rangle = \frac{4\pi N e^4 Z^2}{mc^2\beta^2} \left(\ln\left(\frac{2mc^2\beta^2\gamma^2}{I} \right) - \beta^2 - \frac{\delta(\beta)}{2} \right), \tag{2.1}$$

where mc^2 is the rest energy of the electron, Z the charge of the projectile, N the number density of electrons in the traversed matter, e the elementary charge, β the velocity of the projectile, and I is the mean excitation energy of the atom. In the analysis of experimental data, other parameterizations than the Bethe-Bloch function are also used. The deviation of measured energy loss to the expected energy loss of a particle species can be expressed in terms of,

$$n\sigma_{\mathrm{TPC}} = \frac{\left(\frac{dE}{dx}\right)_{\mathrm{expected}} - \left(\frac{dE}{dx}\right)_{\mathrm{measured}}}{\sigma_{dE/dx}} \tag{2.2}$$

where $\sigma\left(\frac{dE}{dx}\right)$ is the energy resolution of the TPC detector, $\left|\frac{dE}{dx}\right|_{\mathrm{measured}}$ is the energy loss

measured in the TPC and $\left|\frac{dE}{dx}\right|_{\text{expected}}$ is the energy loss calculated from the Bethe-Bloch equation for a particular particle species. The specififc energy loss measured for differnet particle species as a function of transverse momentum is shown in Fig 2.7. The solid lines represent the calculated values of energy loss using Bethe-Bloch formula.

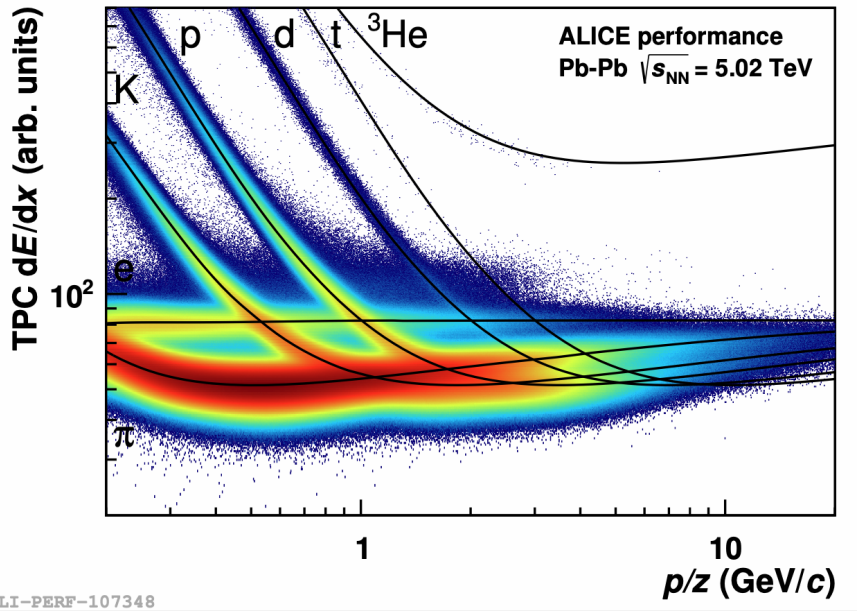

Figure 2.7: The energy loss per unit length in TPC as a function of track momentum in Pb–Pb collisions at $\sqrt{s_{\text{NN}}} = 5.02$ TeV. The solid lines show the parametrizations of the expected mean energy loss using Bethe-Bloch formula.

2.3.3 Time Of Flight (TOF)

To improve the particle identification capabilities, time of flight detector (TOF) is also used along with the TPC. It is designed to measure the flight time of particles from the collision point to the detector, allowing for precise identification of particle types [87]. The TOF system covers a large cylindrical area around the beam pipe and utilizes Multi-gap Resistive Plate Chambers (MRPCs) to achieve excellent timing resolution. With a time resolution of about 80 picoseconds and covering the pseudorapidity range of $|\eta| < 0.9$, the TOF detector is essential for distinguishing between different particle species, such as pions, kaons, and protons, in momentum range of 0.5–3/4 GeV/c. The ionization produced by charged particles initiates a gas avalanche, which produces a signal providing a stop time which is used to determine the time of flight of the particles. The expected time of each particle to reach the TOF detector based on the mass hypothesis, denoted by t_{exp}.

$$t_{\mathrm{exp},i} = \sum_k \Delta t_{i,k} = \sum_k \frac{\sqrt{p_k^2 + m_i^2}}{p_k} \Delta l_k \tag{2.3}$$

The fundamental variable of TOF PID is $t_{\mathrm{TOF}} - t_{\mathrm{event}} - t_{\mathrm{exp},i}$. The simplest PID estimator for a given mass hypothesis m_i is then constructed as an $n\sigma$ quantity in the following way,

$$n\sigma_{\mathrm{TOF},i} = \frac{(t_{\mathrm{TOF}} - t_{\mathrm{ev}}) - t_{\mathrm{expected},i}}{\sigma_{\mathrm{TOF},i}} \tag{2.4}$$

Where, t_{event} is the event collision time, t_{TOF} is the arrival time of the track measured by the TOF detector and $\sigma_{\mathrm{TOF},i}$ is the time resolution of the TOF detector. The Fig. 2.8 shows the TOF β distribution as a function of track momentum in Pb–Pb collisions, illustrating the track separation. The interaction time of the collision/event is denoted as t_{event} and is obtained from combined efforts of TOF and T0 detector. The T0 detector consists of two arrays of Cherenkov counters T0A and T0C, positioned at opposite sides of the interaction

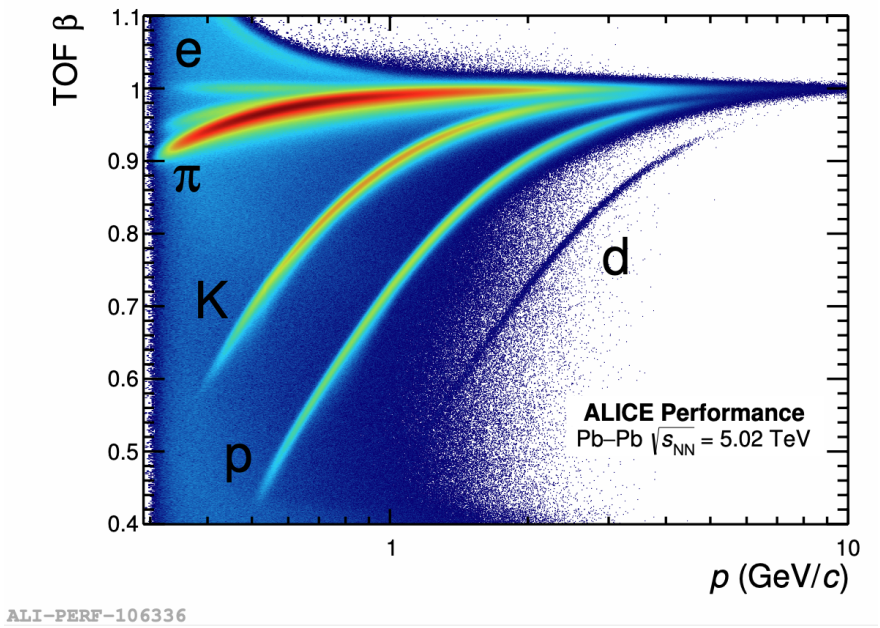

Figure 2.8: TOF β distribution as a function of track momentum in Pb–Pb collisions at $\sqrt{s_{\rm NN}} = 5.02$ TeV

point (IP) at a distance 360 cm and 70 cm away from the IP. Each array has 12 cylindrical counters equipped with a quartz radiator and photomultiplier tube. Left panel of the Fig.2.9 shows the distribution of the start time (interaction time of the collision) measured by the sum of the time signals from the T0A and and T0C detectors in Pb–Pb collisions at $\sqrt{s_{\rm NN}} =$ 2.76 TeV with respect to the nominal LHC clock value. Due to the finite size of the bunches and the clock-phase shift during a fill, this distribution has a width to it. The time resolution of the detector, estimated by the time difference registered in T0A and T0C, is 20–25 ps in Pb–Pb collisions and is shown in the right panel of Fig.2.9.

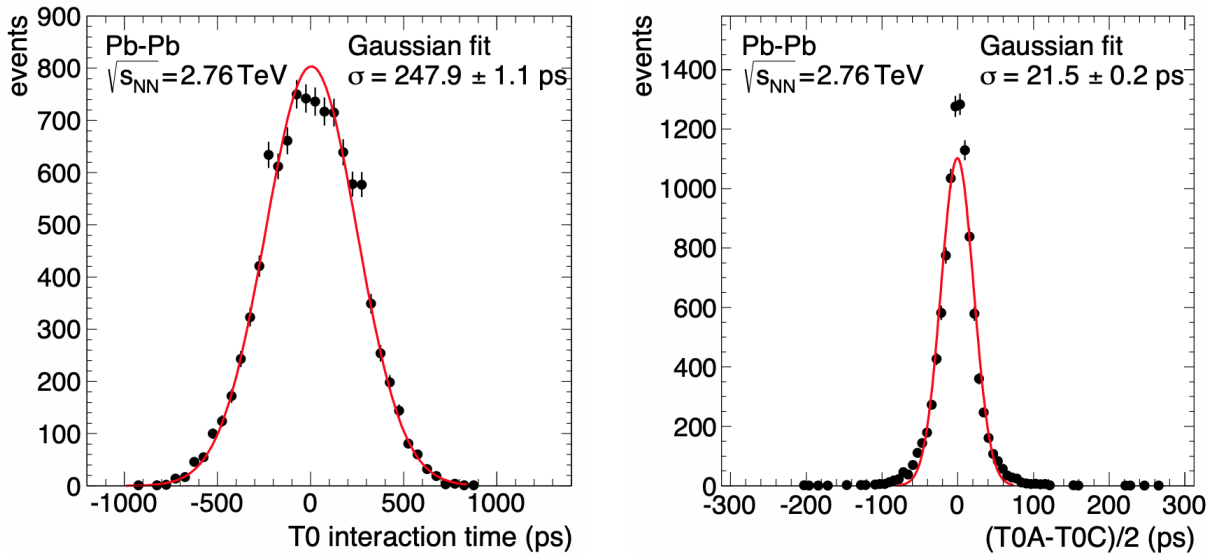

Figure 2.9: Interaction time of the collision with respect to the LHC clock measured by the T0 detector (left) and the resolution of the system obtained as the time difference between T0A and T0C (right). The time difference is corrected for the longitudinal event-vertex position as measured by the SPD.

2.4 V0 Detector and Centrality Estimation

The V0 detector is a small angle detector made of two arrays of scintillator counters, located asymmetrically around the collision point, along the beam direction, at z = 3.4m (V0A) and z = 0.9m (V0C), (shown in Fig. 2.10) and covering the pseudorapidity intervals $2.8 < \eta_{lab} < 5.1$ and $3.7 < \eta_{lab} < 1.7$, respectively. The V0 provides an online MB trigger through the logical coincidence of a signal in the two arrays, and participates in the determination of the luminosity by providing a reference process for van der Meer scans [88]. The major function of the V0 detector is to provide the trigger for the experiment - minimum bias and centrality trigger in A–A collisions are the relevant triggers for this analysis.

- A minimum-bias (MB) trigger: This is generated if number of channels fired during a collision is at least one on V0A and one on V0C. The detection of the fired channels is made by means of two observation windows, one for V0A and the other one for V0C.

- Two centrality triggers of the collision: These triggers are generated if one or the other, or both of the following conditions are respected:

    1. the integration charge seen by V0A and V0C during a collision is larger than a programmed trigger generation threshold (two such triggers are generated),
    2. the number of channels fired during a collision is larger than a programmed trigger generation (for V0A and for V0C).

It is also used to monitor LHC beam conditions and to measure several physics quantities such as charged particle multiplicity which is essential for the centrality measurement in nucleus-nucleus collisions, beam luminosity etc in the collisions. A detailed description of the acquisition and trigger electronics especially designed for the V0 detector is given in [89]. For spherical nuclei, the geometry of heavy-ion collisions is characterized by the impact parameter vector **b** connecting the centers of the two colliding nuclei in the plane transverse to the beams. In the experiment, the centrality is estimated using the particle multiplicities and/or the zero-degree energy.

Centrality The centrality percentile c of an A–A collision with impact parameter b is defined as,

$$c(b) = \frac{\int_0^b \frac{d\sigma}{db'} db'}{\int_0^\infty \frac{d\sigma}{db'} db'} = \frac{1}{\sigma_{AA}} \int_0^b \frac{d\sigma}{db'} db'. \tag{3}$$

Experimentally, the centrality is defined as the fraction of cross section with the largest detected charged-particle multiplicity N_{ch} or the smallest zero-degree energy E_{ZDC}. The cross section can be replaced with the number of observed events n and we get the following equation for centrality.

$$c \approx \frac{1}{N_{\mathrm{ev}}} \int_0^{N_{\mathrm{ch}}} \frac{dn}{dN'_{\mathrm{ch}}} dN'_{\mathrm{ch}} \approx \frac{1}{N_{\mathrm{ev}}} \int_0^{E'_{\mathrm{ZDC}}} \frac{dn}{dE'_{\mathrm{ZDC}}} dE'_{\mathrm{ZDC}}. \tag{5}$$

The above equations are based on the assumption that, on average, the particle multiplicity

at midrapidity (the zero-degree energy) increases (decreases) monotonically with the overlap volume (centrality). For the zero-degree energy measurement, this assumption holds only for central collisions $c \lesssim 50\%$, because nuclear fragments emitted in peripheral collisions may be deflected out of the acceptance of the zero-degree calorimeter, leading to low signals indistinguishable from those seen in central collisions.

In ALICE, there are several ways in which centrality is estimated. Here, we focus on the calculation based on the V0 amplitude. The V0 multiplicity (sum of V0A and V0C amplitudes) distribution was recorded in Pb–Pb collisions at $\sqrt{s_{\mathrm{NN}}} = 2.76\,\mathrm{TeV}$, requiring a coincidence of V0 and SPD, and using ZDC to reduce the electromagnetic dissociation background. The analysis is restricted to events with a vertex position within $|z_{\mathrm{vtx}}| \lesssim 10\,\mathrm{cm}$. The centrality bins are defined by integrating the charged-particle multiplicity distribution following Eqn.(5), and the absolute scale is determined by a model. The high-multiplicity part of the multiplicity distribution was fitted by the Glauber model (red line in Fig.2.11), and the extrapolation of the model was used to determine the unbiased number of events at low multiplicities. The Glauber model describes the collision geometry using the nuclear density profile, assuming that nucleons follow straight line trajectories and encounter binary nucleon-nucleon collisions according to an inelastic nucleon-nucleon cross section. The centrality determination via the particle multiplicity in V0 is illustrated in 2.11.

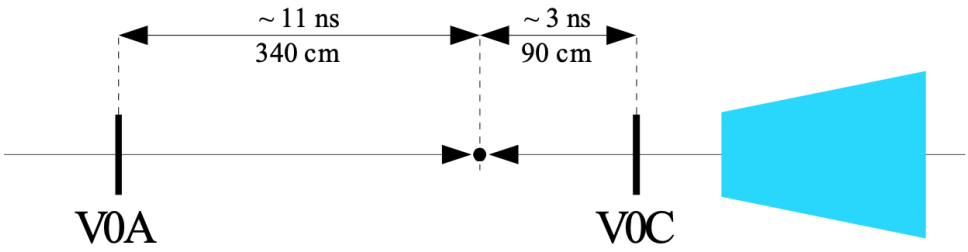

Figure 2.10: The positioning of V0A and V0C detectors on either sides of the interaction point.

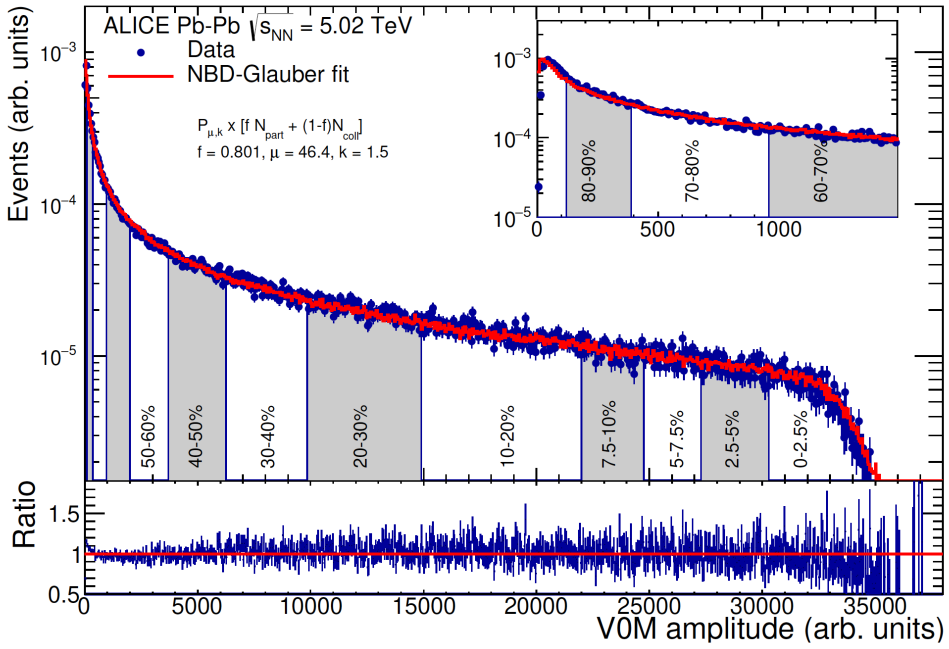

Figure 2.11: Distribution of the V0 amplitude (sum of V0A and V0C) recorded in Pb–Pb collisions at $\sqrt{s_{\rm NN}} = 5.02$ TeV is shown.

2.5 Vertex Finding and Track Reconstruction

The collision data collected by ALICE are processed according to a well-defined reconstruction sequence, as outlined in reference [90]. This process initiates with a clusterization phase, during which data from individual detectors are separately converted into clusters that are characterized by their positions, signal amplitudes, and related errors. Following this, an initial reconstruction of the interaction point is conducted using only the clusters from the SPD of ITS. Subsequently, track reconstruction begins at the outer radius of the TPC utilizing a Kalman-filter based algorithm. These tracks, once established within the TPC, are extended into the ITS layers to identify and track low-momentum particles. These TPC-originated tracks, now termed "global tracks," are then propagated outward, refined through updates from the TRD measurements, and linked with cluster data from additional detectors such as the TOF, HMPID, and calorimeters. In the final stages, these global tracks are propagated back toward the primary vertex to accurately determine each track's position, direction, curvature, and covariance matrix. This culminates in a sophisticated refinement of the interaction vertex, alongside the calculation of each track's closest approach to the primary vertex. Furthermore, the projection on the transverse plane (impact parameter) is assessed both in experimental data and Monte Carlo simulations, as depicted in Figure2.12. A detailed flow diagram showing the steps in the track reconstruction method in ALICE is shown in Fig. 2.13

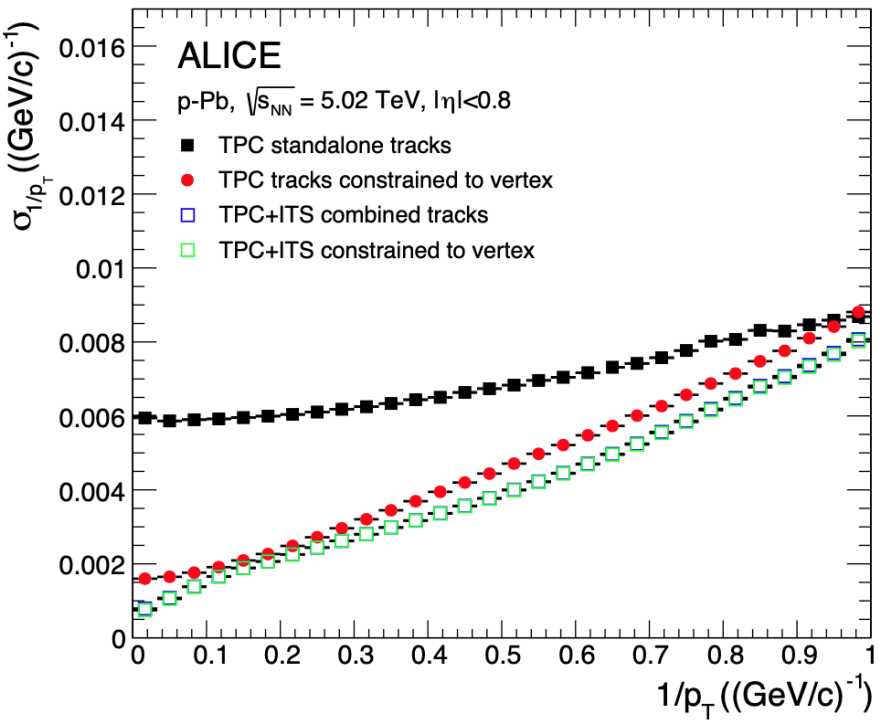

Figure 2.12: The p_T resolution for standalone TPC and ITS–TPC matched tracks with and without constraint to the vertex. The vertex constrain significantly improves the resolution of TPC standalone tracks. For ITS–TPC tracks, it has no effect (green and blue squares overlap).

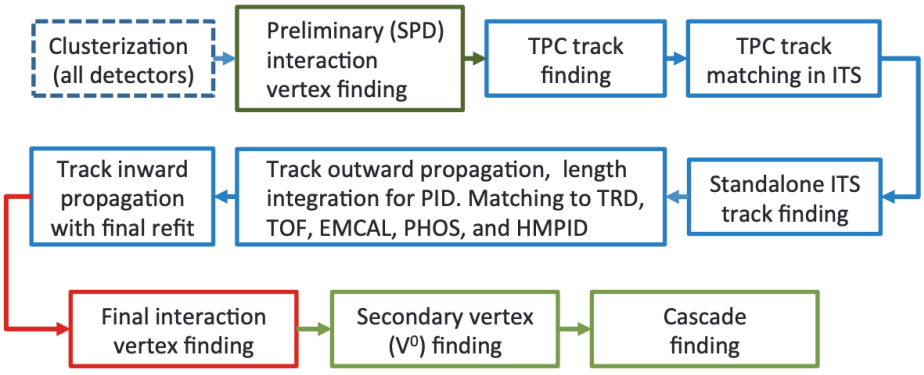

Figure 2.13: Flow diagram of track reconstruction steps

Chapter 3

Analysis Strategy and Details

3.1 Analysis Software

The analysis was performed using the AliFemto package, part of the AliPhysics Framework. AliPhysics (Github link: [91]) is a framework used in ALICE for performing physics analysis of collision data. It provides tools and libraries specifically designed for analyzing the output data from AliRoot, facilitating tasks like track and particle identification, event selection, and statistical analysis. AliRoot (Github link: [92]) is a specialized ROOT software used in ALICE, primarily for simulation, detector response, and reconstruction of raw data.

- Code directory: PWGCF/FEMTOSCOPY/(AliFemto and AliFemtoUser)
- Analysis task used for correlation function calculations: PWGCF/FEMTOSCOPY/macros/Train/AddTaskFemto.C
- Analysis task used for monte-carlo correction calculations: PWGCF/FEMTOSCOPY/macros/AddTaskEfficiency.C
- Analysis tasks are executed using LEGO Trains, the centralized grid system utilized in ALICE for handling and processing large data sets [93].

3.2 Data Sample and Event Selection

The data sample for this analysis is from Pb–Pb events/collisions collected in 2018 during Run2 data taking period (2015-2018) at collision energy, $\sqrt{s_{\rm NN}} = 5.02$ TeV. A summary of details of the dataset production is included in the Table 3.1. In ALICE analysis, a 'trigger' selects specific events of interest from the numerous collisions occurring in the detector. Triggers are designed to capture particular types of events based on predefined criteria, such as the presence of certain number of particles or specific collision characteristics. These selected events are then stored separately based on the trigger used. The minimum bias trigger, kINT7 is set as the default trigger in this analysis. Various event selection criteria, including the trigger are as follows:

- The background and poor quality events are rejected using `SelectCollisionCandidates` method from class `AliPhysicsSelection`.
- Pileup events are removed using the standard `AliEventCuts` class via `SetRejectTPCPileupWithITSTPCnCluCorr(kTRUE)`. This removes all events with pileup in TPC. ($\sim$32% of the events in the dataset LHC18q/r are removed using this cut).
- `AliMultSelection` class is used for estimating centrality(multiplicity). This analysis is performed in several centrality classes such as $0-10\%$, $10-30\%$, $30-50\%$ and $50-90\%$.
- The minimum bias trigger, `(AliVEvent::kINT7)` is set as the default trigger which uses information from SPD and V0 detectors. To improve statistics in the 0-10% centrality class, the `(AliVEvent::kCentral)` trigger is used.
- Only events with reconstructed primary vertex within a range: $|z_{vtx}| < 10$ cm from the center of the TPC (nominal collision point) were selected.

Table 3.1: Details of the experimental Pb–Pb collision dataset used for analysis is shown. (Software version ALIROOT-8373)

Dataset name	LHC18q/r_pass3_AOD252
Number of runs	145/103
Polarity	+0.5, -0.5
Energy	$\sqrt{s_{\rm NN}}$ = 5.02 TeV
System	Pb–Pb

The analysis was also performed on simulated data from the general-purpose official ALICE MC productions. HIJING and AMPT models were utilized and the details of these two production datasets are given in Table 3.2 and Table 3.3 respectively.

The distribution of events after each applied event selection criterion using a subset of HIJING MC reconstructed data is shown in the right panel of Fig. 3.1. Meanwhile, the left panel of Fig.3.1 displays the centrality profile distribution determined using the V0M trigger from the same HIJING dataset.

Table 3.2: Details of the HIJING general-purpose MC production anchored to pass3 of LHC18q and LHC18r dataset, minimum bias is shown. (software version ALIROOT-8462)

Energy	$\sqrt{s_{\rm NN}}$ = 5.02 TeV
System	Pb–Pb
Dataset name	LHC20e3a_AOD243
Generated events	3 Million
Output size	75.5 TB
Run time	442 y 97 d

Table 3.3: Details of the AMPT general-purpose MC production anchored to LHC15o dataset, minimum bias. (software version ALIROOT-7338)

Energy	$\sqrt{s_{\mathrm{NN}}} = 5.02$ TeV
System	Pb–Pb
Dataset name	META_AMPT_LHC17i2f_extra_AOD217
Generated events	4 Million
Output size	106.6 TB
Run time	452 y 68 d

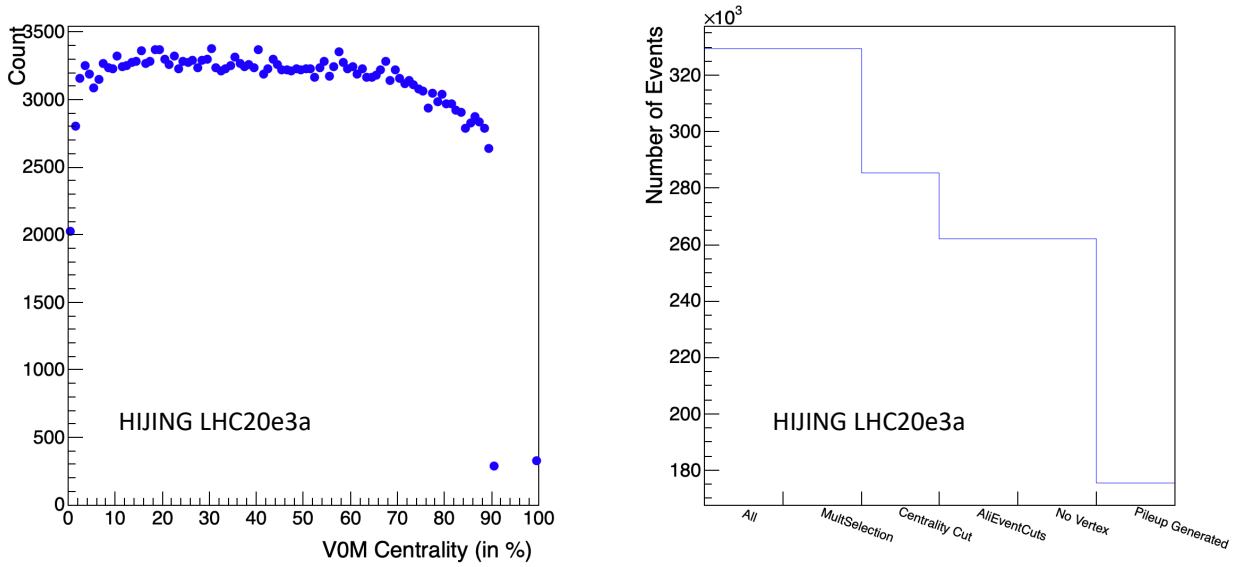

Figure 3.1: Distribution of centrality percentile using V0M trigger (on left) and the number of events with each event selection criteria (on right) is plotted using the HIJING General Purpose (LHC20e3a) MC production at the reconstructed level.

3.3 Track and Topological Selection

An event in heavy-ion collisions produces thousands of particles that come out of the fireball and hit the detectors. The particles that are stable inside the detectors can be identified and studied. But not all these particles are primary. Primary particles are those that are produced in the initial interactions of beams. But there are also contributions coming from interactions with the materials of the detectors which are called secondary particles. Just like some events are not good for analysis and event selection criteria are required, tracks also go through selection procedure. The track selection is done according to the analysis requirements and detector acceptance in the region of interest. In this analysis, we are interested in the primary kaons that are produced in the initial collisions. There are several variables such as number of clusters in the TPC tracks, TPC-ITS match, distance from the origin of the track to the nominal collision point etc that decide the quality of the track. In ALICE, we use a system of predefined track selection criteria, that are checked by reading the filterbit of a track to ensure a minimum track quality. There are various filterbits based on how loose or tight we want the criteria to be. Following are the filter bits used in this analysis.

- filter bit 128 – TPC Only tracks. Default filterbit used in this analysis.
- filter bit 96: global tracks with strict DCA (32 + 64, where 32 requires at least one cluster in the SPD and 64 requires at least one cluster in the SDD) - used for systematic error estimation.
- filter bit 768: hybrid tracks (Require TPC, ITS refit, At least one hit on SPD) - used for systematic error estimation.

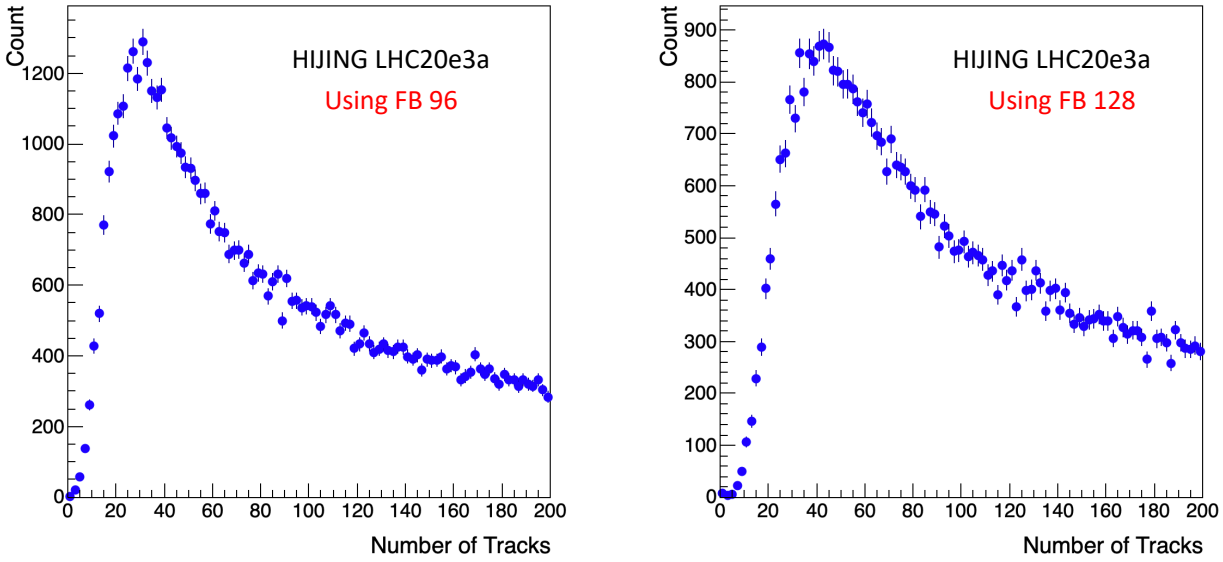

Figure 3.2: Distribution of number of tracks in different filterbits (Using the HIJING General Purpose (LHC20e3a) MC production at the reconstructed level)

The total number of particles produced in a collision is called multiplicity. It is an important observable used to characterize the complexity and energy density of the collision. A comparison of multiplicity distribution using filterbit 96 and 128 is shown in the Fig. 3.2. Apart from the cuts implemented in above filter bits, additional cuts are also applied for selecting and identifying the particles for analysis. The process of determining the type of particles produced in the collision is called particle identification (PID). The charged and neutral kaon identification criteria are described in the sections below. For the neutral kaons, there are both track selection criteria that are applied to the daughter tracks and geometrical cuts based on the topology of the decay process. Both neutral and charged kaon tracks are selected in a transverse momentum range from 0.6 GeV/c to 1.5 GeV/c and pseudorapidity, $|\eta| < 0.8$.

3.3.1 Charged Kaon ($K^{\pm}$) Selection

The charged kaons are identified based on the combined signals measured in the TPC and TOF detectors. Every track reconstructed in these detectors have an associated $|n\sigma|$ which indicates the probability of that track being identified as a specific particle. The nσ for tracks are defined separately based on whether TPC or TOF is used to identify the track and are denoted by $n\sigma_{\mathrm{TPC,K}}$ and $n\sigma_{\mathrm{TOF,K}}$ respectively. This analysis utilizes information of $n\sigma$ from both TPC and TOF detectors to select a good quality kaon tracks. A detailed discussion on its definition and $n\sigma$ PID method was provided in the context of TPC and TOF description in Section 2.3.

From the energy loss vs momentum distribution of the tracks, it is observed that the kaons are contaminated by other misidentified tracks (i.e, electrons, pions and protons). Therefore track rejections are applied to increase the purity of the kaon sample. The contamination from pions increases as the momentum increases. The following track selection and track rejection criteria, based on the nσ values are used as the default PID method in this analysis.

- The $K^{\pm}$ are accepted for, $n\sigma = \sqrt{n\sigma^2_{\mathrm{TPC,K}} + n\sigma^2_{\mathrm{TOF,K}}} < 2.0$.
- The tracks are rejected if following conditions are met.
  - If the track passes the PID n$\sigma < 3.0$ cut for more than one particle species (in the set of pions, kaons, and protons), it is rejected.
- Electron rejection: The tracks are rejected if $n\sigma_{\mathrm{TPC,\ e}} < 3.0$.

The filterbit 128 containing the tracks from TPC is used as the default filterbit. TPC clusters are points where the particle's ionization energy loss is measured and a track can have a maximum of 159 clusters. The standard criterion used in ALICE sets the minimum number of TPC clusters required for a track to be 70. The χ^2/ndf per TPC cluster is a

measure of the goodness of fit for the track model to the observed data and is set as 4. To ensure tracks are close to the primary vertex, two selection criteria are applied: one in the xy-plane and one along the z-axis. The distance of closest approach (DCA) of a track to the primary vertex must be less than 0.3 cm in the transverse plane (xy) and less than 1.0 cm along the z-axis. A summary of the track cuts used for selecting the $K^{\pm}$ tracks are given in the Table 3.4.

Table 3.4: The default track selection criteria for charged kaons ($K^{\pm}$)

Transverse momentum	$0.6 < p_T < 1.5$ `GeV/c`
Pseudorapidity	$\|\eta\| < 0.8$
Filterbit	128 (TPC only tracks)
Minimum number of TPC Clusters	70
χ^2/ndf per TPC cluster	4
nσ selection	$n\sigma_{TPC,TOF} < 2.0$
nσ rejection	$n\sigma_{TPC,TOF} < 3.0$ for $\pi^{\pm}$, $K^{\pm}$ and p($\bar{p}$)
Electron rejection	$n\sigma_{TPC,e} < 3.0$
DCA to vertex-xy	0.3 cm
DCA to vertex-z	1.0 cm

A comparison of the energy loss (dE/dx) vs transverse momentum (p_T) distribution using HIJING reconstructed tracks, before and after the electron rejection cut is shown in Fig. 3.3. In the right panel, we see that a band corresponding to electrons is removed as expected. The effect of electron rejections seems to affect largely at p_T of around 0.5 GeV as one would expect because that's where the energy loss bands of kaons and electrons seem to have most overlap. In Fig. 3.4, dE/dx vs p_T of K^+ and K^- are shown after all the track rejections.

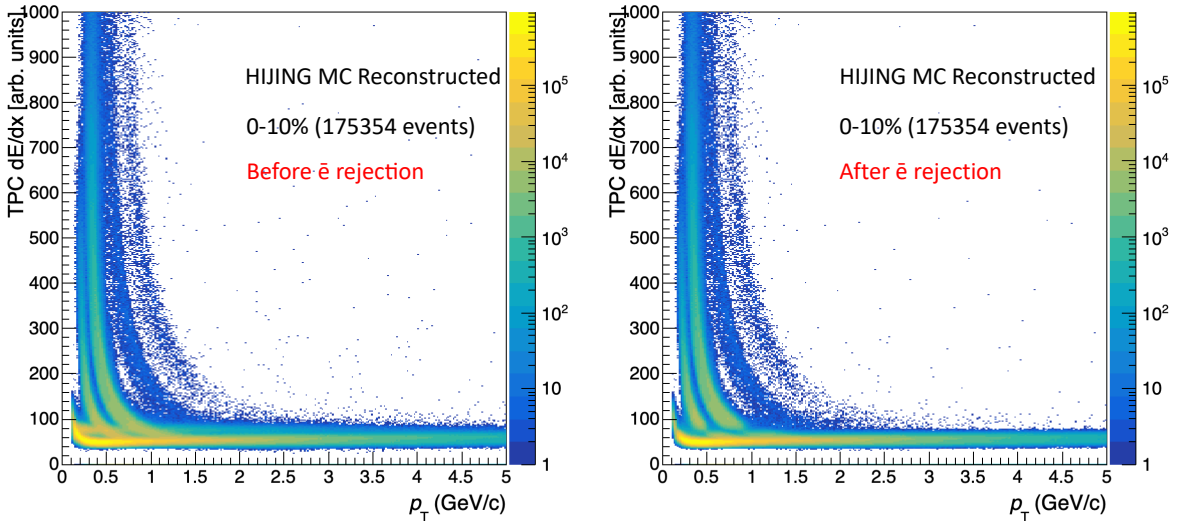

Figure 3.3: Energy loss (dE/dx) vs transverse momentum (p_T) of the identified tracks before (on right) and after (on left) electron rejection cut is applied. (Using the HIJING General Purpose (LHC20e3a) MC production at the reconstructed level)

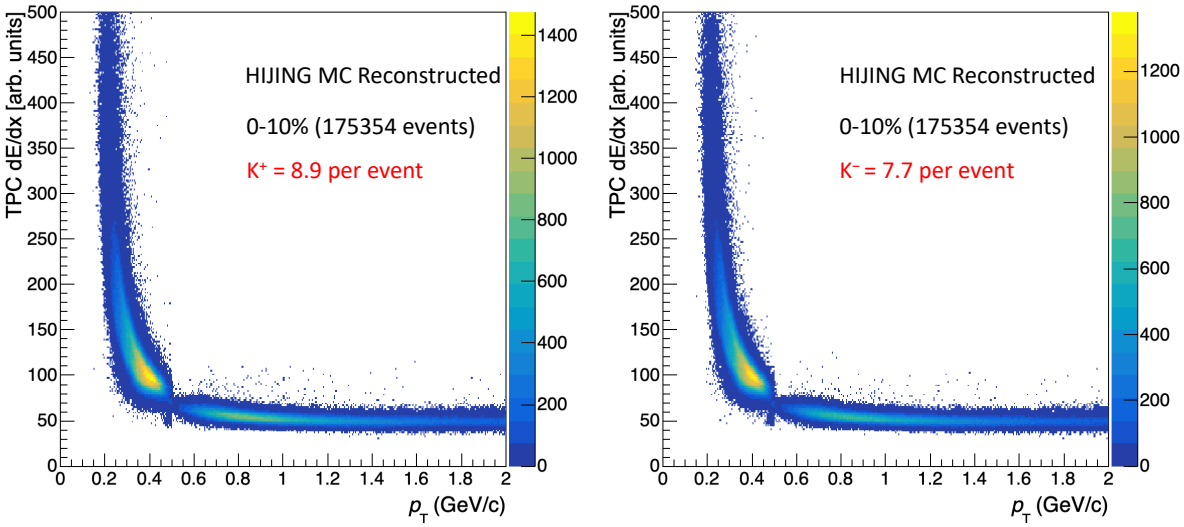

Figure 3.4: Energy loss (dE/dx) vs transverse momentum p_T of K^+ (on left) and K^- (on right) (Using the HIJING General Purpose (LHC20e3a) MC production at the reconstructed level)

3.3.2 Neutral kaon (K^0_S) Selection

As neutral particles do not leave a track in the time projection chamber, they must be reconstructed from the daughter particles into which they decay. The identification of neutral kaon is carried out based on the weak decay $K^0_S \rightarrow \pi^+ + \pi^-$. These decays are identified from the V0 decay topology of the particle. When a particle decays and hence no longer exists, its mass before the decay can be calculated from the energies and momenta of the decay products (here, $\pi^+\pi^-$ tracks) using the conservation of four momentum using the following equation given in Eqn. (3.1). The invariant mass of K^0_S can be calculated utilizing this equation. The `AliAODV0` class of AliRoot is used for the reconstruction procedure.

$$m_{inv} = \sqrt{(E_1 + E_2)^2 - |\vec{p_1} + \vec{p_2}|^2} = \sqrt{m_1^2 + m_2^2 + 2(E_1 E_2 - \vec{p_1}.\vec{p_2})} \tag{3.1}$$

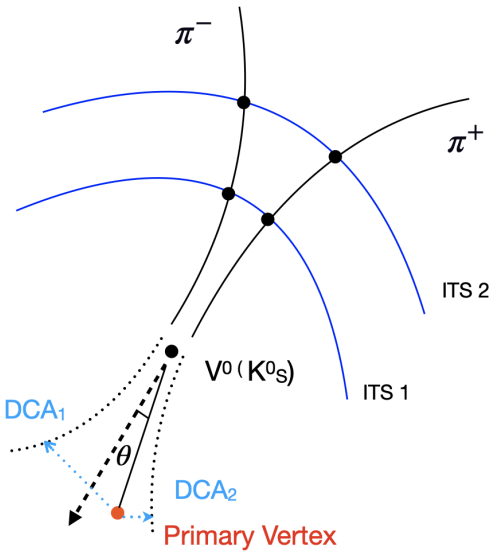

Figure 3.5: The decay topology of K^0_S

Table 3.5: The default track and topological selection criteria for neutral kaons (K^0_S)

Transverse momentum	$0.6 < p_T < 1.5$ GeV/c
Pseudorapidity	$\|\eta\| < 0.8$
DCA of daughter to the primary vertex (PV)	> 0.1 cm
DCA between the daughter pions	< 1.0 cm
Decay length	$< 4\ c\tau$
Radius of V0	$> 5\ cm$
Armenteros-Podolanski cut	$p_{\mathrm{T}}^{\mathrm{ARM}} > 0.2\alpha$
$\|n\sigma\|$ of daughter pion tracks	≤ 2
Number of TPC clusters of daughter tracks	< 70
Invariant mass selection	$0.485 < m_{\pi^+\pi^-} < 0.510$ GeV/c^2
Cosine of pointing angle	> 0.998

A diagram illustrating the decay topology of K^0_S is shown in Fig. 3.5. The primary vertex (PV) is depicted as a red point, where any primary particle must ideally originate from. The secondary vertex is where the K^0_S will undergo its decay after traveling a certain distance, which is known as the decay length. The maximum DCA between the daughter tracks is set to be 1.0 cm. The minimum DCA between each daughter track to the PV is set as 0.1 cm. The Armenteros–Podolonski cuts are used to remove the contamination from Λ tracks. The histogram of p_T^{ARM} Vs. α plotted before and after applying the Armenteros–Podolonski cut is given in Fig. 3.6. These variables are defined below.

1. Transverse momentum p_T^{arm} (not with respect to the beam axis but the direction of the mother)

2. α as a measure of the asymmetry of the longitudinal momenta of the daughters:

$$\alpha = \frac{p_L(+) - p_L(-)}{p_L(+) + p_L(-)}$$

The minimum radius of reconstructed V0 (K^0_S) is set to 5 cm. The minimum value of Cosine of pointing angle (Cos(PA)) is set to be 0.998. The pointing angle is the angle between the momentum vector of the reconstructed K^0_S and the vector connecting the PV to the decay vertex (secondary vertex) of the K^0_S. In ideal case where the K^0_S is perfectly aligned with the vector pointing from PV to the decay vertex, Cos(PA) will be unity suggesting maximum probability that decaying particle originated from the PV. The decay length of K^0_S is 2.68 cm and the maximum decay length of the reconstructed track is set as 4 times 2.68 cm. The reconstructed K^0_S tracks are selected in a p_T range from 0.6 GeV/c to 1.5 GeV/c and $|\eta| < 0.8$. The default selection criteria used to get a K^0_S sample as displayed in Fig. 3.7 are summarized in the Table. 3.5.

To estimate the purity K^0_S sample, defined as signal/(signal+background), the invariant mass distribution is fitted with a sum of a Lorentzian function and a second-degree polynomial function. This fit is shown by the blue line. Additionally, the distribution excluding the signal region (0.485, 0.510) GeV/c^2 is fitted with a second-degree polynomial, shown by the red line. The estimated purity in the 0–10% centrality interval is 79%.

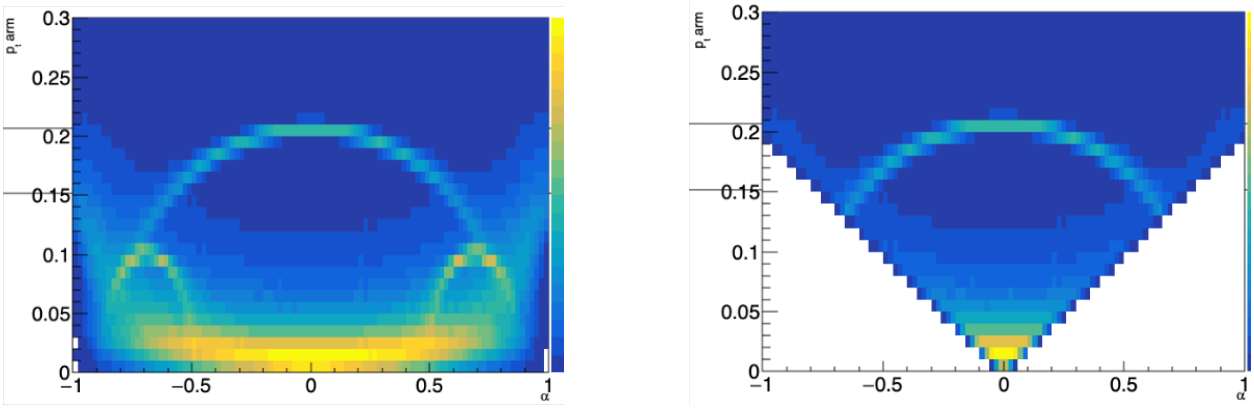

Figure 3.6: The distribution of p_T^{ARM} Vs. α (a) before and (b) after applying the Armenteros–Podolonski cut.

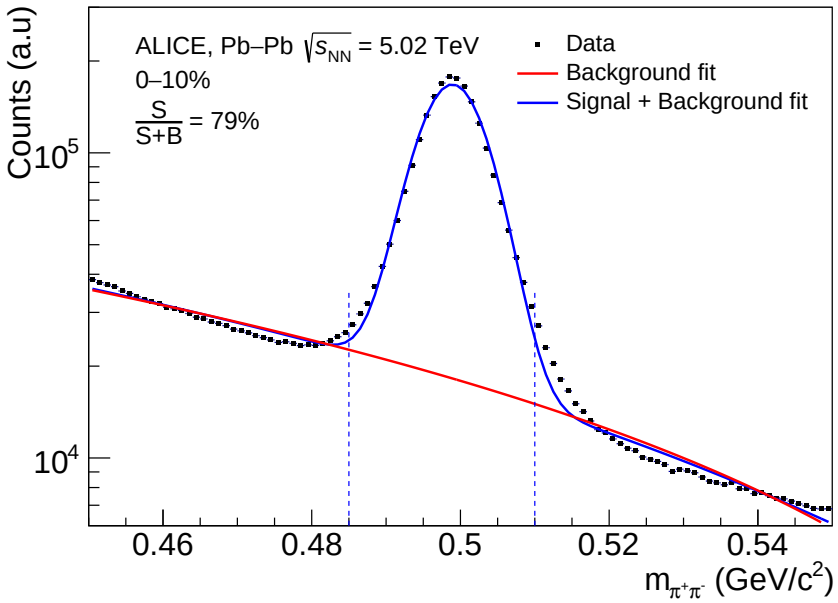

Figure 3.7: The invariant mass distribution of K^0_S using default selection criteria used in this analysis

The invariant mass distributions using the default selection criteria for various centrality intervals of 0–10%, 10–30%, 30–50% and 50–90% are shown in Fig. 3.8. The corresponding purity values calculated are also given in the canvas of each distribution. To increase the purity of K^0_S, the selection criteria needs to be stricter. The invariant mass distributions obtained using a tighter topological selection criteria is given in Fig. 3.9. Along with the cuts described above, an additional requirement on the maximum value of DCA between V0 and PV is set to be 0.1 cm. As expected, this strict DCA requirement significantly increases the purity of the kaon sample (around 98% for all centrality intervals), but it also considerably reduces the statistics. As correlations require higher statistics, we use the strict selection criterion for the systematic error estimation in order to account for the contamination.

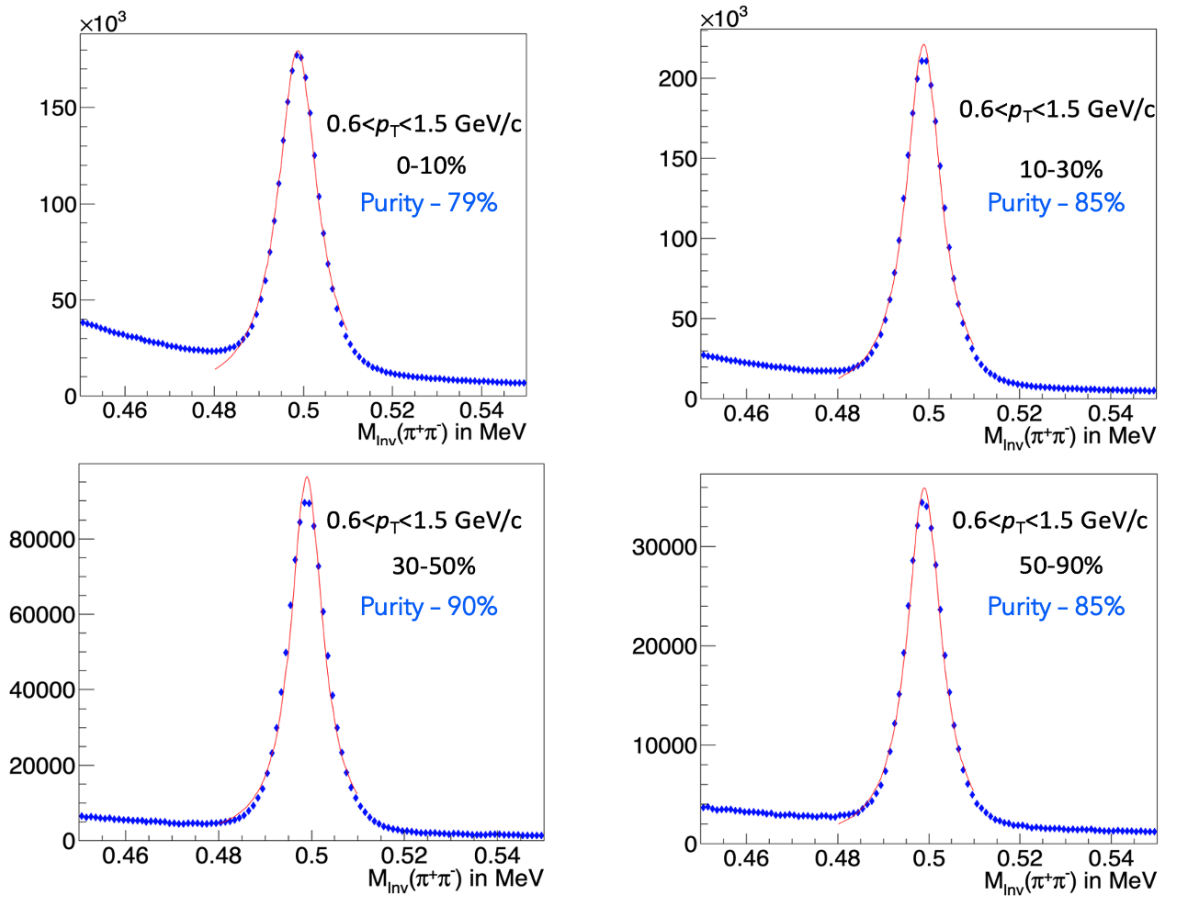

Figure 3.8: The invariant mass distribution of K^0_S using the Pb–Pb data at $\sqrt{s_{NN}} = 5.02$ TeV in different centralities by applying the default reconstruction criteria given in Table 3.5 is plotted. The distribution in the invariant mass range of (0.45, 0.55) is fitted with a sum of Lorentzian function and a polynomial function of degree 2.

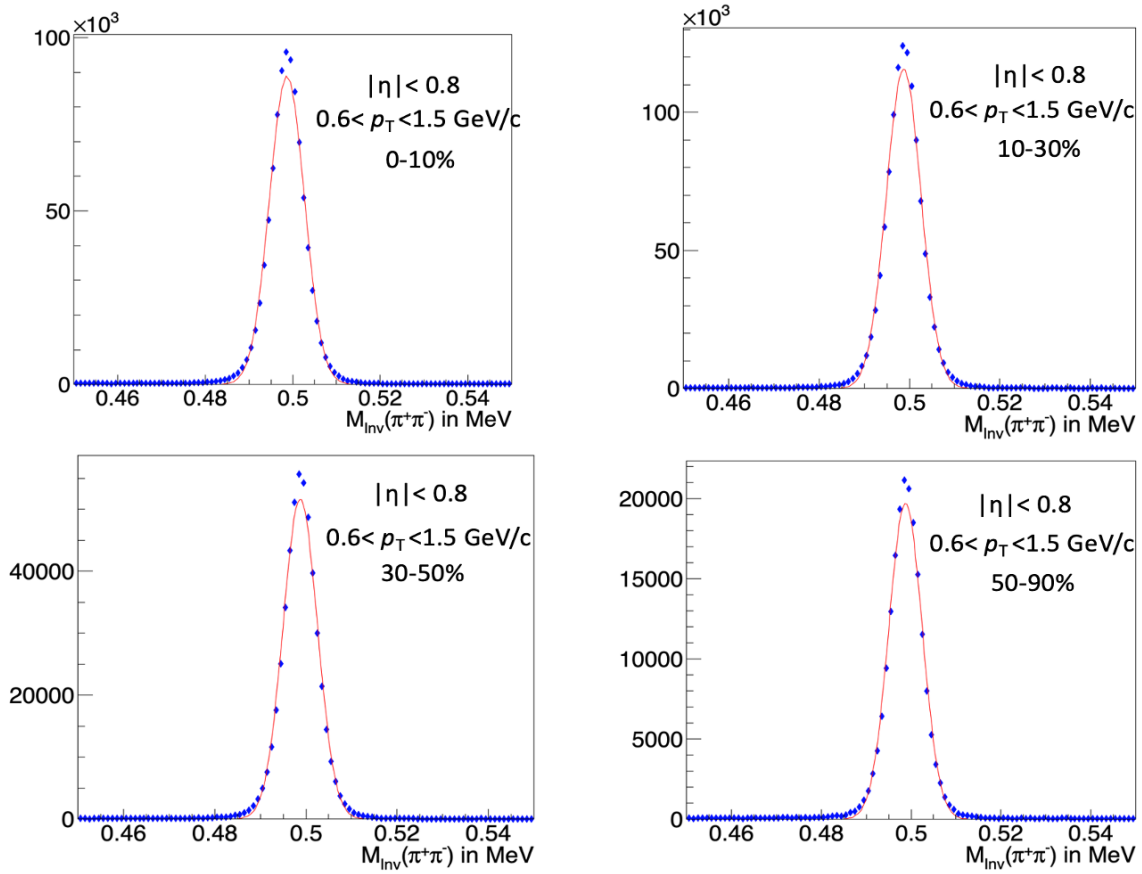

Figure 3.9: The invariant mass distribution of K^0_S using the Pb–Pb data at $\sqrt{s_{NN}} = 5.02$ TeV in different centralities by applying strict DCA cuts is plotted. An additional cut on DCA from V0 to PV is added to the default selection criteria.

3.4 Analysis Observable, $C(\Delta\varphi, \Delta\eta)$

The two particle correlation function is a common concept used to describe the relationship between the properties of two particles, which may be either identical or non-identical. For two particles of type 1 and 2, correlation function can be defined as the ratio of two-particle distribution, denoted as $P_{12}(x_1, y_1, x_2, y_2)$ and the the product of the single-particle distributions, $P_1(x_1, y_1)$ and $P_2(x_2, y_2)$ where x and y denote the properties of interest. Mathematically, this is represented as:

$$C(x_1, y_1, x_2, y_2) = \frac{P_{12}(x_1, y_1, x_2, y_2)}{P_1(x_1, y_1)P_2(x_2, y_2)} \tag{3.2}$$

In this analysis, we measure the experimental two-particle angular correlation function denoted by $C(\Delta\varphi, \Delta\eta)$ as a function of $\Delta\varphi$ and $\Delta\eta$, the difference in azimuthal angle (η) and pseudorapidity (φ) of the two particles produced in the same event.

3.4.1 Azimuthal angle and Pseudorapidity

The collider experiments usually employ a Cartesian co-ordinate system in which the z-axis is aligned with the beam direction, while the x and y axes define the transverse plane orthogonal to the beam. In this system a particle's three-momentum $\vec{p} = (p_x, p_y, p_z)$ is decomposed into a longitudinal component p_z along the z axis and a transverse component $p_T \equiv (p_x, p_y)$ within the transverse plane.

- Azimuthal angle (φ): Angle made by the particle trajectory and the x-axis.

$$\varphi = \tan^{-1}\left(\frac{p_y}{p_x}\right) \in (0, 2\pi) \tag{3.3}$$

- Pseudorapidity (η): Defined as a function of θ, the angle made by the particle trajectory with the beam pipe or z-axis in our convention.

$$\eta = -\ln \tan\left(\frac{\theta}{2}\right) \tag{3.4}$$

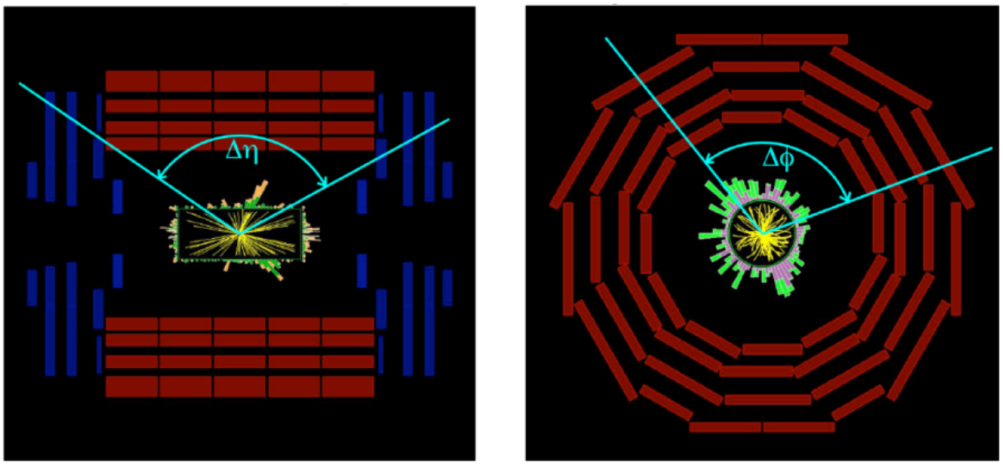

Figure 3.10: Depiction of angular differences of particle tracks denoted by $\Delta\eta$ and $\Delta\varphi$ with a cross sectional view of a detector. The yellow lines are the tracks of the charged particles and the green and pink bars show the energy deposition in the calorimeters. This energy deposition is not relevant for this analysis.

3.4.2 Angular Correlation Function

Two particle angular correlation functions are a robust tool that allows for exploration of underlying physics phenomena of particle production during collisions (protons and heavy ions) by measuring the distributions of angles in $\Delta\eta\Delta\varphi$ space. This section details the mathematical definition and construction of the angular correlation function. The numerator of the angular correlation function can be interpreted as a joint probability to observe a particle with azimuthal angle, φ_1 and pseudorapidity η_1 if a second particle with azimuthal angle jφ_2 and pseudorapidity η_2 is observed as well, and distributions $P_1(x_1, y_1)$ and $P_2(x_2, y_2)$ in the denominator as probabilities of observing particles with φ_1 and η_1, and φ_2 and η_2, respectively.

$$
\begin{aligned}
C(\Delta\varphi, \Delta\eta) &= \frac{P_{12}(\varphi_1, \eta_1, \varphi_2, \eta_2)}{P_1(\varphi_1, \eta_1) P_2(\varphi_2, \eta_2)} \\
\Delta\eta &= \eta_1 - \eta_2 \\
\Delta\varphi &= \varphi_1 - \varphi_2
\end{aligned}
\tag{3.5}
$$

$$
\begin{aligned}
C(\Delta\varphi, \Delta\eta) &= \frac{S(\Delta\varphi, \Delta\eta)}{B(\Delta\varphi, \Delta\eta)} \\
S(\Delta\varphi, \Delta\eta) &= \frac{1}{N_{\text{pairs}}^{\text{signal}}} \frac{d^2 N_{\text{pairs}}^{\text{signal}}}{d\Delta\varphi d\Delta\eta} \\
B(\Delta\varphi, \Delta\eta) &= \frac{1}{N_{\text{pairs}}^{\text{mixed}}} \frac{d^2 N_{\text{pairs}}^{\text{mixed}}}{d\Delta\varphi d\Delta\eta}
\end{aligned}
\tag{3.6}
$$

The numerator shown in Fig. 3.11a represented by $S(\Delta\varphi, \Delta\eta)$ is the signal distribution which is constructed using the particle pairs from the same events. The denominator, represented by $B(\Delta\varphi, \Delta\eta)$ given in Fig. 3.11b, is the reference distribution constructed using particle pairs from different events that are uncorrelated. Therefore, this reflects the single particle acceptance and is known as the background distribution that ideally contains only combinatorial background, absent of any genuine correlation signals. In event mixing procedure, each event is mixed with 10 different events that are similar in terms of multiplicity (events having $N_{ch} = 5$ wide multiplicity bin are mixed) and the position of primary vertex (events having 2 cm wide z-vertex bin are mixed). This strategy helps in modeling the background more accurately by ensuring that the mixed events are similar enough to maintain relevant physical properties while being different enough to minimize genuine correlations not related to detector artifacts or event-specific effects. This is especially important in correlation studies to differentiate between actual physical phenomena and statistical fluctuations or experimental biases.

Both the signal and background distributions are normalized to the number of pairs ($N_{\text{pairs}}^{\text{signal}}, N_{\text{pairs}}^{\text{mixed}}$) in the given distribution. The measurements are restricted to $-1.6 \leq \Delta\eta \leq 1.6$ and $-\pi \leq \Delta\varphi < \pi$, chosen according to the limited acceptance of the detectors used for particle identification. Finally the correlation functions were mirrored around the point $(\Delta\eta, \Delta\varphi) = (0, 0)$ and plotted in the range $-\frac{\pi}{2} < \Delta\varphi < \frac{3\pi}{2}$. In the absence of correlations, the ratio of signal and background distributions should equal unity. If the ratio is greater than unity, it means there is a positive correlation and if it is less than unity, there is a negative correlation or anti-correlation.

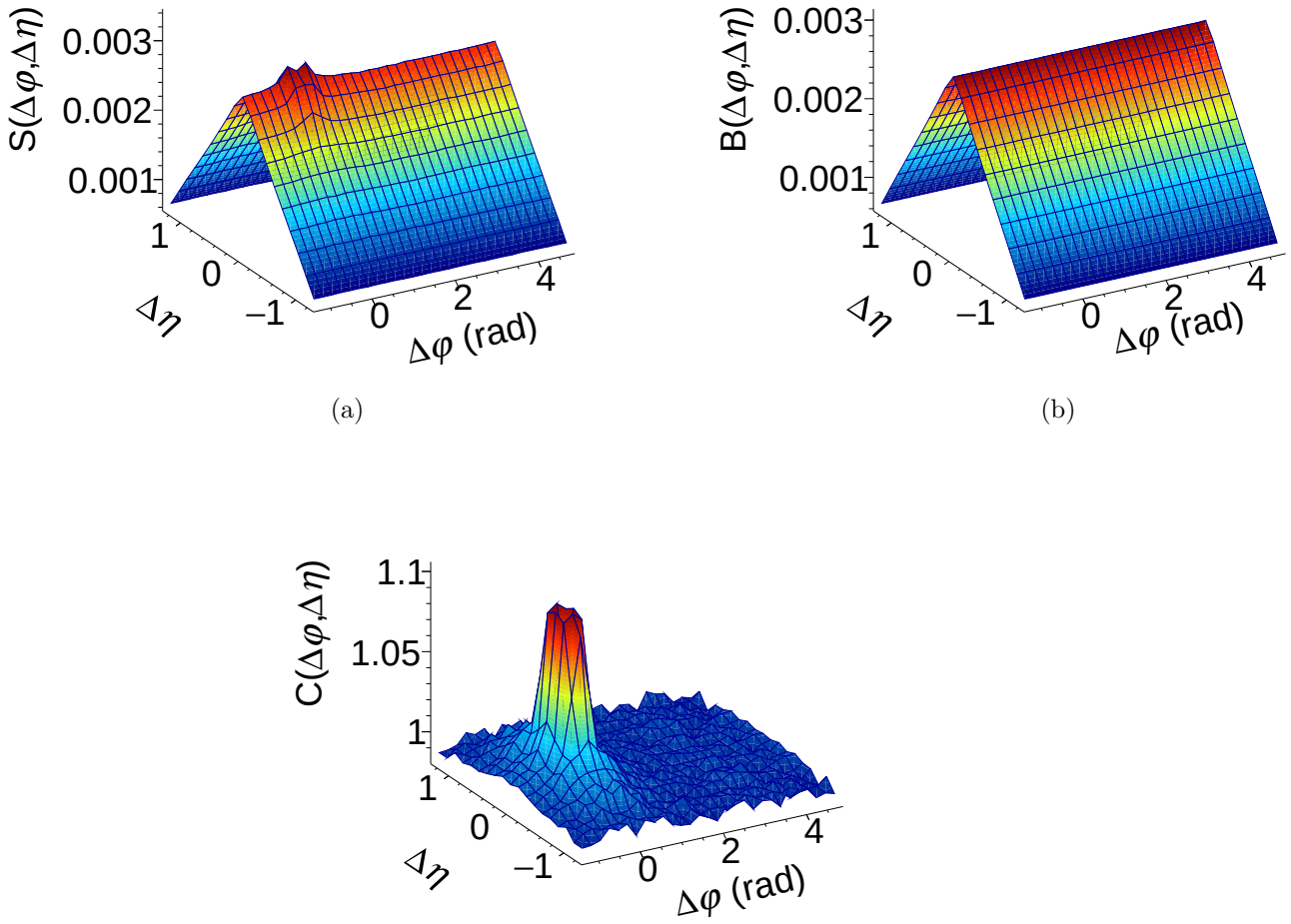

(a)

(b)

(c)

Figure 3.11: (a) The signal, $S(\Delta\varphi, \Delta\eta)$, (b) background, $B(\Delta\varphi, \Delta\eta)$ and (c) correlation function, $C(\Delta\varphi, \Delta\eta)$ obtained using HIJING General Purpose (LHC20e3a) production for K^+K^- pairs. Both the signal and background distributions are normalized to the number of pairs in each distribution.

3.5 Monte Carlo (MC) Simulation Studies

ALICE has a stable framework for simulating its complex detector geometries, transport of the particles and the various detector response mechanisms. To obtain a baseline for the correlations from real collision events and to correct these for the detector effects, simulation studies are performed using Monte–Carlo (MC) event generators such as HIJING and AMPT. There are two types of simulated MC data samples that are used for calculating the corrections and detector resolutions.

- MC Generated: The initial particles that are simulated by the event generator which does not go through transport codes and therefore represents the ideal scenario.
- MC Reconstructed: The generated particles are passed through transport codes for geometry and detector response. This is achieved in ALICE using simulation tools such as GEANT3 [94], GEANT4 [95], FLUKA [96] etc.

Simulating the transport and response of final state particles and the secondary particles produced from the interactions of particles within the material is a demanding task given the complexity and the number of sub detectors involved in the ALICE experiment. Of comparable complexity and diversity is the primary event generation that requires generating uncorrelated events, correlation between particles and a multitude of so called hard probes as well as any possible mixture between these components. The description of the general ALICE simulation strategy and those components of the framework related to simulation are given in [97].

3.5.1 Monte Carlo Generators

HIJING (Heavy Ion Jet INteraction Generator)

HIJING is a Monte Carlo event generator, developed in 1991 to study the jet and multiparticle production in high energy proton-proton (pp), proton-nucleus (pA), and nucleus-nucleus (AA) collisions [98–100]. This model incorporates mechanisms such as multiple minijet production, soft excitation, nuclear shadowing of parton distribution functions and jet interactions in dense hadronic matter. The physics contributions from resonance decays are also included. HIJING was initially written in FORTRAN and was rewritten in C++ with the possibility of inclusion of alternative physics processes and compatibility with experimental frameworks such as AliRoot used by ALICE experiment. HIJING includes initial and final state interactions, but does not include the evolution and therefore collective expansion effects like flow whereas a model like AMPT includes flow and is considered in our study.

AMPT (A Multi Phase Transport model)

AMPT model includes both initial partonic collisions and final hadronic interactions and the transition between these two phases of matter. It has four main components, namely, initialization of collisions, parton transport after initialization, hadronization mechanism and hadron transport. A brief discussion of the modifications made to the default HIJING fragmentation scheme and ART 3 hadron evolution is given in [101]. A description of how the different components of AMPT model, that uses HIJING for generating the initial phase space distribution of partons, Zhang's Parton Cascade (ZPC) for modeling partonic scatterings [102], the Lund string fragmentation model or a quark coalescence model for hadronization, and A Relativistic Transport (ART) model for treating hadronic scatterings, are improved and combined to give a coherent description of the dynamics of relativistic heavy ion collisions is given in [103].

3.5.2 Monte Carlo Corrections

In detectors, distinction of primary and secondary particles is crucial for drawing conclusions about the particle production mechanisms. Primary particles are the particles produced in the collisions between beams, that initially enter the detector. Secondary particles are those produced from the interactions of the primary particles within the detector via weak or strong nuclear decays, scattering, ionization etc. In MC simulations, the detector geometry is assumed and particles are generated in conditions that match the real experimental conditions. By looking at the generated and reconstructed particle count using the MC data, we can estimate the detector performance, data corrections etc.

The MC correction variables are estimated utilizing the HIJING model and are described in this chapter. This section details the definition and procedure for estimating efficiency, purity, contamination, and the final correction factor used in the correlation function corrections. The final correction factor for the correlation function considers the contribution from both the detector efficiencies and contamination from secondary particles. Additionally, we use the HIJING framework to measure corrected correlation functions at both generated and reconstructed levels, to perform the closure test. The results of the Monte-Carlo closure test using the minimum-bias triggered events is also included. The final corrected correlations of neutral to charged ($K^0_S K^{\pm}$) and charged to charged (K^+K^-) kaons are calculated using both HIJING and AMPT models at the generated level and are shown in the next chapter.

Efficiency

Every detector is susceptible to potential loss of particles. This means the detectors can not reconstruct all the particles that are produced in the collisions. And in analysis we apply geometrical and kinematic cuts while selecting the particles which reduces the number of reconstructed particles even more. So, the raw particle yields need to be corrected for the

inefficiency. In MC simulations, the detector geometry is assumed and particles are generated in conditions that match the real experimental conditions. By comparing the number of generated and reconstructed primary particles in MC, the track reconstruction efficiency ϵ can be estimated. Because we reconstruct the particles within an acceptance region based on the detector geometry, efficiency is expressed as acceptance times efficiency. It is defined as the ratio of the number of particles actually measured to the number of particles that would have been measured in an ideal detector as in the the Eq. (**??**) below. We can loose particles during the track reconstruction or during the particle identification which is followed by reconstruction process. Therefore the total efficiency is a sum of tracking efficiency and PID efficiency. Reconstruction efficiency depends on various factors of the detectors.

$$\epsilon = \frac{N_{\text{rec, primary}}}{N_{\text{gen, primary}}} \tag{3.7}$$

Purity

When efficiency quantifies the reconstruction process, purity is what estimates its quality. Purity of particles refers to the ability to accurately identify particles of interest from the background noise and other particles created in the collision process. An estimate of purity can be obtained from MC simulations by verifying the generated information or the PDG of the reconstructed particles. When we try to increase the efficiency of particles using loose cuts, the purity of the sample becomes less as there are more chances of misidentifying the particles. Aim is to always find the optimum cuts that provide the efficiency and purity that best fits the analysis. The purity and total efficiency of K^+, K^- and K^0_S estimated using the default track selection criteria is given in the Fig 3.12.

$$P = \frac{N_{\text{rec, correct PDG}}}{N_{\text{rec, correct PDG}} + N_{\text{rec, incorrect PDG}}} \tag{3.8}$$

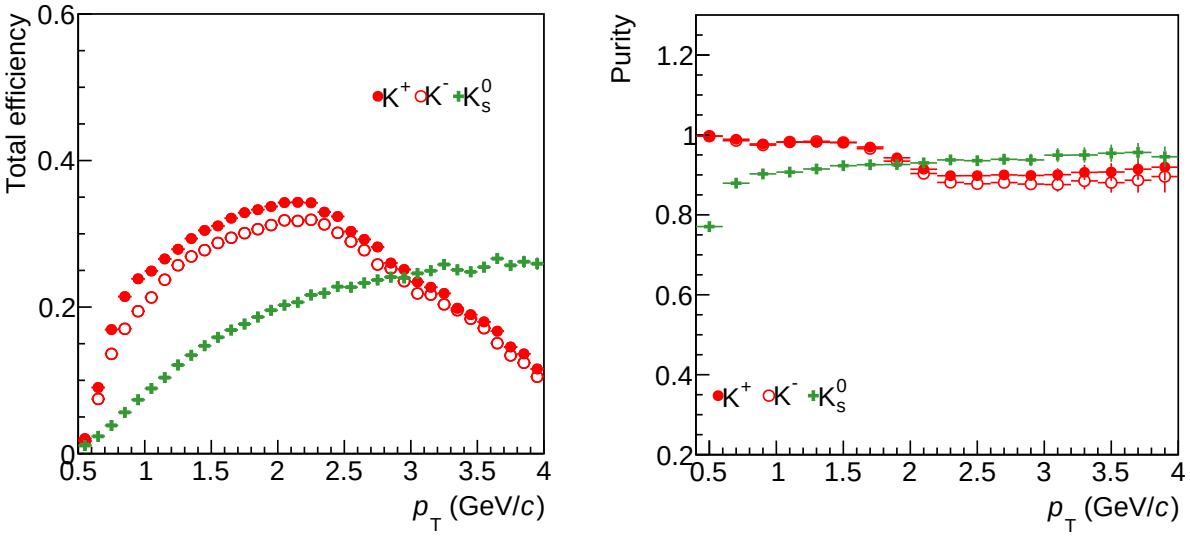

Figure 3.12: The efficiency and purity for K^+, K^- and K^0_S using the default particle selection criteria are shown. All values were obtained using HIJING General Purpose (LHC20e3a) production.

Factors Affecting Efficiency and Purity

As we make the particle selection criteria looser(stricter), it is expected that the detector efficiency increases(reduces) because more(less) particles pass the criteria. And as efficiency increases, the purity of the particle reduces and contamination increases. In the Fig 3.13, the default selection cuts for K^0_S is replaced by stricter cuts which reduces the overall efficiency of K^0_S. More specifically, the K^0_S efficiency is reduced by 50% at a p_T value of 2 GeV/c with these stricter cuts. And the integrated purity of K^0_S changes from 91.0% to 98.8%.

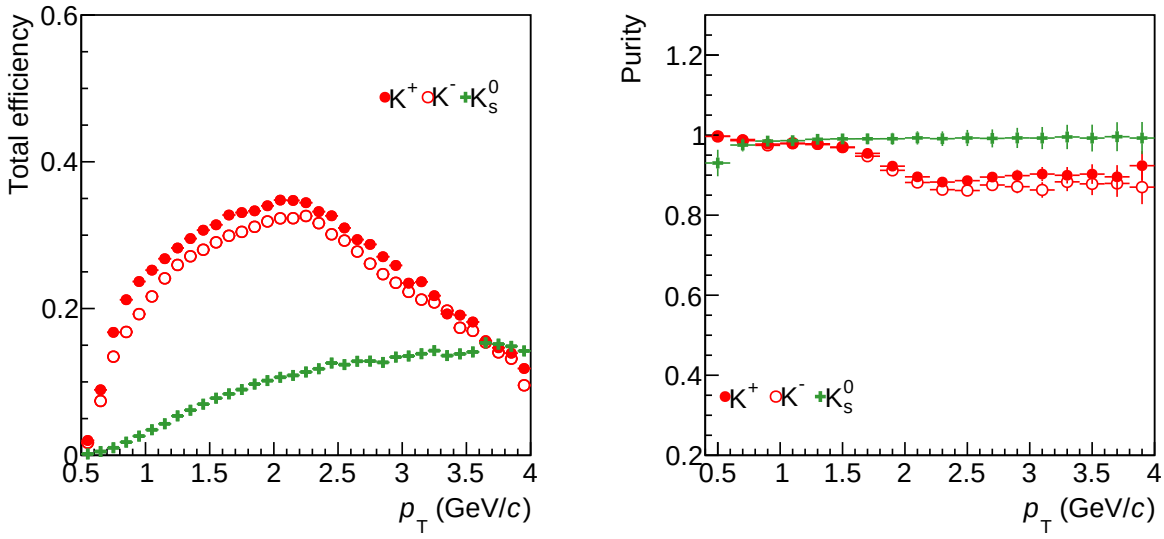

Figure 3.13: The efficiency and purity for K^+, K^- and K^0_S using the strict topological selection criteria for K^0_S. The K^+ and K^- are selected using the default criteria. All values were obtained using HIJING General Purpose (LHC20e3a) production.

Secondary Contamination

In this analysis, we are interested in a signal due to the correlations between primarily produced kaons. Therefore, secondary kaons are treated as a contamination. We can estimate the secondary contamination using the number of primary and secondary kaons that are present in the reconstructed MC sample. Secondary kaons can majorly arise from decays of resonances and other heavier particles that are primary. The Λ and Σ baryons classified as hyperons containing one or more strange quarks can decay to kaons. There are heavier mesons such as charmed D^+, D^0 mesons that decays to kaons. And there are resonances that decays to kaons via strong force like $\phi(1020) \rightarrow K^+ + K^-$: The phi meson, a resonance that decays predominantly into a pair of charged kaons. In the actual collision data, distinguishing primary kaons from kaons coming from secondary interactions is not a straightforward task and sometimes impossible. This is possible in MC and the definition for secondary contamination in terms of the number of primary and secondary reconstructed kaons is as

following. The values obtained for K+, K^- and K^0_S particles using HIJING MC production is given in the left of Fig. 3.14 and is used for correcting the particle pairs in the final correlation functions.

$$\mathbf{C_{sec}} = \frac{N_{\text{rec, secondary}}}{N_{\text{rec, primary}} + N_{\text{rec, secondary}}} \tag{3.9}$$

Correction Factor

The final correction factor, f used for correcting the correlation functions combines the information from both efficiency and secondary contamination.

$$N_{gen} = fN_{\text{rec}} = f(N_{\text{rec, primary}} + N_{\text{rec, secondary}}) \tag{3.10}$$

Combining the above equation with the definition of secondary contamination (Eqn. (3.7)) and efficiency (Eqn. (3.9)), we get the equation for correction factor as given in Eqn. (3.11). The correction factor estimated is p_T dependent as given in the right panel of Fig. 3.14 and is applied for each particle pairs in the signal and background distributions according to the Eqn. (3.12) and Eqn. (3.13) where, $S^{'}(\Delta\eta, \Delta\phi, p_{T,1}, p_{T,2})$ and $B^{'}(\Delta\eta, \Delta\phi, p_{T,1}, p_{T,2})$ represents the uncorrected signal and background distributions respectively.

$$f = \frac{1 - C_{\text{sec}}}{\varepsilon} \tag{3.11}$$

$$S(\Delta\eta, \Delta\phi) = \sum_{p_{T,1}, p_{T,2}} f(p_{T,1}, p_{T,2}) \cdot S^{'}(\Delta\eta, \Delta\phi, p_{T,1}, p_{T,2}) \tag{3.12}$$

$$B(\Delta\eta, \Delta\phi) = \sum_{p_{T,1}, p_{T,2}} f(p_{T,1}, p_{T,2}) \cdot B^{'}(\Delta\eta, \Delta\phi, p_{T,1}, p_{T,2}) \tag{3.13}$$

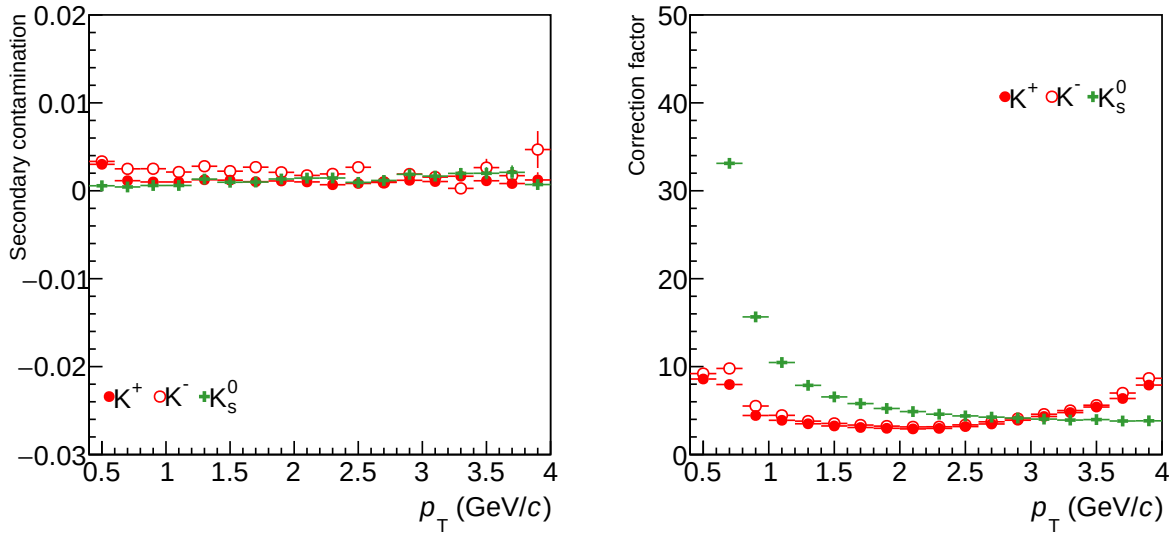

Figure 3.14: The secondary contamination and the final correction factor for K+, K$^-$ and K^0_S using the default particle selection criteria are shown. All values were obtained using HIJING General Purpose (LHC20e3a) production.

3.5.3 Monte Carlo Closure Test

Monte Carlo (MC) closure tests are critical for assessing the reliability and accuracy of particle reconstruction and data correction methodologies employed in analysing the particle collision data. Such tests serve as a benchmark to ensure that the deviations between simulated (generated) and experimentally reconstructed data are within acceptable uncertainty thresholds. For this particular closure test, LHC20e3a production is considered, a general purpose production based on the HIJING generator and the GEANT3 transport code, containing about 3.2×10^6 generated events. The angular correlation functions are calculated using the generated MC (true MC) and reconstructed MC data and are compared with each other. In an ideal world where detectors and our reconstruction procedure are 100% efficient, the results from both these data would provide exactly similar results. However, in practice, discrepancies arise due to inefficiencies and limitations inherent in the experimental setup and reconstruction algorithms. It is therefore crucial to ensure that these discrepancies

remain within known, quantifiable limits. The results from the closure test for $K^0_S K^{\pm}$ correlation function is displayed in Fig. 3.15. The 2D correlation functions of $K^0_S K^{\pm}$ using true MC and reconstructed MC are shown in the leftmost and middle panels of Fig. 3.15 respectively. The relative error between true and reconstructed MC correlation values captured by (reconstructed–generated)/reconstructed is shown in the rightmost panel of Fig. 3.15 which quantifies if the closure test is successful or not. Similarly, results using K^+K^- particle pairs are displayed in Fig. 3.16. To further validate the efficiency correction procedure, the correlation functions at the reconstructed level for both $K^0_S K^{\pm}$ and K^+K^- are scaled by the correction factor defined in the previous section. Due to the limited statistics available in the reconstructed data of the MC production, the verification of the closure test's success is conducted by fitting the correlation functions at the reconstructed level with a predefined mathematical model. The fitting function, given by Equation (3.14), is designed to approximate the correlation distributions at the generator level effectively. Successful agreement between these distributions confirms the robustness of the closure test, ensuring that the experimental setup and data processing techniques are capable of producing reliable results.

$$A \exp\left(-\frac{(x-\mu)^2}{2\sigma^2}\right) + A_0 \tag{3.14}$$

Where, A is the amplitude of the exponential component, which would model any peak in the correlation distribution, μ is the center of the peak in the correlation, σ is the standard deviation, indicating the width of the peak and A_0 is the constant that helps in aligning or normalizing the function to the baseline of the correlation, particularly addressing the "flat" region observed on the away side.

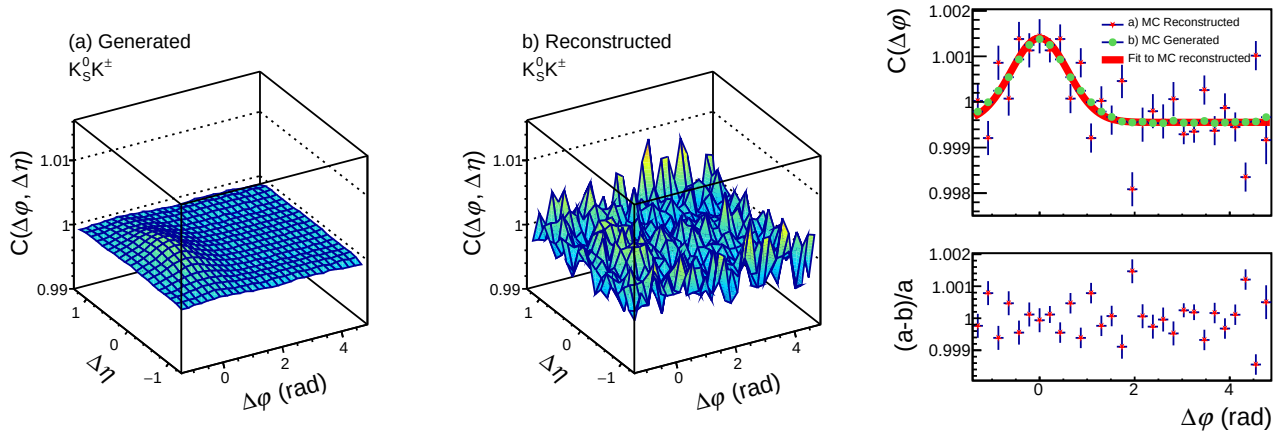

Figure 3.15: From left to right: 2D correlation function of $K^0_S K^\pm$ using MC generated, reconstructed and the corresponding $\Delta\varphi$ projections of the 2D correlations (upper panel) with the relative error of generated and reconstructed data points (lower panel) are displayed. All values were obtained using HIJING General Purpose (LHC20e3a) production.

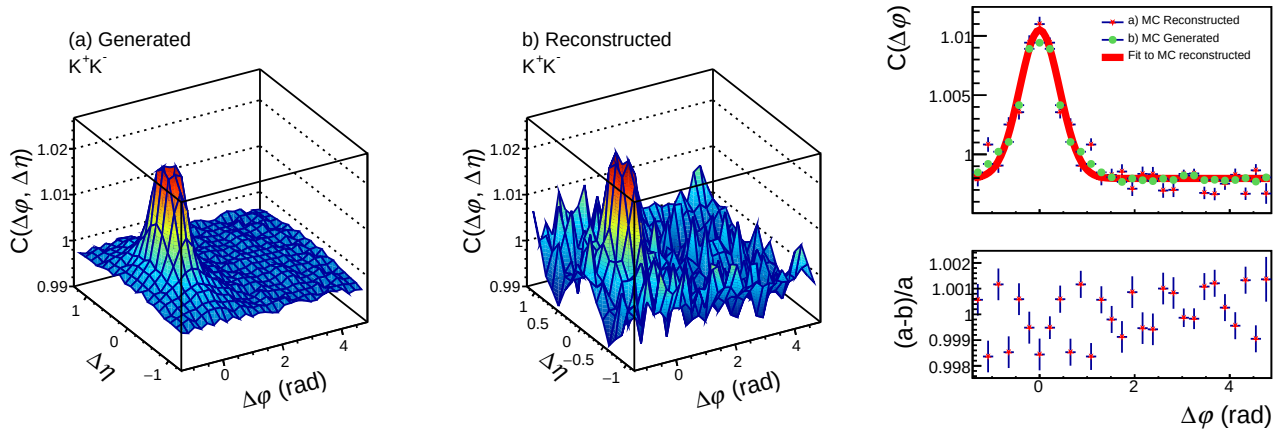

Figure 3.16: From left to right: 2D correlation function of K^+K^- using MC generated, reconstructed and the corresponding $\Delta\varphi$ projections of the 2D correlations (upper panel) with the relative error between generated and reconstructed data points (lower panel) are displayed. All values were obtained using HIJING General Purpose (LHC20e3a) production.

3.6 Estimation of Error

In this section, we discuss the estimation of statistical and systematic errors associated with our experimental measurements. Understanding and quantifying these errors is crucial for interpreting the reliability and accuracy of our data. We will discuss the methodologies employed to calculate these errors, examine the implications of their presence in our results, and ensure that our interpretations and conclusions are robust.

• **Statistical error:** Statistical errors, also known as random errors, arise from the inherent fluctuations in the measurement due to limited size of the data sample. These are unpredictable and vary from one measurement to another, even under the same conditions. The bin error of the histograms are computed in ROOT by default as the square root of bin content in case of unweighted histograms and as the square root of the bin sum of the weights square in case of weighted histograms. All the results are plotted with the statistical error even though in cases where large data samples are used, the errors may not be visible.

• **Systematic error:** Systematic errors in scientific experiments, refer to biases or inaccuracies that consistently skew results in one direction. These errors can arise from various sources including equipment calibration, experimental procedure, or theoretical assumptions. Identifying and correcting these errors is crucial to ensure the reliability and accuracy of experimental findings, as they can significantly impact the interpretation of data and the conclusions drawn from the research. The details on the estimation of systematic error is described in the section below.

3.6.1 Relative Systematic Uncertainty

The relative systematic uncertainty associated with the correlation functions denoted by $Syst.Err$ is calculated with the formula given in Eqn. (3.15) where, CF_{def} and CF_{var} are the values of the correlation function or the yield of particle pairs with the default and varied selection criteria respectively.

$$Syst.Err = \frac{|CF_{def} - CF_{var}|}{CF_{def}} \tag{3.15}$$

In this analysis, following variations in the analysis procedure are considered in order to estimate the systematic error associated with the $K^0_S K^{\pm}$ and K^+K^- correlations in $\Delta\varphi$ and $\Delta\eta$ directions. Both the default and varied parameters are given below. If there are two variations for one source of error, the maximum of the two uncertainties was taken into account. In all the cases, only one parameter was varied at a time.

- Filterbit for Track Selection: 128 (default) Vs 96/768 (Variation)
- nσ for $K^{\pm}$ Selection : 3.0 (default) Vs 2.0 (Variation)
- nσ for Electron Rejection : 3.0 (default) Vs 2.0 (Variation)
- PVz Cut for Event Selection : 10.0 cm (default) Vs 7.0 cm (Variation)
- Binning in PVz for Event Mixing: 10.0 (default) Vs 5.0 (Variation)
- Invariant Mass Cut for K^0_S Selection: Loose (Default) Vs Tight (Variation)
- Topological selection criteria for K^0_S: Loose (Default) Vs Tight (Variation)

The specific values of nσ for the $K^{\pm}$ selection and electron rejection are chosen according to the previous similar ALICE analyses. The events having primary vertex within $\pm$7 cm from the center of TPC are considered for systematic variation instead of the default value of $\pm$10 cm. The binning in primary vertex of events used for event mixing procedure for background construction is varied to 5.0 from 10.0. This increases the interval in PVz for selecting events with similar vertex for event mixing to 4.0 cm from the default value of 2.0 cm. The default invariant mass interval for selecting K^0_S is (0.485, 0.51) GeV/c. The variation considered is a stricter interval of (0.491, 0.505) GeV/c. In case of the selection criteria for K^0_S, the default cuts used are described in Table 3.5. The tighter cuts for the systematic variation include an additional criterion on the maximum value of DCA from V0 to PV, setting it to be 0.1 cm which significantly increases the purity of the K^0_S sample.

3.6.2 Systematic Variations in the $\Delta\varphi$ projection

A comparison of $\Delta\varphi$ projections of $K^0_S K^{\pm}$ taken in a symmetric $\Delta\eta$ interval of (-1.0,1.0) for all the systematic variations considered using the Pb–Pb collision data at $\sqrt{s_{\rm NN}} = 5.02$ TeV in centrality interval of 0–10% is shown in Fig. 3.17. The data values are also compared to the HIJING and AMPT model predictions. Similarly, the projections taken in case of K^+K^- correlation function is shown in Fig. 3.18. The AMPT model provides a better description of the correlation in case of $K^0_S K^{\pm}$ compared to that of K^+K^-, although the reasons for this discrepancy are not yet fully understood.

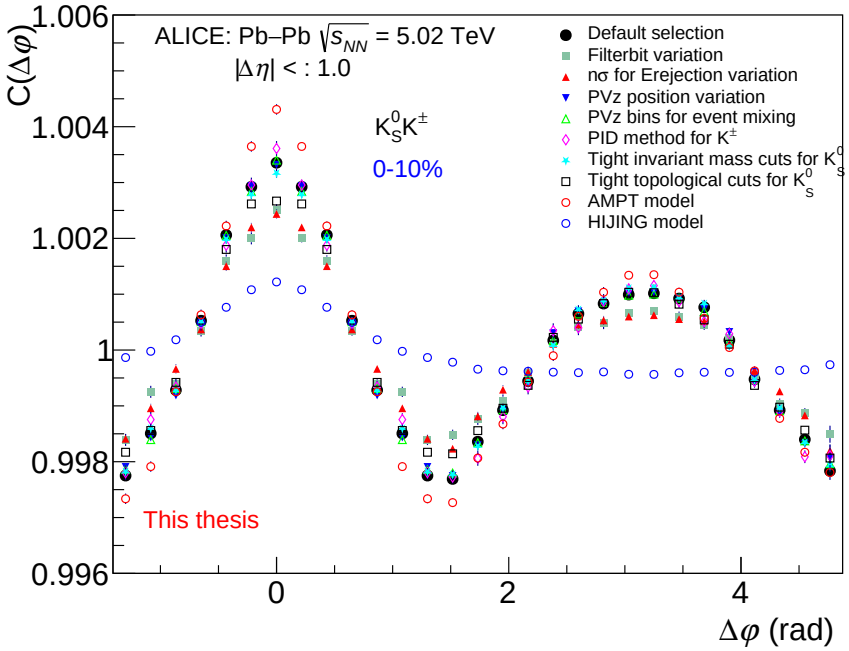

Figure 3.17: The comparison of $\Delta\varphi$ projections of $K^0_S K^{\pm}$ for all the systematic variations considered using the Pb–Pb collision data at $\sqrt{s_{\rm NN}} = 5.02$ TeV in centrality interval of 0–10%.

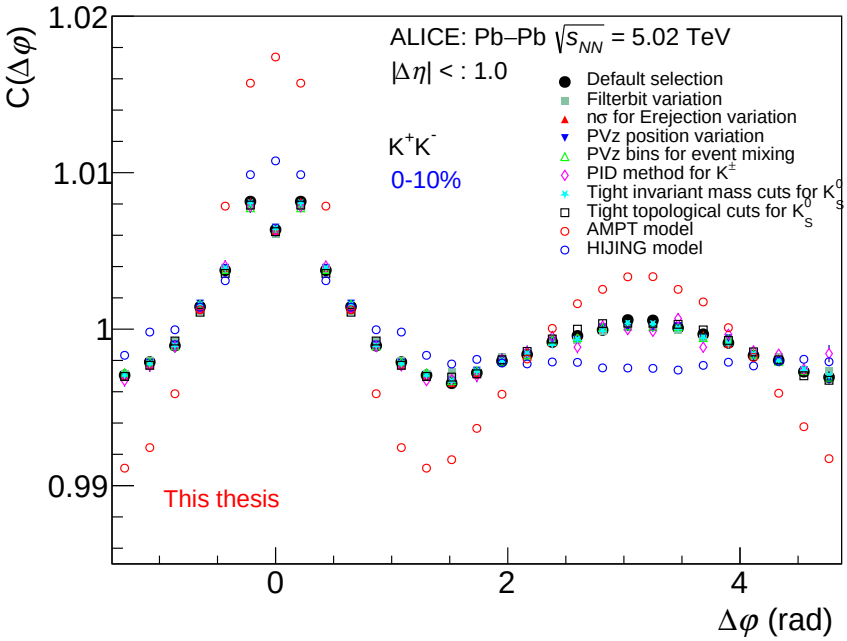

Figure 3.18: The comparison of $\Delta\varphi$ projections of K^+K^- for all the systematic variations considered using the Pb–Pb collision data at $\sqrt{s_{\rm NN}}$ = 5.02 TeV in centrality interval of 0–10%.

3.6.3 Systematic Variations in the $\Delta\eta$ projection

A comparison of $\Delta\eta$ projections of $K^0_S K^{\pm}$ taken in nearside ($\Delta\varphi < 0.9$ rad) range for all the systematic variations using the Pb–Pb collision data at $\sqrt{s_{\rm NN}} = 5.02$ TeV in centrality interval of 0-10% is shown in Fig. 3.19. The model predictions from AMPT and HIJING are also illustrated. It is seen that AMPT provides a good description of the data within the systematic error. As we make the cuts for selecting K^0_S stricter to match the criteria in the nu_{dyn} analysis, the data points are getting closer to the model predictions. Similarly, $\Delta\eta$ projections taken in nearside ($\Delta\varphi < 0.9$ rad) range for K^+K^- correlation function is shown in Fig. 3.20.

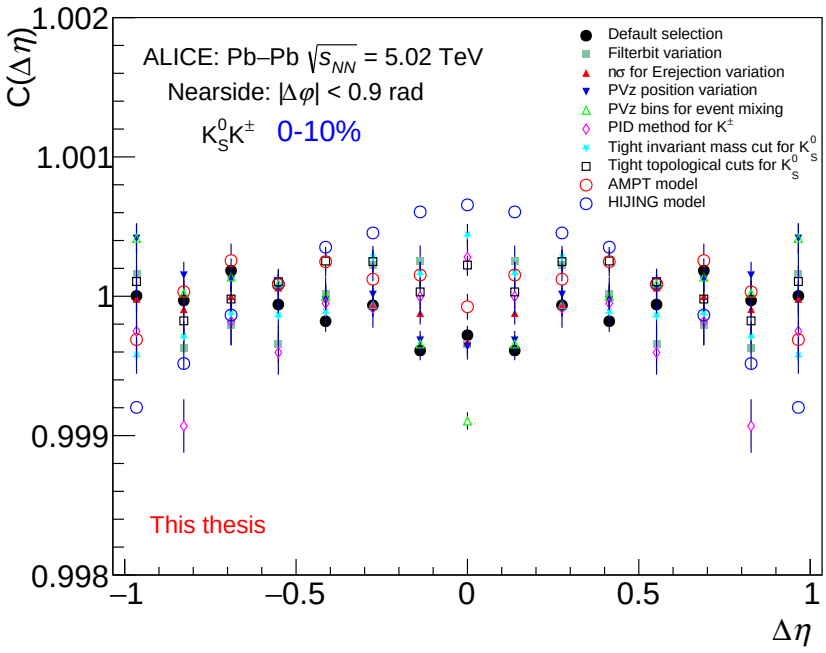

Figure 3.19: The comparison of $\Delta\eta$ projections of $K^0_S K^{\pm}$ for all the systematic variations considered using the Pb–Pb collision data at $\sqrt{s_{\rm NN}} = 5.02$ TeV in centrality interval of 0-10%.

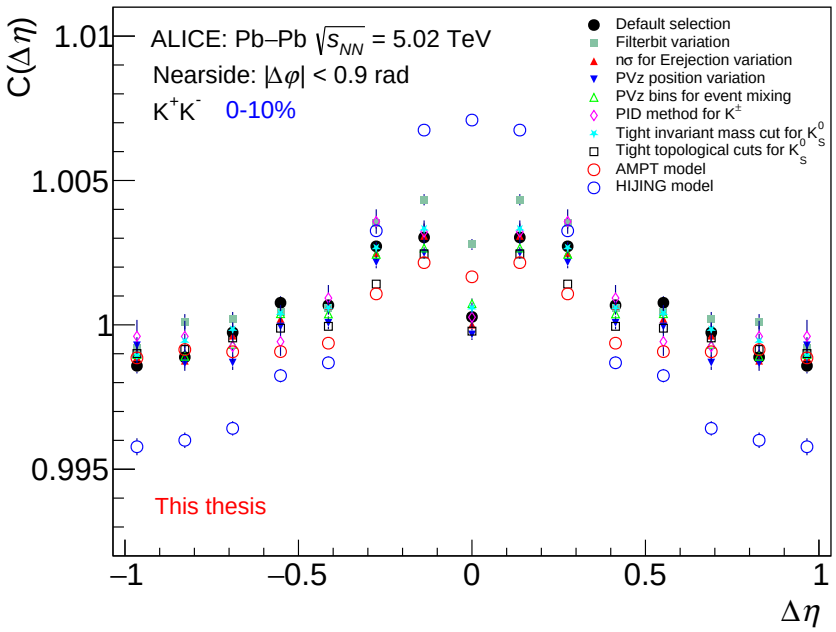

Figure 3.20: The comparison of $\Delta\eta$ projections of K^+K^- for all the systematic variations considered using the using the Pb–Pb collision data at $\sqrt{s_{\rm NN}} = 5.02$ TeV in centrality interval of 0-10%.

3.6.4 Barlow's Test

It can happen that some of the differences in the values of correlation functions after the systematic variations mentioned above are still within the statistical uncertainty. In such a case, this source should not be taken into account for the total systematic uncertainty as it would result in the over estimation of systematics. Barlow's checks are done for this purpose to estimate the statistical significance of systematic uncertainty. This technique was introduced by Roger Barlow in 2002 [104].

If the yield obtained from default measurement is denoted as CF_{def} and the yield from systematic variations is denoted as CF_{var}, the Barlow's variable denoted as n is calculated as follows.

$$n = \frac{|CF_{def} - CF_{var}|}{\sqrt{\sigma^2_{def} \pm \sigma^2_{var}}} \tag{3.16}$$

Subtraction in the denominator takes place when the default and systematic samples are entirely correlated, meaning one is a subset of the other; otherwise, the errors are added in quadrature. The threshold value, represented by the dotted red line in the plots below, is 1. If at least 1/3 of the Barlow control points surpass this value, the systematic control is statistically significant and will contribute to the final systematic uncertainty. It was observed that all the sources of systematic variations considered fail the Barlow test and therefore are included in the total estimation of uncertainty. As an example, results from Barlow's test for the Filterbit variation in $\Delta\eta$ projection of $\mathrm{K}^0_S\mathrm{K}^{\pm}$ correlation for various centrality intervals are given in Fig.3.21 and Fig.3.22. Similarly, results from $\Delta\varphi$ projection of $\mathrm{K}^0_S\mathrm{K}^{\pm}$ correlation for various centrality interavls are given in Fig.3.23 and Fig.3.24.

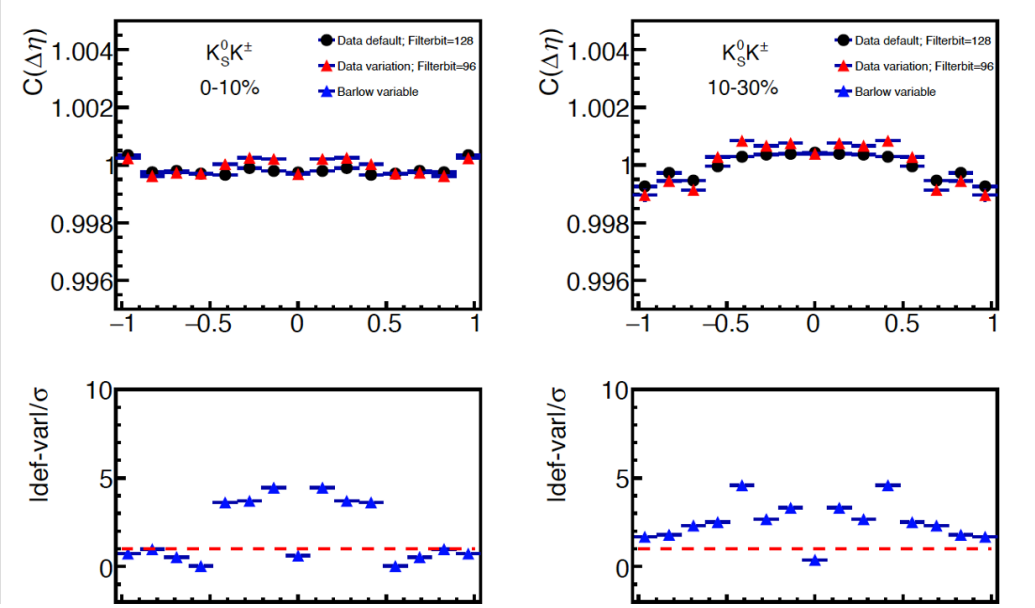

Figure 3.21: Barlow's test result for $\Delta\eta$ projection of $K^0_S K^\pm$ in 0-10% and 10-30% centrality intervals where the Barlow variable is plotted in the bottom panel.

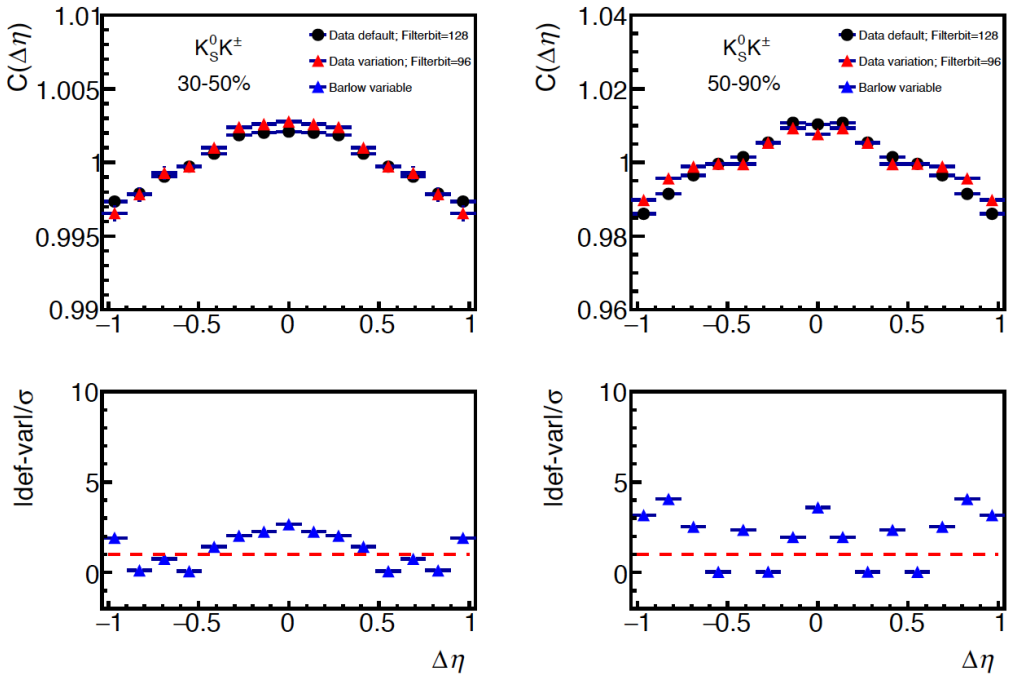

Figure 3.22: Barlow's test result for $\Delta\eta$ projection of $K^0_S K^\pm$ in 30-50% and 50-90% centrality intervals where the Barlow variable is plotted in the bottom panel.

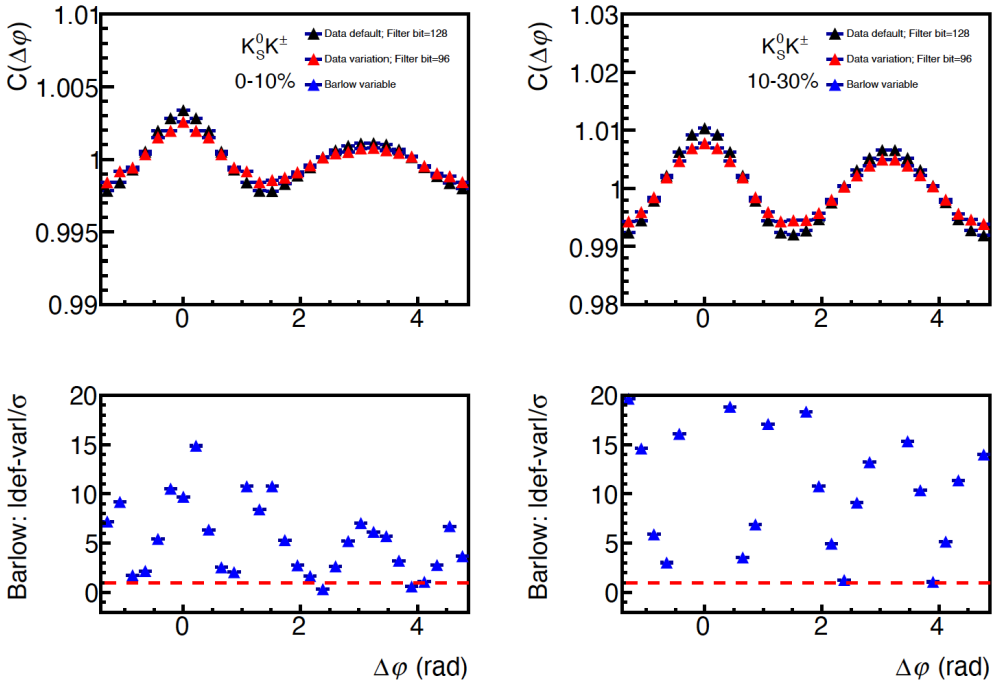

Figure 3.23: Barlow's test result for $\Delta\varphi$ projection of $K^0_S K^\pm$ in 0-10% and 10-30% centrality intervals where the Barlow variable is plotted in the bottom panel.

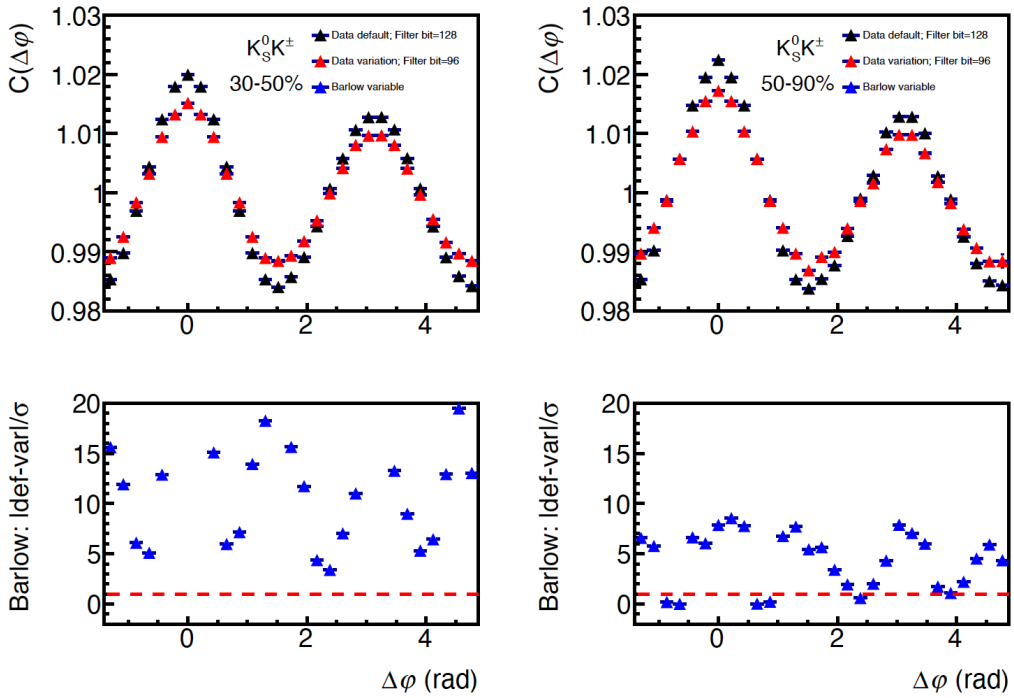

Figure 3.24: Barlow's test result for $\Delta\varphi$ projection of $K^0_S K^\pm$ in 30-50% and 50-90% centrality intervals where the Barlow variable is plotted in the bottom panel.

3.6.5 Total Relative Systematic Uncertainty

Once the individual systematic uncertainties from each source of variation are calculated, the sum of the squares of these values is computed to estimate the total systematic uncertainty. The total systematic uncertainty is represented by the square root of this sum.

$$\text{Total relative systematic uncertainty} = \sqrt{\sum_{i=1}^{n} Syst.Err_i^2} \tag{3.17}$$

In the equation above, $Syst.Err_i$ represents the uncertainty contribution from individual source of error. The total relative systematic uncertainty calculated is applied to $\Delta\varphi$ and $\Delta\eta$ projections of both $\mathrm{K}^0_S\mathrm{K}^{\pm}$ and $\mathrm{K}^+\mathrm{K}^-$ correlation functions. This is shown by grey filled markers in Fig. 4.13, Fig. 4.14, Fig. 4.15, and Fig. 4.16 given in next chapter.

Chapter 4

Analysis Results of $\mathbf{K^0_S K^{\pm}}$ and $\mathbf{K^+K^-}$ Angular Correlations

In this chapter, we discuss the 2D and 1D angular correlation functions of $K^0_S K^{\pm}$ and K^+K^- using HIJING and AMPT MC simulations, anchored to the Run2 Pb–Pb collision data at $\sqrt{s_{NN}} = 5.02$ TeV at the generated level. Subsequently the discussion is extended to include the analysis results using the real Pb–Pb collision data at the same collision energy. The 2D correlations have been corrected for detector efficiencies and secondary contamination. The 1D correlations include correction due to detector efficiencies and secondary contamination, and the total systematic error estimation. The 1D projections of these correlations are taken in both $\Delta\varphi$ and $\Delta\eta$ directions and are compared with the theoretical model predictions. These models do not account for the physics contributions from condensate formation, thus providing a baseline for the analysis.

4.1 2D Correlations using Models

4.1.1 HIJING Model Predictions

The Fig.4.1 displays the 2D $K^0_S K^{\pm}$ angular correlation function using the HIJING model at generated level for 0–10%, 10–30% and 30–60% centrality intervals. As discussed previously, the final 2D angular correlations contain an interplay of various physics mechanisms. The correlation structures observed in the near side region are more prominent in the higher centrality interval due to the dilution effects. To explore the contribution of secondary kaons in this correlation, we remove all the kaons except the primarily produced kaons in the simulation. The correlations after removing all the particle pairs coming from weak and strong resonance decays for 0–10%, 10–30% and 30–60% centrality intervals are displayed in Fig.4.2. It is observed that the correlations are mostly flat in the near side after the resonance subtraction, except some remnant contributions which may be coming from mini-jets.

Similar study is done using K^+K^- particle pairs and the Fig. 4.3 illustrates the corresponding 2D correlation function using the HIJING model simulation at the generated level anchored to the Pb–Pb collision data at $\sqrt{s_{\rm NN}} = 5.02$ TeV for 0–10%, 10–30% and 30–60% centrality intervals. We can see a strong peak in the near side region whereas it is mostly flat in the away side. From the discussion in Section. 1.6, we expect to see a significant contribution to the near side peak originating from $\Phi(1020)$ meson resonance. Indeed, there is a pronounced peak on the near side of Fig. 4.3 in all centrality intervals. This is further supported by the Fig. 4.4, which displays the K^+K^- correlation after subtracting all the resonance contribution and shows that the major peak is no longer present. This was also confirmed by removing only the Φ meson resonances based on its PDG code.

Additionally, in both $K^0_S K^{\pm}$ and K^+K^- correlations, we observe no signs of contribution from collective expansion, which is consistent with expectations. The HIJING model does

not account for the evolution of the system, including flow dynamics. To explore the physics involving flow effects, we need to employ a different model. AMPT is suitable for this purpose and will be the focus of the next section.

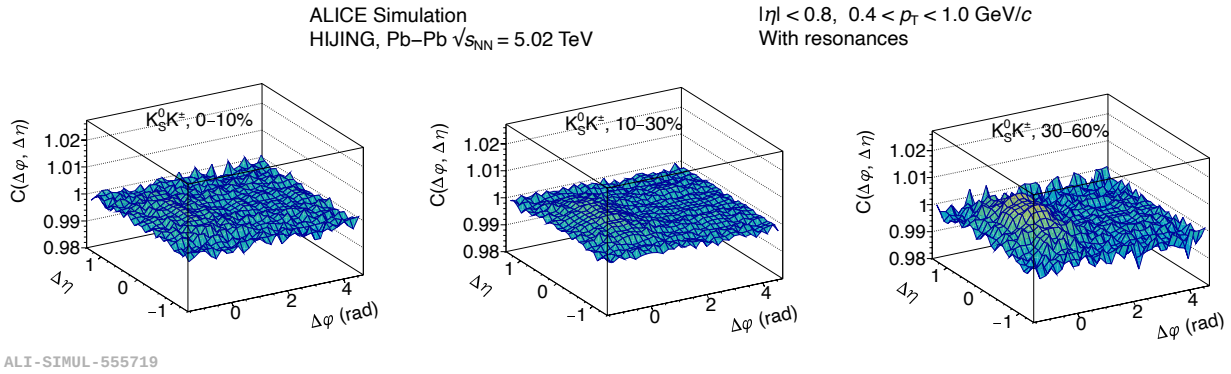

Figure 4.1: 2D $K^0_S K^{\pm}$ correlation function using the HIJING model production at generated level at $\sqrt{s_{\rm NN}} = 5.02$ TeV with the default cuts for 0–10%, 10–30% and 30–60% centrality intervals are displayed.

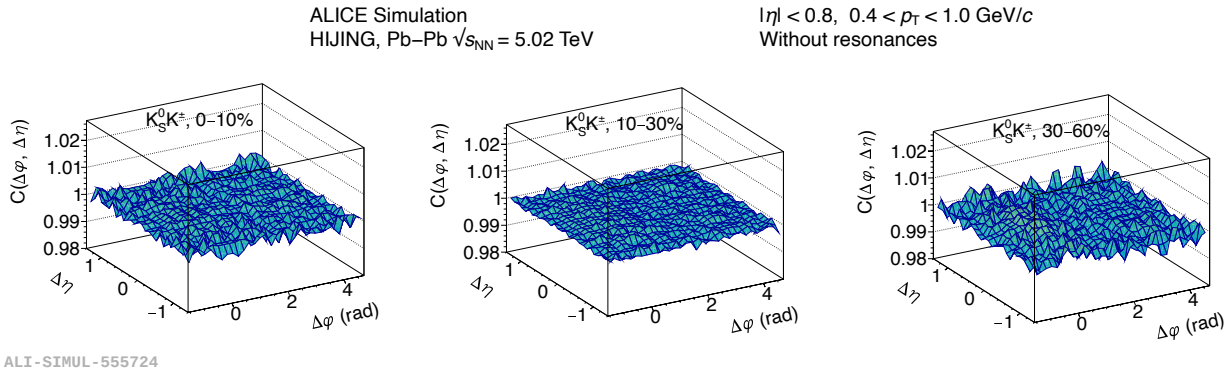

Figure 4.2: 2D $K^0_S K^{\pm}$ correlation function after removing all the resonance decay contributions using the HIJING model production at generated level at $\sqrt{s_{\rm NN}} = 5.02$ TeV with the default cuts for 0–10%, 10–30% and 30–60% centrality intervals are displayed

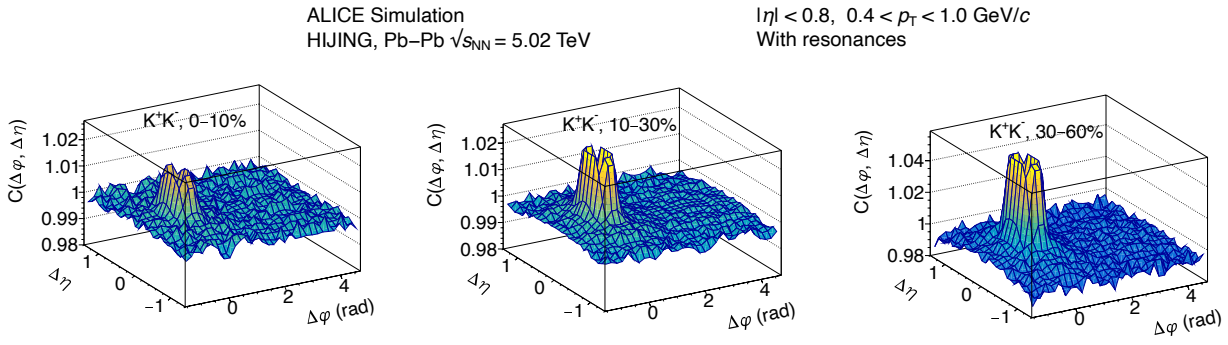

Figure 4.3: 2D K^+K^- correlation function using the HIJING model production at generated level at $\sqrt{s_{NN}} = 5.02$ TeV with the default cuts for 0–10%, 10–30% and 30–60% centrality intervals are displayed.

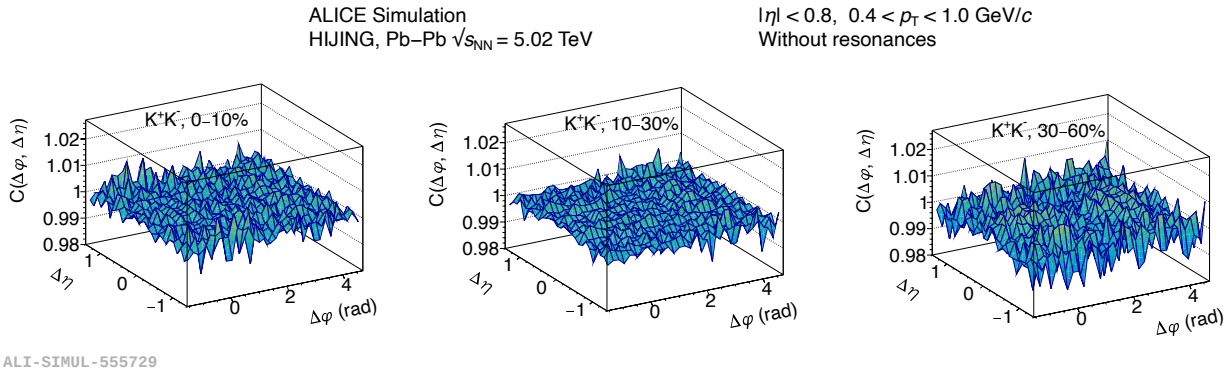

Figure 4.4: 2D K^+K^- correlation function after removing all the resonance decay contributions using the HIJING model production at generated level at $\sqrt{s_{NN}} = 5.02$ TeV with the default cuts for 0–10%, 10–30% and 30–60% centrality intervals are displayed

4.1.2 AMPT Model Predictions

The Fig. 4.5 displays the 2D $K^0_S K^{\pm}$ correlation for 0–10%, 10–30% and 30–60% centrality intervals. A notable observation from this figure is transformation of the near-side region of the correlation compared to HIJING, which no longer appears flat; instead, a distinct flow profile is evident. Disentangling contribution from different physics effects require further studies.

Similarly, the 2D correlation functions of K^+K^- using the same dataset at the generated level for 0–10%, 10–30% and 30–60% centrality intervals are illustrated in Fig. 4.6. The observed final shape of the correlation is influenced by a combination of flow effects and the near-side peak, primarily attributed to resonances. This suggests that while flow dynamics play a significant role in shaping the correlation pattern, resonances also make a substantial contribution, particularly in enhancing the near-side peak. In both $K^0_S K^{\pm}$ and K^+K^- correlations, jets may also contribute to the near side peak, but this aspect has not been investigated at this time.

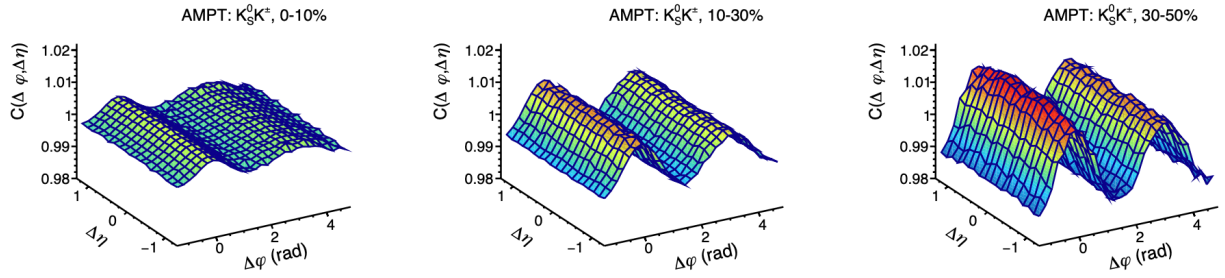

Figure 4.5: 2D $K^0_S K^{\pm}$ correlation function using the AMPT model anchored production at generated level at $\sqrt{s_{\rm NN}} = 5.02$ TeV with the default cuts for 0–10%, 10–30% and 30–60% centrality intervals are displayed.

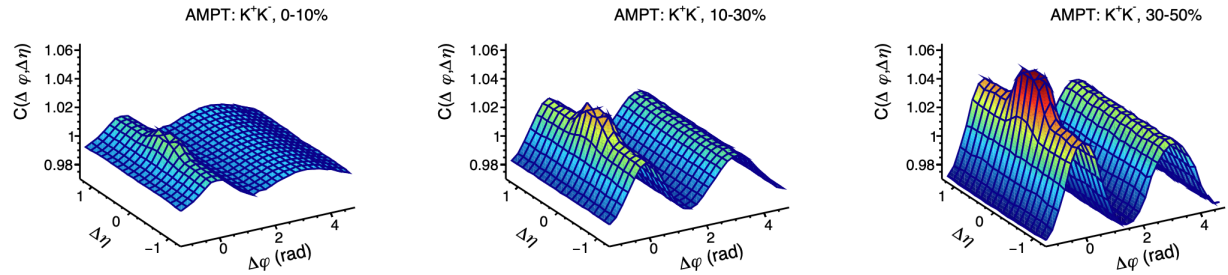

Figure 4.6: 2D K^+K^- correlation function using the AMPT model anchored production at generated level at $\sqrt{s_{\rm NN}} = 5.02$ TeV with the default cuts for 0–10%, 10–30% and 30–60% centrality intervals are displayed.

4.1.3 HIJING With and Without Resonances

The following figures compare the HIJING model predictions for both $K^0_S K^{\pm}$ and K^+K^- correlation functions before and after subtracting the contributions from weak and strong

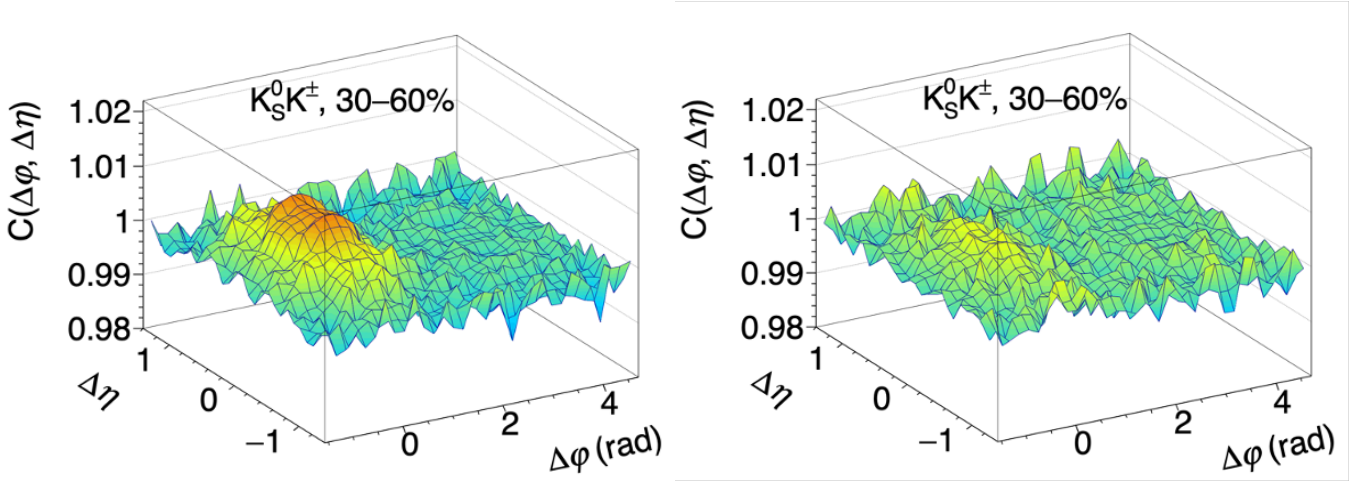

(a) (b)

Figure 4.7: 2D $K^0_S K^{\pm}$ correlation function using HIJING model (a) before and (b) after the resonance subtraction using Pb–Pb collision data $\sqrt{s_{\rm NN}}$ = 5.02 TeV for 30–60% centrality interval is displayed.

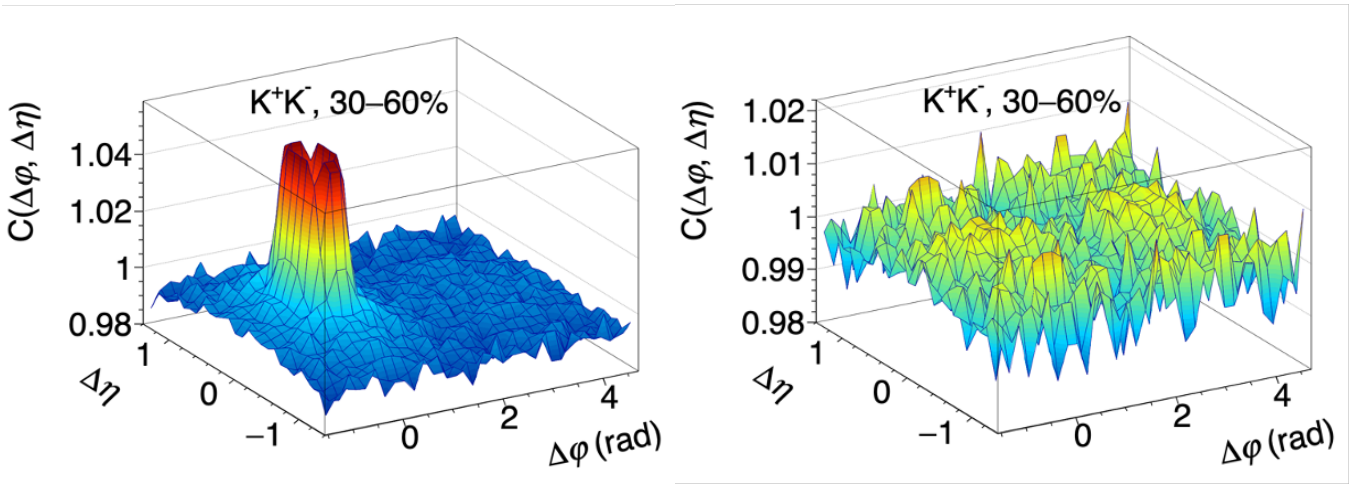

(a) (b)

Figure 4.8: 2D K^+K^- correlation correlation function using HIJING model (a) before and (b) after the resonance subtraction using Pb–Pb collision data $\sqrt{s_{\rm NN}}$ = 5.02 TeV for 30–60% centrality interval is displayed.

4.1.4 HIJING Vs AMPT Comparison

The following figures compare the HIJING and AMPT model predictions for both $K^0_S K^{\pm}$ and K^+K^- correlation functions. Notably, the HIJING model lacks flow effects, whereas the AMPT model incorporates them, allowing for a distinct visualization of both flow and non-flow features within the models.

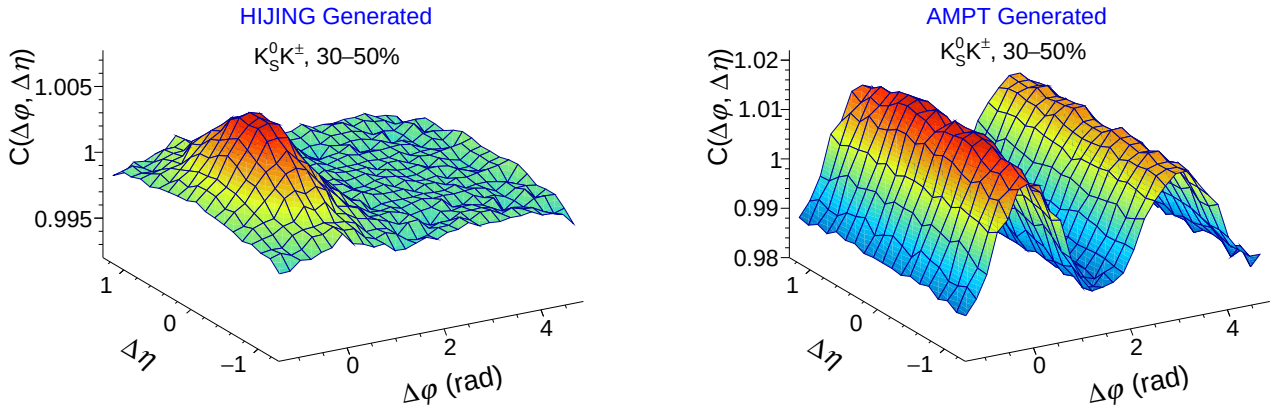

(a) (b)

Figure 4.9: 2D $K^0_S K^{\pm}$ correlation function using (a) HIJING model and (b) AMPT model at generated level at $\sqrt{s_{\rm NN}} = 5.02$ TeV for 30–50% centrality interval is displayed.

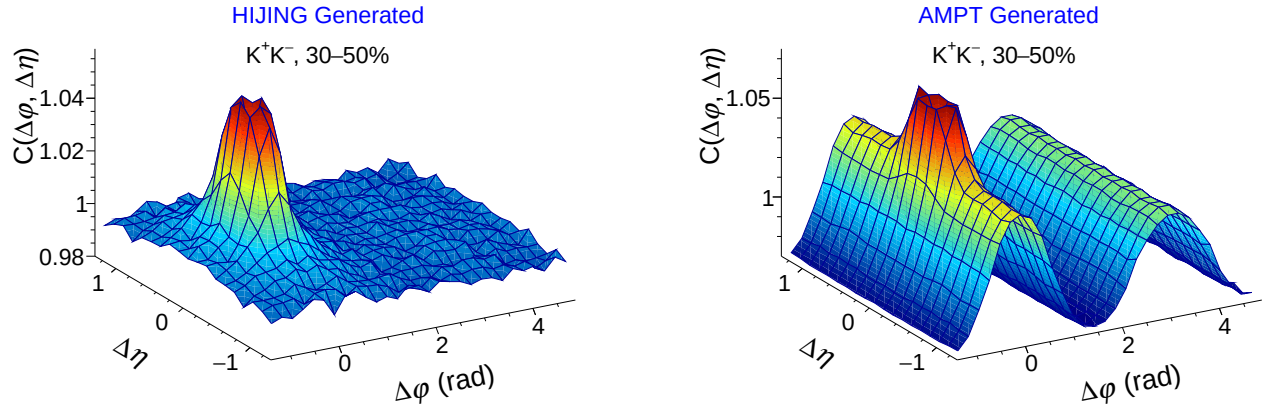

(a) (b)

Figure 4.10: 2D K^+K^- correlation function using (a) HIJING model and (b) AMPT model at generated level at $\sqrt{s_{\rm NN}} = 5.02$ TeV for 30–50% centrality interval is displayed

4.2 2D Correlations using Data

In this section, the final 2D correlation functions of $K^0_S K^{\pm}$ (Fig. 4.11) and K^+K^- (Fig. 4.12) corrected for detector efficiencies and secondary contamination using Pb–Pb collision data at $\sqrt{s_{\rm NN}} = 5.02$ TeV are discussed. The correlations are computed in 0–10%, 10–30%, 30–50% and 50–90% centrality intervals. The MB trigger is set for all centralities except for the case of 0–10% centrality where the dedicated kCentral trigger is utilized for better statistics. As seen in model predictions, both the correlations show dependence on multiplicity. From most central to peripheral collisions, the strength of the correlations is increasing due to the known dilution effect. This is expected because in peripheral collisions, there are less produced particles in the correlated events and the background is small and therefore the correlation strength is stronger. It is observed that collective flow has a dominant effect in both the correlations as one would expect in case of heavy ion collisions.

In Fig. 4.11, we observe a depression in the near-side region of the correlation function in the 0–10% centrality. This dip is not observed in the 10–30% and 30–50% centrality intervals where the correlations show features similar to those predicted by the AMPT model. The correlations in the near side region are growing with centrality and in the 50–90% centrality, the peak is sharper. In these peripheral collisions, additional physics mechanisms may be influencing significant changes in the shape of the correlation. In Fig. 4.12, the overall shape of the correlation remains consistent across all the centrality intervals although the magnitude of the correlation demonstrates centrality/multiplicity dependence, as expected. The specific features of the correlation are similar to those predicted by the AMPT model. Notably, a near-side peak is evident, superimposed on the collective flow profile. This near-side peak at $(\Delta\eta, \Delta\varphi) \approx (0,0)$ observed in K^+K^- correlation is a combination of at least two physics effects: (i) fragmentation of hard-scattered partons (minijets) and (ii) resonance decays. Obtaining magnitude and impact of these individual contributions to the final correlation

function require a more detailed analysis. Preliminary results regarding flow and resonance subtraction from these correlation functions are discussed in Chapter 6. Observing these correlations visually, no anomalous behavior is apparent. Furthermore, 1D projections have been taken to facilitate comparisons with model predictions, and are discussed in the next two sections of this chapter.

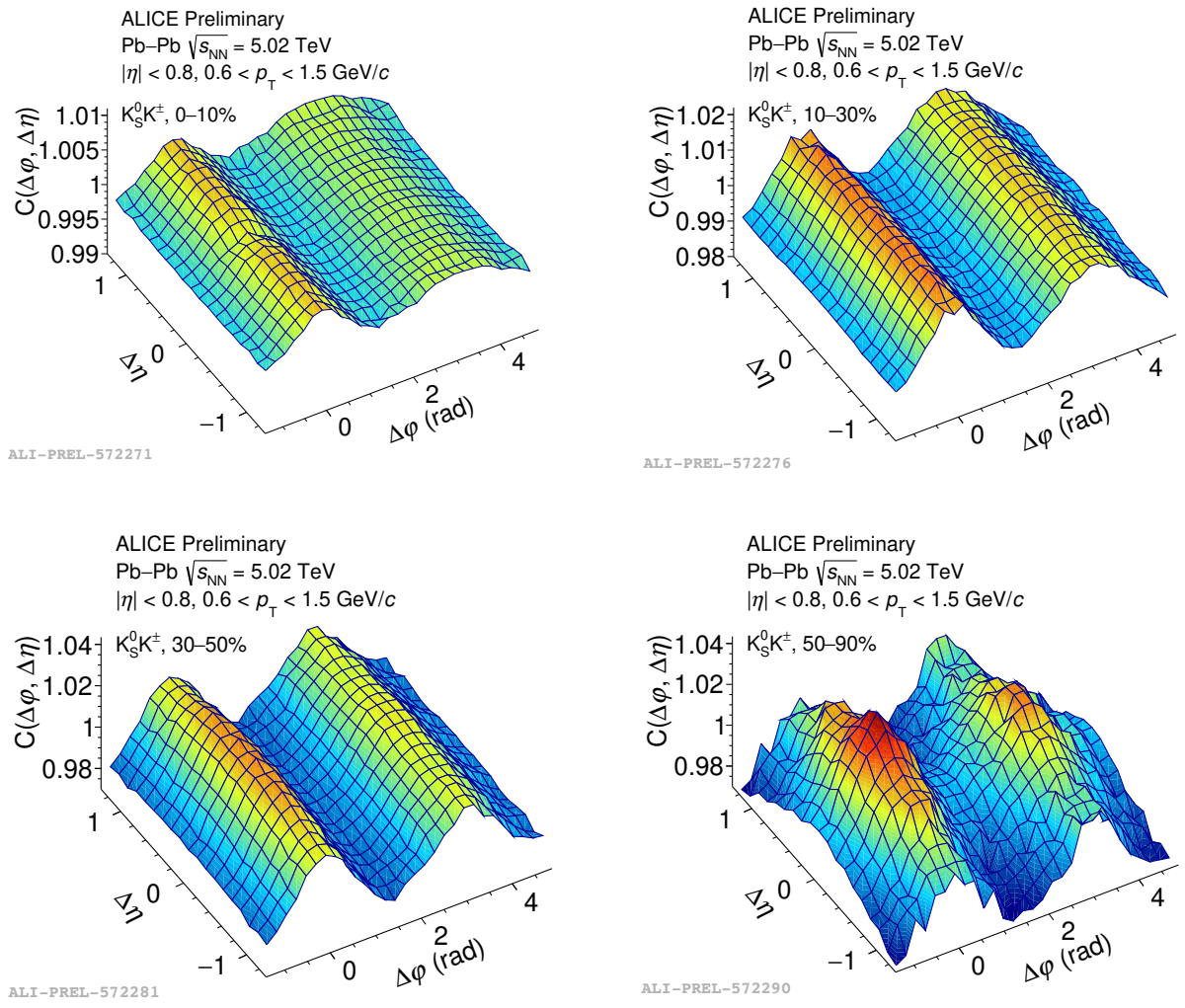

Figure 4.11: The final $K^0_S K^{\pm}$ correlation function corrected for detector efficiencies and secondary contamination using the Pb–Pb collision data at $\sqrt{s_{\rm NN}}$ = 5.02 TeV for 0–10%, 10–30%, 30–50% and 50–90% centrality intervals are displayed.

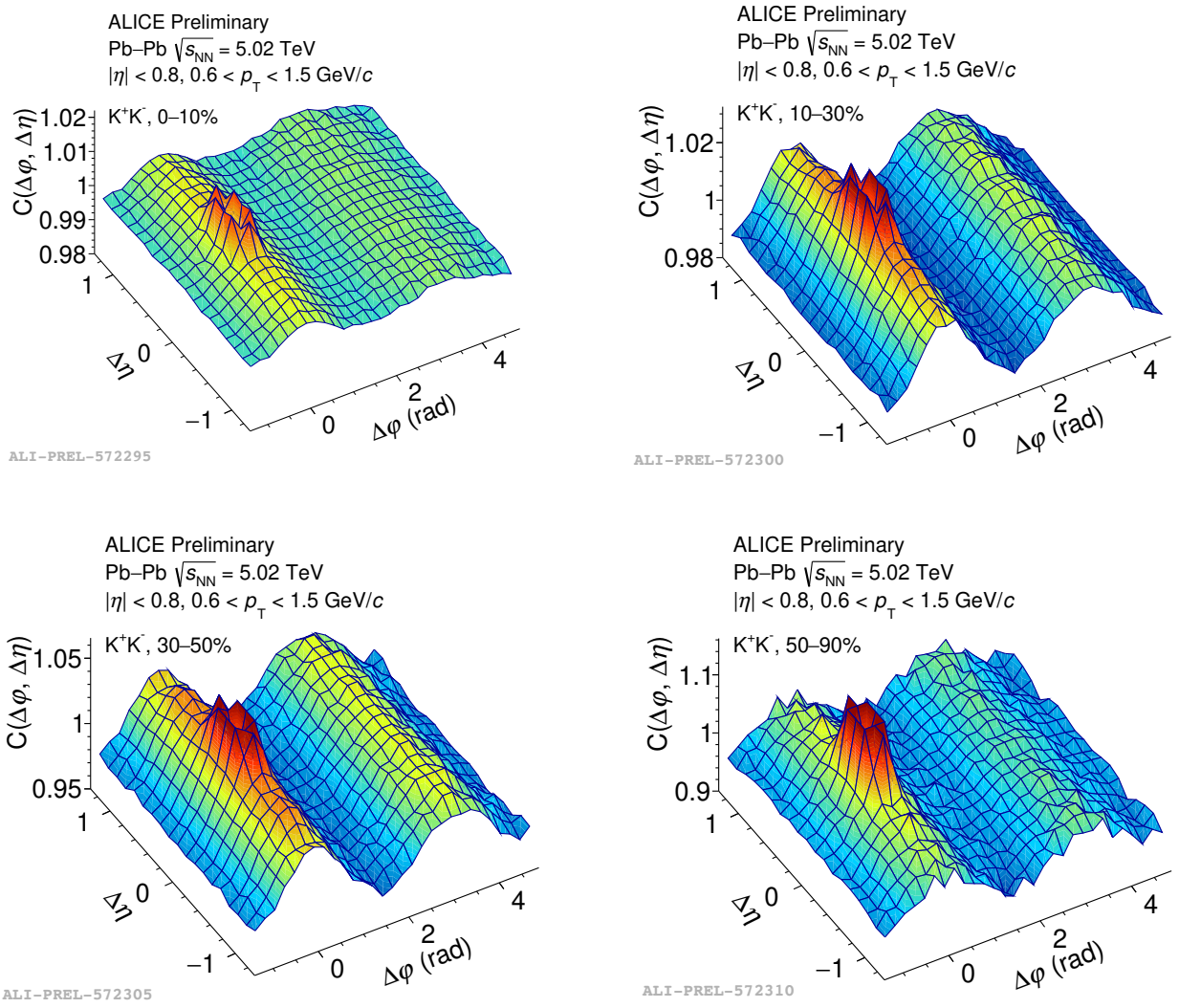

Figure 4.12: The final K^+K^- correlation function corrected for detector efficiencies and secondary contamination using the Pb–Pb collision data at $\sqrt{s_{NN}} = 5.02$ TeV for 0–10%, 10–30%, 30–50% and 50–90% centrality intervals are displayed.

4.3 1D Projections of $K^0_S K^\pm$ Correlation Function

4.3.1 $\Delta\eta$ Projections

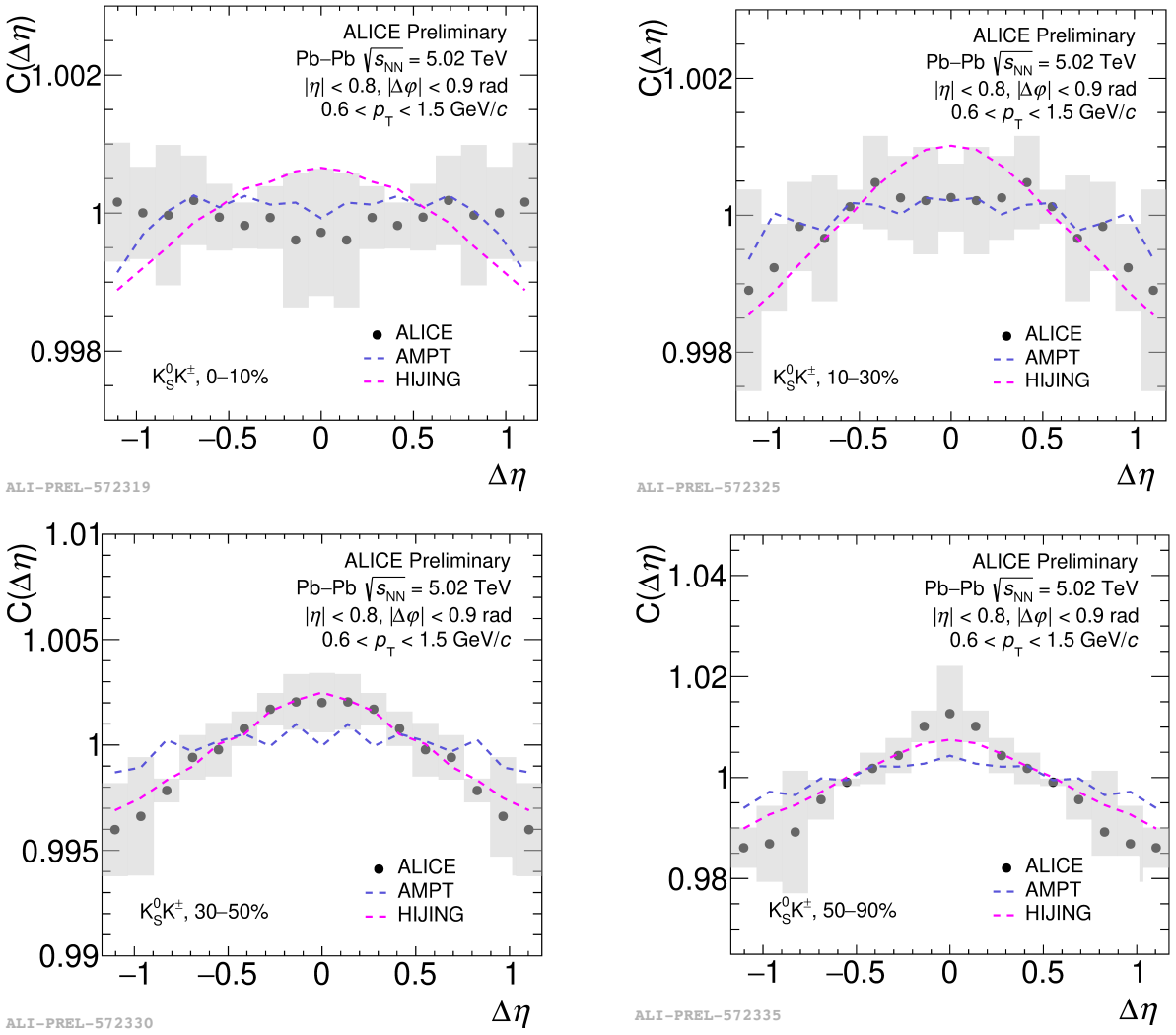

Figure 4.13: The $\Delta\eta$ projections of $K^0_S K^\pm$ using the Pb–Pb collision data at $\sqrt{s_{NN}} = 5.02$ TeV in centrality interval of 0-10% is shown.

4.3.2 $\Delta\varphi$ Projections

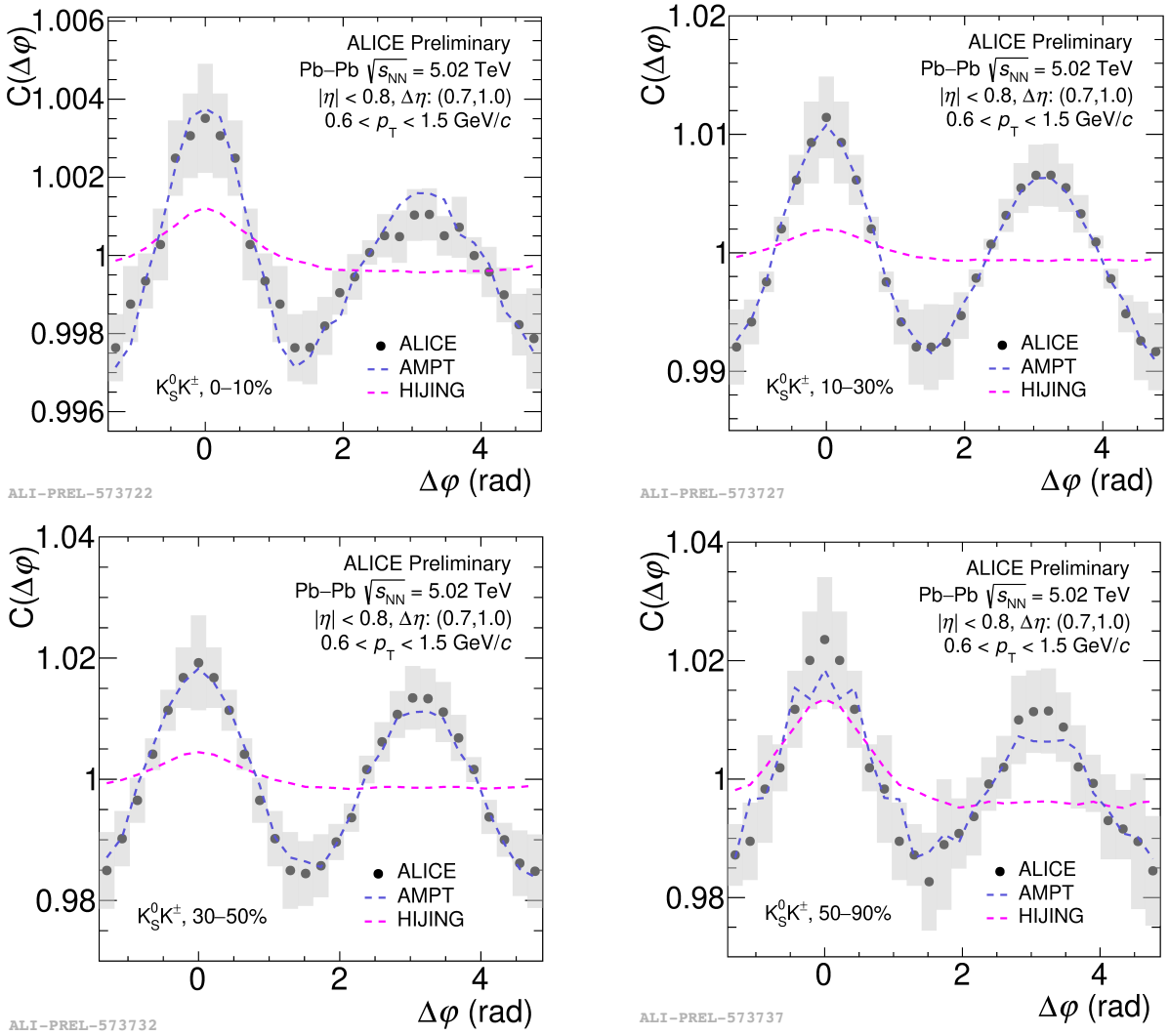

Figure 4.14: The $\Delta\varphi$ projections taken in the nearside for $K^0_S K^\pm$ is compared to that of $K^+_S K^-$ in 0-10%, 10-30%, 30-50% and (b) 50-90% centrality intervals using the Pb–Pb collision data at $\sqrt{s_{NN}} = 5.02$ TeV.

The $\Delta\eta$ and $\Delta\varphi$ projections of $K^0_S K^{\pm}$ correlation function measured using Pb–Pb collision data at $\sqrt{s_{\rm NN}} = 5.02$ TeV in 0–10%, 10–30%, 30–50% and (b) 50–90% centrality intervals are shown in Fig. 4.13 and Fig. 4.14 respectively. The correlations for each centrality interval are compared with predictions from the HIJING and AMPT models. The data points are represented by black markers, while the grey regions indicate the associated systematic errors. The predictions from the HIJING and AMPT models are depicted as pink and blue dashed lines, respectively. In $\Delta\eta$ projections shown in Fig. 4.13, it is observed that the HIJING and AMPT models describe the data within the systematic error for all the centrality intervals. A careful investigation shows that there is a slight centrality dependence in the data, characterized by the disappearance of the nearside peak in the 0–10% centrality interval, where the models tend to overestimate the data. As centrality increases, the alignment between the data and model predictions improves. Notably, the experimental data and HIJING model predictions are in complete agreement at the 30-50% centrality interval. However, in higher centralities of 50–90%, the model predictions tend to underestimate the data. This vanishing near-side peak could be attributed to the presence of anti-correlation structures, which, when combined with near-side correlations, result in weaker overall correlations. The presence of such anti-correlation features could have indicated condensate signals, supporting the $_{dyn}$ analysis. However, the presence of large systematic errors makes these interpretations not conclusive.

In $\Delta\varphi$ projections shown in Fig. 4.14, the AMPT model is able to reproduce the behavior in the experimental data for all the centrality intervals. The HIJING model predictions are included for completeness though we do not expect HIJING to describe the flow correlations as the model does not include the description of collective expansion. Therefore, the observed disagreement between the HIJING model and experimental data is expected. Additionally, ALICE has previously measured the elliptic flow or v_2 as a function of p_T for $K^{\pm}$ and its description using AMPT model are documented in [105]. While discrepancies between

the HIJING and AMPT models in the $\Delta\varphi$ direction are anticipated, differences in the $\Delta\eta$ direction are not as straightforward. Notably, in Fig. 4.13, we observe a 1% discrepancy between these models in central collisions (0–10% and 10–30% centrality intervals). This variation can be attributed to AMPT's inclusion of radial expansion, which offers a more accurate description in central collisions, where radial flow (azimuthally symmetric) is the only possible form of transverse flow. In non-central or peripheral collisions, the azimuthal symmetry is broken, and anisotropic flow patterns can arise due to anisotropic initial overlap region. The $\Delta\varphi$ projections are affected by anisotropic flow patterns and $\Delta\eta$ projections are affected by radial flow patterns. In conclusion, AMPT which includes radial expansion describes the trends observed in $\Delta\eta$ projections across all centrality intervals, while HIJING tends to slightly underestimates them in central collisions. Similarly, the $\Delta\varphi$ projections are well described by AMPT but not by HIJING.

4.4 Comparison of $K^0_S K^{\pm}$ and K^+K^- Correlation Functions

4.4.1 $\Delta\eta$ Projections

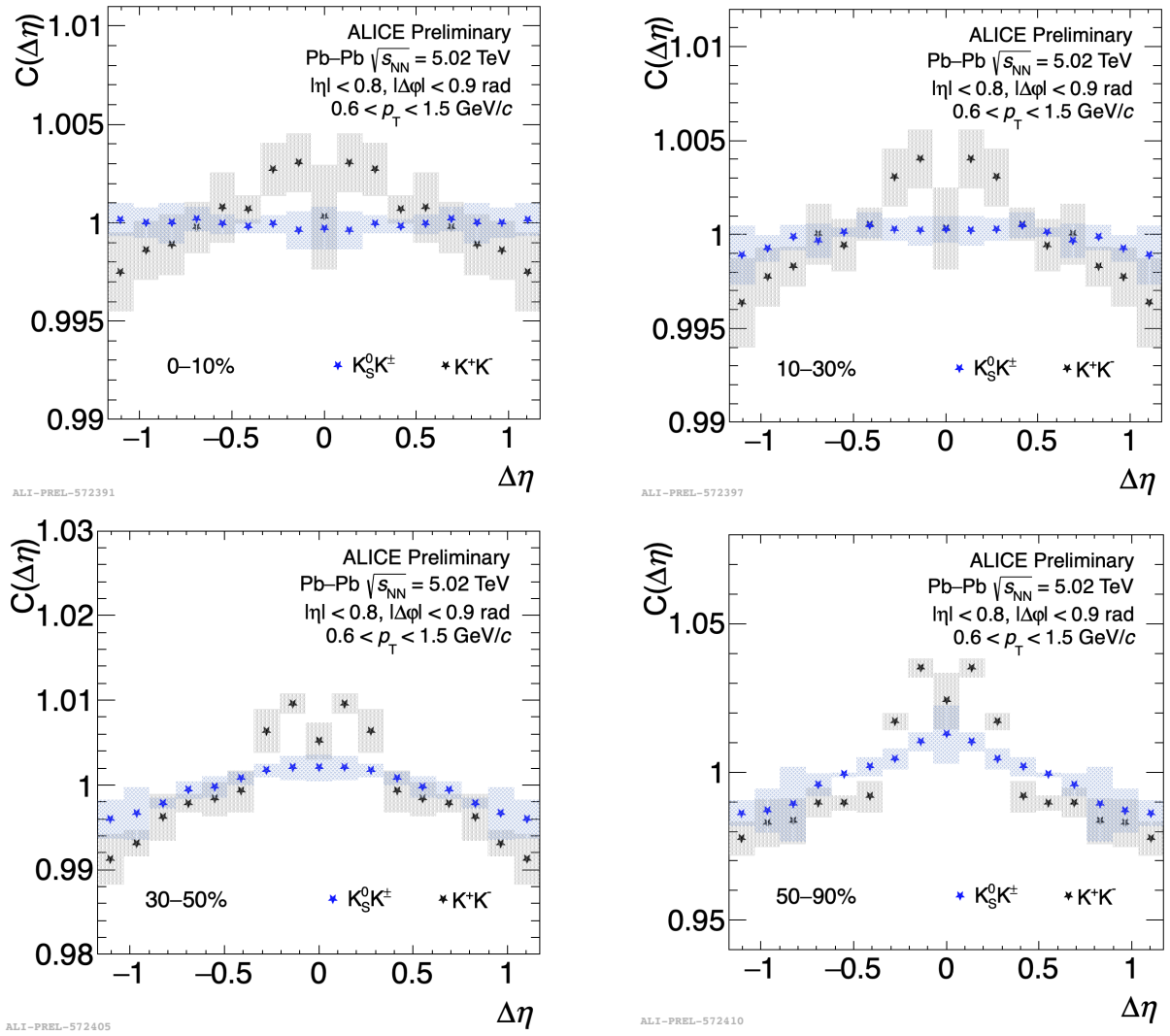

Figure 4.15: The $\Delta\eta$ projections taken in the nearside for $K^0_S K^{\pm}$ is compared to that of K^+K^- in 0-10%, 10-30%, 30-50% and (b) 50-90% centrality intervals using the Pb–Pb collision data at $\sqrt{s_{\rm NN}} = 5.02$ TeV. The blue and black bars represent the systematic errors associated with the $K^0_S K^{\pm}$ and K^+K^- correlations.

4.4.2 $\Delta\varphi$ Projections

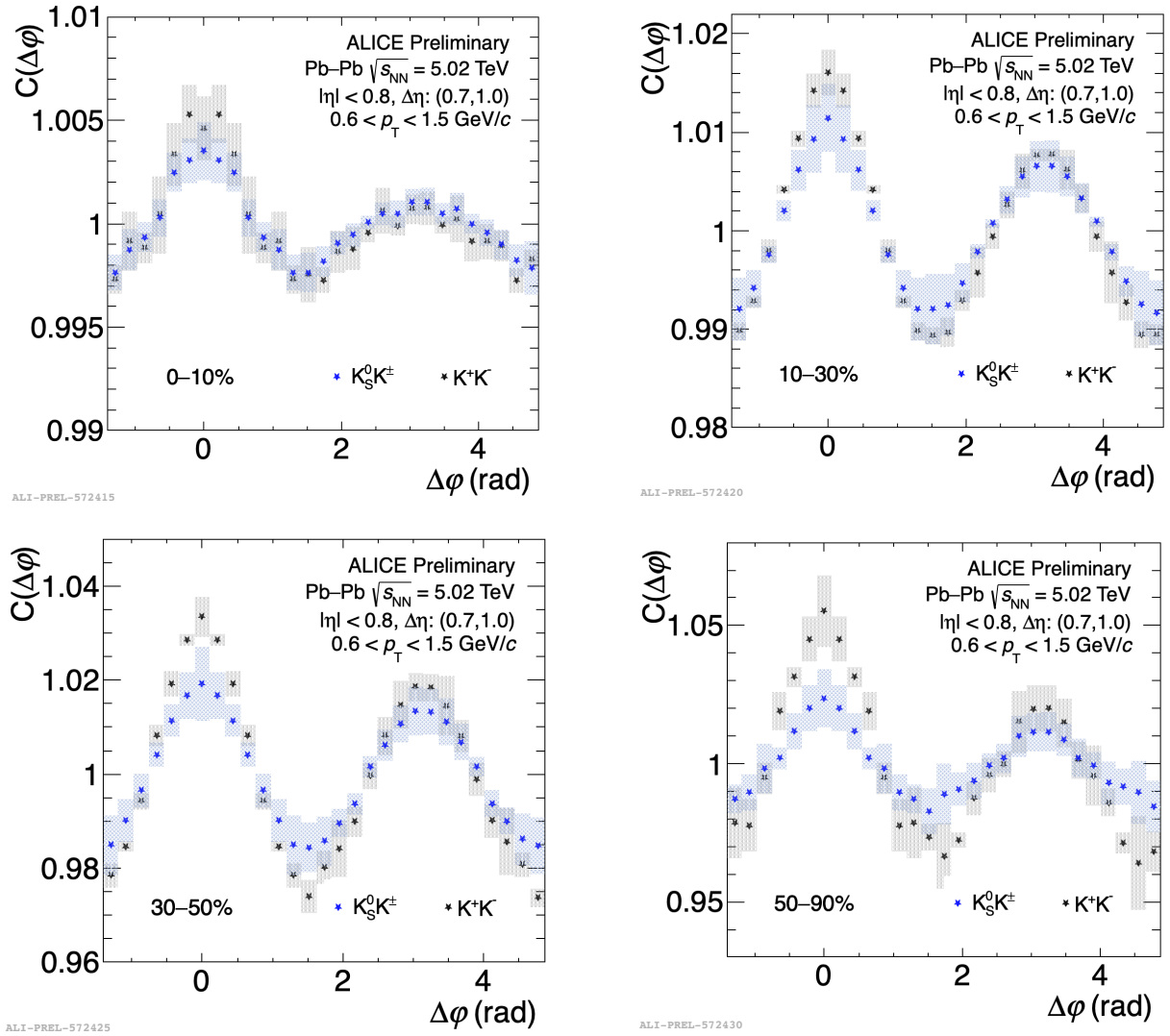

Figure 4.16: The $\Delta\varphi$ projections taken in $\Delta\eta$ interval of (0.7, 1.0) for $K^0_S K^\pm$ is compared to that of K^+K^- in 0-10%, 10-30%, 30-50% and (b) 50-90% centrality intervals using the Pb–Pb collision data at $\sqrt{s_{NN}} = 5.02$ TeV. The blue and black bars represent the systematic errors associated with the $K^0_S K^\pm$ and K^+K^- correlations.

The $\Delta\eta$ and $\Delta\varphi$ projections of $K^0_S K^{\pm}$ correlation function compared with that of K^+K^- in 0–10%, 10–30%, 30–50% and 50–90% centrality intervals are shown in Fig 4.15 and Fig 4.16 respectively. The blue markers represent the $K^0_S K^{\pm}$ correlations and the black markers represent the K^+K^- correlations with associated systematic errors. The $\Delta\eta$ projections are taken in a $\Delta\varphi$ range of (-0.9, 0.9) radian and $\Delta\varphi$ projections are taken in high $\Delta\eta$ range of (0.7, 1.0). In $\Delta\eta$ projections shown in Fig. 4.15, we observe that the $K^0_S K^{\pm}$ correlation values are rather flat compared to that of K^+K^-. The discrepancy between these two correlations can be attributed to the dominant contribution from $\Phi(1020)$ meson resonance to the final $K^+_S K^-$ correlation function. The correlations seem to have similar features across all the centrality intervals.

In $\Delta\varphi$ projections shown in Fig. 4.16, the flow profile of $K^0_S K^{\pm}$ and K^+K^- are in agreement within the systematic error for central collisions (0–10% centrality). From central to peripheral collisions, the discrepancy between the correlations seems to increase and it is maximum for the nearside region in 50–90% centrality interval. The ALICE collaboration measured elliptic flow coefficient (v_2) of identified particles in Pb–Pb collisions at $\sqrt{s_{NN}} = 2.76$ TeV and the values are reported in [49]. Although we can not directly compare the previous findings of (v_2) by ALICE with the flow correlation measurements in this analysis, it is interesting to observe the features they exhibit. The results in [49] were obtained with the scalar product method, a two-particle correlation technique, using a pseudo-rapidity gap of $\Delta\eta > 0.9$ between the identified hadron under study and the reference particles. The v_2 values are reported for K^0_S and $K^{\pm}$ as a function of p_T for different centralities. A centrality and p_T dependent difference is observed for these two measurements where v_2 for neutral kaons is systematically lower than that of their charged counterparts. The difference between the two measurements reaches up to two standard deviations in central collisions and is of one standard deviation in peripheral Pb–Pb collisions. In our measurement, most agreement between $K^0_S K^{\pm}$ and K^+K^- flow profiles were seen in central collisions which is contrasting to

the ALICE result. An explanation for the origin of the differences in v_2 of K^0_S and $K^{\pm}$ and exploring the direct relation between ALICE measurement and this analysis requires further investigation.

Overall, the angular correlations of $\mathrm{K}^0_S\mathrm{K}^{\pm}$ and $\mathrm{K}^+\mathrm{K}^-$ are described by MC model simulations. We do not observe significant anti-correlation structures in the $\mathrm{K}^0_S\mathrm{K}^{\pm}$ correlation and as a result, these angular correlations do not exhibit anomalous behavior in the production of neutral and charged kaons, a finding in contrast to the ν_{dyn} measurement. To further validate these conclusions, it is important to subtract the individual contributions of various physics mechanisms. If we are left with a correlation function that is approximately flat around unity, this would indicate that all significant contributions have been accounted for.

Chapter 5

Summary

This dissertation focused on the measurement of two particle angular correlation functions of pairs of neutral and charged kaons ($K^0_S K^{\pm}$) and oppositely charged kaons (K^+K^-) using experimental Pb–Pb collision data at $\sqrt{s_{NN}} = 5.02$ TeV (Run2 data collected in 2018). The correlations are calculated as a function of $\Delta\eta$ and $\Delta\varphi$, where $\Delta\eta$ is the difference in the pseudo-rapidities and $\Delta\varphi$ is the difference in azimuthal angles of particle pairs respectively. This marks the first time the ALICE experiment has measured $K^0_S K^{\pm}$ angular correlation functions.

The motivation for this analysis stems from a previous ALICE Collaboration publication that reported ν_{dyn} as a function of centrality for neutral to charged kaon pairs ($\nu_{\rm dyn}[K^0_S, K^{\pm}]$) and oppositely charged kaon pairs ($\nu_{\rm dyn}[K^+, K^-]$) using experimental Pb–Pb collision data at $\sqrt{s_{\rm NN}} = 2.76$ TeV (Run1 data collected in 2010). The ν_{dyn} is a statistical fluctuation observable proposed to study isospin fluctuations in the strangeness sector. The experimental values are compared with Monte–Carlo simulations including HIJING, three modes of AMPT and EPOS–LHC. The measured values of $\nu_{\rm dyn}[K^0_S, K^{\pm}]$ exhibited large deviation from the model predictions and showed three distinct anomalies which are 1) the dynamical correlations are unusually large, 2) ν_{dyn} scaled by multiplicity shows a clear centrality/multiplicity

dependence, with the correlations increasing as multiplicity grows, and 3) these correlations stretch over a unit in pseudorapidity. Furthermore, $\nu_{\rm dyn}[K^+, K^-]$ does not show anomalous behavior and the magnitude and shape of experimental values are well reproduced by Monte–Carlo model predictions. These correlations can only be explained by invoking the formation of condensates in heavy ion collisions that can decay into hadrons and therefore cause fluctuations in the number of produced neutral and charged kaons. Two such theoretically hypothesized phenomena are Disoriented Chiral Condensate (DCC) and Disoriented Isospin Condensate (DIC). DCC involves disorientation and emission from kaon fields i.e., in the strange quark sector while DIC involve disorientation in the light quark sector.

To further explore this anomalous behavior, we performed a differential analysis of these correlations in $\Delta\eta\Delta\varphi$ space. The measurement was carried out in different centrality classes, including 0–10%, 10–30%, 30–50% and 50–90%. The primary task in the analysis is to perform the particle identification (PID) for neutral and charged kaons. The neutral and charged kaon tracks were selected in a kinematic range of transverse momentum cut: $0.6 < p_T < 1.5$ GeV/c and pseudo-rapidity cut: $-0.8 < \eta < 0.8$. The combined information from Time Projection Chamber and Time Of Flight detectors were used to identify the charged kaons, based on the nσ PID technique. The neutral kaons are reconstructed based on the weak decay $K^0_S \rightarrow \pi^+ + \pi^-$. These decays are identified from the decay topology of V0 particle having a characteristic shape. Both kinematic and topological selection criteria are utilized to select a pure sample of K^0_S candidates. The K^0_S selection does involve nearly 20% contamination as seen in the invariant mass distribution and is accounted for in the systematic error estimation. To verify the track and topological selection criteria used for PID, Monte–Carlo (MC) closure test was performed and the successful results were obtained. The correlations are measured both at the MC generated and MC reconstructed level and are compared to each other. The closure test was done using the HIJING model production anchored to Pb–Pb collision data at $\sqrt{s_{NN}} = 5.02$ TeV. The total detector efficiency (sum

of tracking efficiency and PID efficiency), purity and secondary contamination of $K^{\pm}$ and K^0_S were also calculated using the HIJING data. The yield of $K^{\pm}$ and K^0_S for the correlation function was corrected for detector efficiencies and secondary contamination. These final correction factors are supplemented to the particle pairs bin by bin while calculating the correlation function. The final correlation function, $C(\Delta\varphi, \Delta\eta)$ is calculated as a ratio of signal ($S(\Delta\varphi, \Delta\eta)$) and background ($B(\Delta\varphi, \Delta\eta)$) where the signal distribution is constructed using the particle pairs from the same events which are correlated and the background is the reference distribution created using particle pairs from different events that are uncorrelated and therefore reflecting the single particle acceptance effects. The background is calculated using the event mixing procedure where each event is mixed with 10 events that are similar in terms of multiplicity and primary vertex position.

The 2D angular correlations of ($K^0_S K^{\pm}$) and (K^+K^-) correlations are computed. To understand the magnitude and extend of physics contributions to this correlation, 1D projections are computed in both $\Delta\eta$ and $\Delta\varphi$ directions with a comparison to both AMPT and HIJING predictions at the generated level. In our differential measurement, we expected to see structures due to anti-correlation in case of $K^0_S K^{\pm}$ angular correlation function based on the previous positive values of ν_{dyn}. However the results were indeed surprising. The model predictions using HIJING and AMPT (with string melting) seems to describe the correlations in the experimental data within the systematic error. As HIJING model does not include collective expansion, the correlation in $\Delta\varphi$ shows large discrepancy with the data which is expected. Whereas the AMPT model describes the flow correlations very well. In $\Delta\eta$ correlation, a small anti-correlation dip is observed for ($K^0_S K^{\pm}$) which does have a centrality dependence. The dip is observed in 0-10% centrality and is vanishing for 30-50% centrality. However due to large values of systematic error, these findings are not conclusive.

A comparison of ($K^0_S K^{\pm}$) and (K^+K^-) correlations in both $\Delta\varphi$ and $\Delta\eta$ directions is also done in various centrality intervals. The $\Delta\eta$ projections are taken in a $\Delta\varphi$ range of

(-0.9, 0.9) and $\Delta\varphi$ projections are taken in high $\Delta\eta$ range of (0.7, 1.0). In $\Delta\eta$ projection, it is observed that the $K^0_S K^{\pm}$ correlation values are rather flat compared to that of K^+K^-. The discrepancy between the two correlations can be attributed to the contribution from $\Phi(1020)$ meson resonance to the $K^+_S K^-$ correlation function. The correlations seem to have similar features across all the centrality intervals. In $\Delta\varphi$ projections, the flow profile of $K^0_S K^{\pm}$ and K^+K^- are in agreement within the systematic error for central collisions (0–10% centrality). From central to peripheral collisions, the discrepancy between the correlations seems to increase and it is maximum for the nearside region in 50–90% centrality.

It can be concluded that the angular correlations do not exhibit anomalous behavior in the production of neutral and charged kaons, an observation in contrast to the previous integrated event-by-event ν_{dyn} measurement. AMPT model provides a better description compared to the HIJING and this can be attributed to the presence of radial and collective expansion in AMPT model. Comparison of $K^0_S K^{\pm}$ and K^+K^- correlations show that the anisotropic flow in both the correlations are comparable to each other. The $\Delta\eta$ correlations of K^+K^- shows dominant contributions from $\Phi(1020)$ meson resonance. Further studies are required to understand the extend and impact of the individual contributions of jets, resonances and flow towards the final shape of the correlations.

Finally, preliminary results from our effort to subtract the contribution of anisotropic flow in case of both $K^0_S K^{\pm}$ and K^+K^- correlations are also included as an outlook. Additionally, the results from rejecting the $\Phi(1020)$ meson resonance contribution in case of K^+K^- correlation function is included.

Chapter 6

Future Studies

Two-particle angular correlation functions are a powerful analytical tool for examining the dynamic evolution of the particle systems produced in high-energy collisions, offering a clear visual representation and the ability to study various physical processes simultaneously. They illustrate how different physics mechanisms combine to influence the final shape of the correlation. However, obtaining magnitude and impact of these individual contributions to the final correlation function can be a challenging process when trying to isolate signals from specific processes like condensate formation. In this chapter, we discuss the preliminary results from our effort to subtract the flow and resonance contributions from the $K^0_S K^{\pm}$ and K^+K^- correlation functions.

As previously observed, both correlation functions exhibit a dominant contribution from anisotropic flow. Notably, elliptic flow, represented as the dominant coefficient in the Fourier expansion that characterizes the azimuthal distribution of particles produced in the collisions. In K^+K^- correlation function, the near-side peak observed contains a major contribution from $\Phi(1020)$ meson resonance and minijets. The of $K^0_S K^{\pm}$ correlation can have contributions from resonances like $f_1(1285)$ and $a_0(980)$. An attempt to subtract flow from both correlations and Φ Meson contributions from K^+K^- correlation is discussed.

6.0.1 Φ Meson Resonance Rejection in K^+K^- Correlation

In this section, we discuss the method for rejecting Φ(1020) meson resonances and present the 2D correlation functions of K^+K^- pairs after this rejection. It was verified by the simulation studies using HIJING model in Section. 4.1.1 that the peak in the near-side region of K^+K^- correlation function is dominantly originating from Φ(1020) resonance that decays to K^+ and K^- with a branching ratio of 48.9 ± 0.5%.

In MC simulations, rejection of all the K^+ and K^- pairs coming from the Φ(1020) resonance is a relatively straightforward task. This is because each particle in the simulation is tagged with a Particle Data Group (PDG) code that identifies its type. To determine if a particle/track comes from the Φ(1020) meson resonance, one can check if it has a parent(mother) track associated with it, and then verify if the PDG code of this parent particle is 333, which corresponds to the Φ(1020) meson resonance.

In the experimental data, the task is not straightforward though it is possible to do the resonance rejection by using invariant mass cut. This approach is similar to calculating the invariant mass of the K^0_S particle, where the invariant mass of a particle is conserved when it decays into other particles. In this case, instead of oppositely charged pions, we have kaons. Using the mass hypothesis for the oppositely charged kaon tracks and their momentum, $m_{K^+K^-}$, invariant mass of the pairs can be calculated. To determine the appropriate invariant mass range for removing the K^+K^- pairs from the correlation, the distribution of the calculated $m_{K^+K^-}$ is filled to a histogram, as shown in Fig. 6.1. From this distribution, it is evident that a range of (1.015, 1.025) GeV/c is optimal for rejecting the pairs. A tighter range would result in not removing enough pairs that may be coming from the Φ(1020) meson resonance decay. Conversely, a looser cut would remove genuine correlations due to other physics mechanisms.

The 2D K^+K^- correlations obtained after the Φ(1020) meson rejection in an invariant

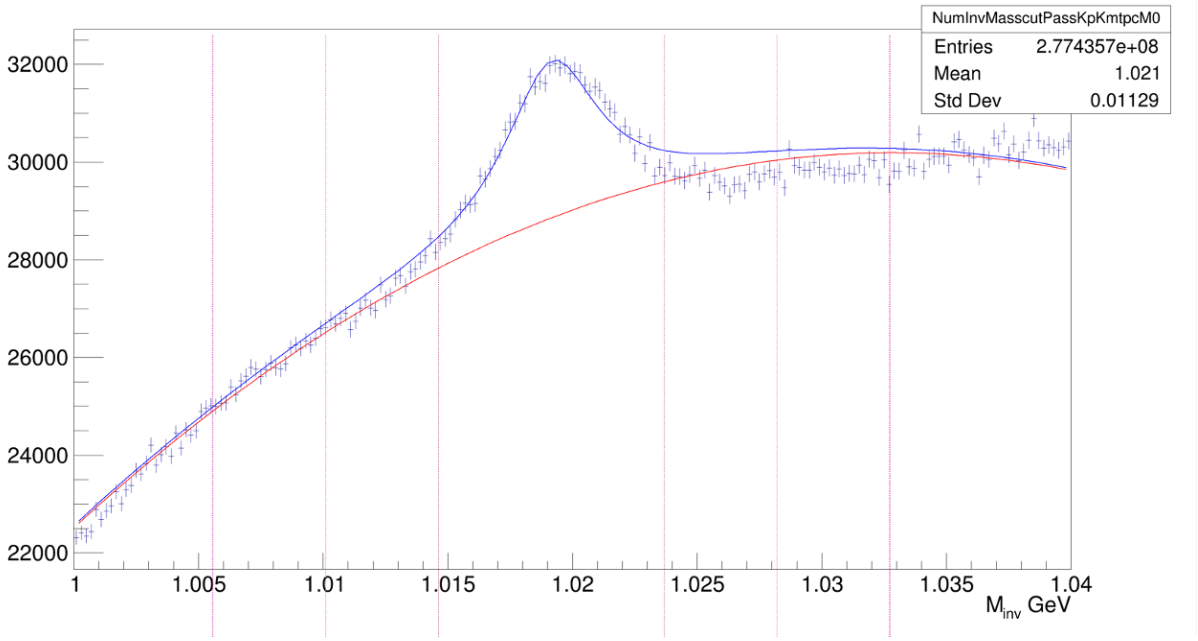

Figure 6.1: Invariant mass of $\Phi(1020)$ meson resonance ($m_{K^+K^-}$) calculated using the K^+K^- pairs using the Pb–Pb collision data at $\sqrt{s_{\rm NN}} = 5.02$ TeV.

mass ($m_{K^+K^-}$) range from 1.015 to 1.025 GeV/c are displayed in Fig.6.2 for 0–10%, 10–30%, 30–50%, and 50–90% centrality intervals. While comparing Fig. 6.2 with Fig. 4.12 which demonstrates the K^+K^- correlation using the same data before $\Phi(1020)$ meson rejection, we see that the peak in the near-side region has disappeared. To determine the range of invariant mass of To understand the magnitude of the $\Phi(1020)$ meson's contribution and the percentage of the peak that is removed, projections of these 2D correlations are taken and displayed in the next section, along with the correlations after flow subtraction.

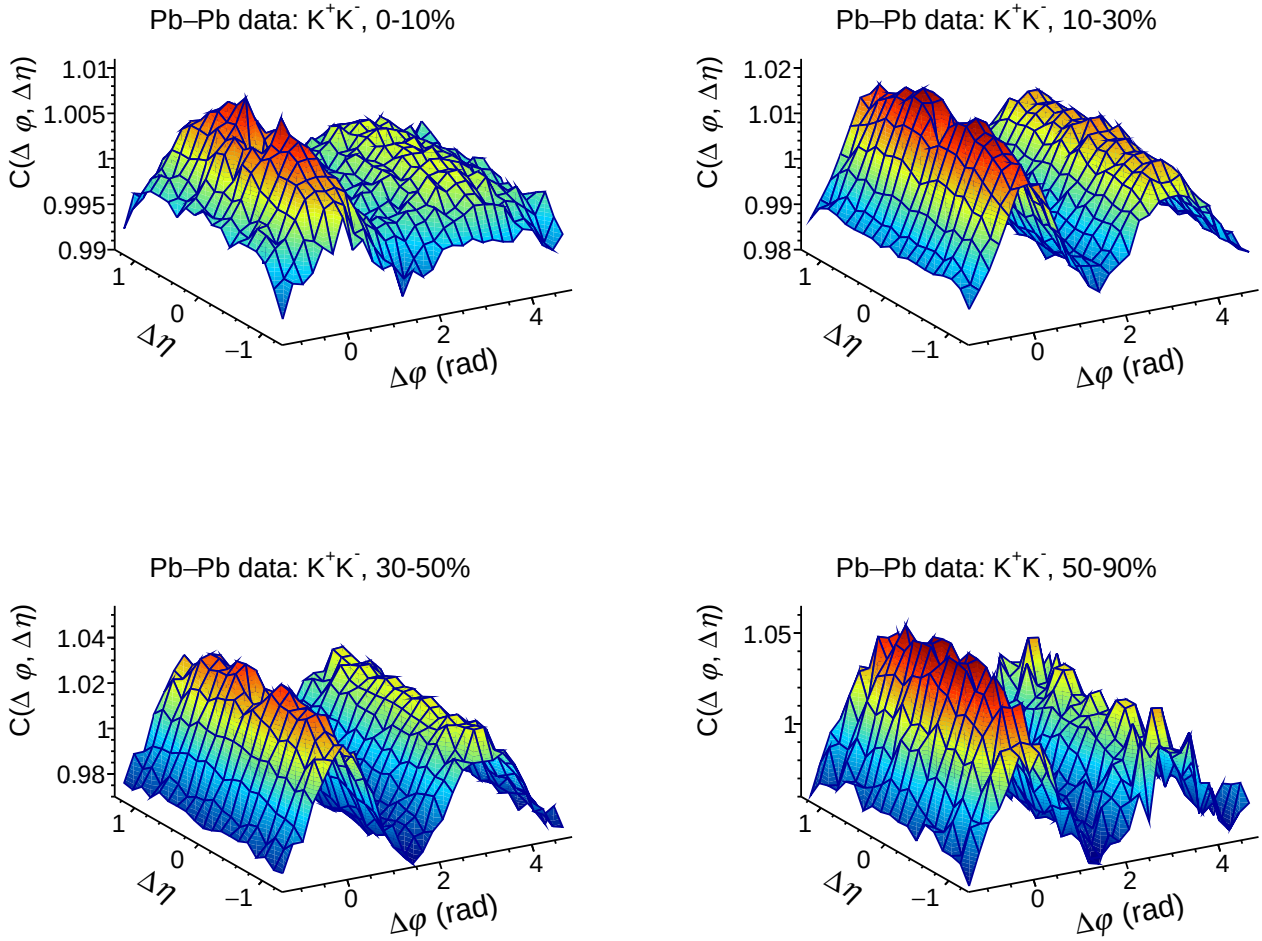

Figure 6.2: The 2D K^+K^- correlation function after the rejection of Φ meson using an invariant mass cut between (1.01, 1.03) GeV/c are displayed for 0–10%, 10–30%, 30–50%, and 50–90% centrality intervals. The correlations are obtained using the Pb–Pb collision data at $\sqrt{s_{\rm NN}} = 5.02$ TeV.

6.0.2 Flow Subtraction in $K^0_S K^{\pm}$ and K^+K^- Correlations

A detailed discussion on collective effects such as anisotropic flow was done in Section 1.4.3. In this section, we discuss the results of removing the anisotropic flow contribution from $K^0_S K^{\pm}$ and K^+K^- Correlations. This is carried out by assuming the flow profile in the correlation to be similar to that of the $\Delta\varphi$ projection taken in large $\Delta\eta$ range and then subtracting this bin by bin from the flow profile in small $\Delta\eta$ range. The intervals of (0.75,1.0) and (0.001,0.3) are used as the large and small $\Delta\eta$ ranges respectively. The subtraction method is verified by doing the same procedure by fitting flow profile in the high $\Delta\eta$ range of the correlation function using the Fourier decomposition of the azimuthal distribution of particles including four Fourier coefficients and subtracting this fit from the $\Delta\varphi$ projection in small $\Delta\eta$ range. The equation for anisotropic flow using a Fourier decomposition of the single particle azimuthal distribution is given below. Here, φ is the azimuthal angle of the emitted particle, and v_n and Ψ_n are the n-th order flow coefficient and flow symmetry-plane angle, respectively.

$$\frac{dN}{d\varphi} \propto 1 + 2\sum_{n=1}^{+\infty} v_n \cos\left[n(\phi - \Psi_n)\right] \tag{6.1}$$

A comparison of the two methods described above for flow subtraction in case of $K^0_S K^{\pm}$ correlation in 0–10% and 10–30% centrality intervals is given in Fig. 6.3. Similarly, the results in 30–50% and 50–90% centrality intervals is given in Fig. 6.4. After the flow contribution is subtracted from the experimental correlation, the distribution is compared to the HIJING model prediction. Black solid and open markers represent the correlations after flow subtraction using method 1 ($\Delta\varphi$ projection taken in large $\Delta\eta$ range is approximated as the description for anisotropic flow)) and method 2 (using Fourier decomposition fit to approximate anisotropic flow). The pink dashed lines are the HIJING model predictions. And square and triangular markers represent the flow profile in small and large $\Delta\eta$ intervals, before the flow subtraction. The same format is used in K^+K^- correlation as well.

A comparison of two methods for flow subtraction performed for K^+K^- correlation in 0–10% and 10–30% centrality intervals is given in Fig. 6.5. And similar results in 30–50% and 50–90% centrality intervals is given in Fig. 6.6. In Fig.6.7, the flow contribution is subtracted from K^+K^- correlations that already includes the $\Phi(1020)$ meson resonance rejection using an invariant mass cut in a range of (1.015,1.025) GeV/c. Additionally for clarity, $K^0_S K^\pm$ correlations after performing flow subtraction (using the second method) in experimental data is compared to the HIJING in all the centrality intervals and are given in Fig. 6.9 and Fig. 6.10. Similar results obtained with K^+K^- correlation are given in Fig. 6.11 and Fig. 6.12. Finally, the results with both flow and $\Phi(1020)$ meson resonance rejection in K^+K^- correlation are given in Fig. 6.13 and Fig. 6.14.

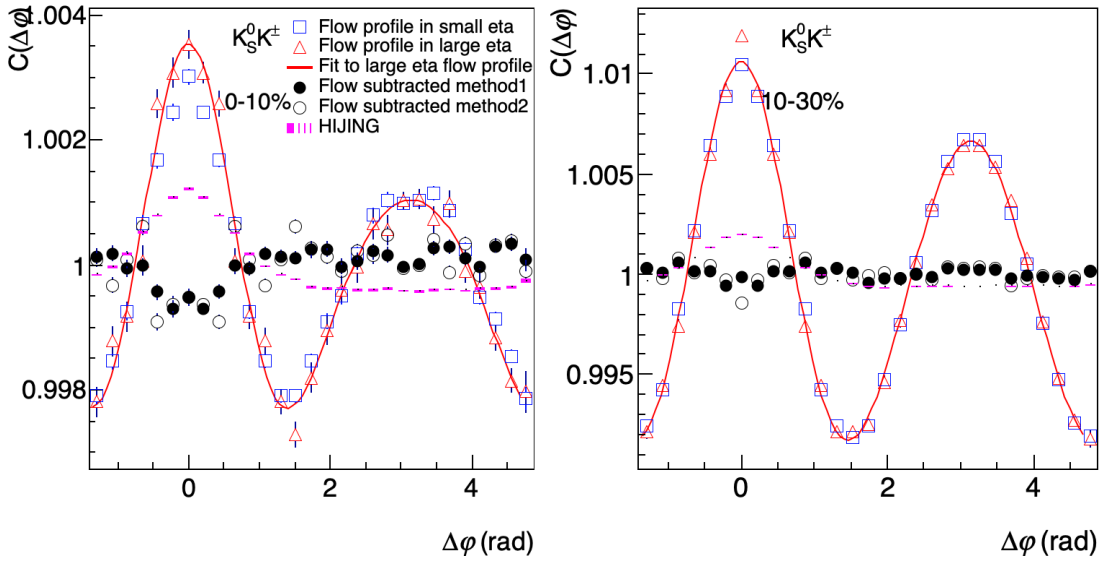

Figure 6.3: The 1D $\Delta\varphi$ $K^0_S K^\pm$ correlation after flow subtraction (black solid and open markers) is compared to HIJING in 0-10% and 10-30% centrality intervals.

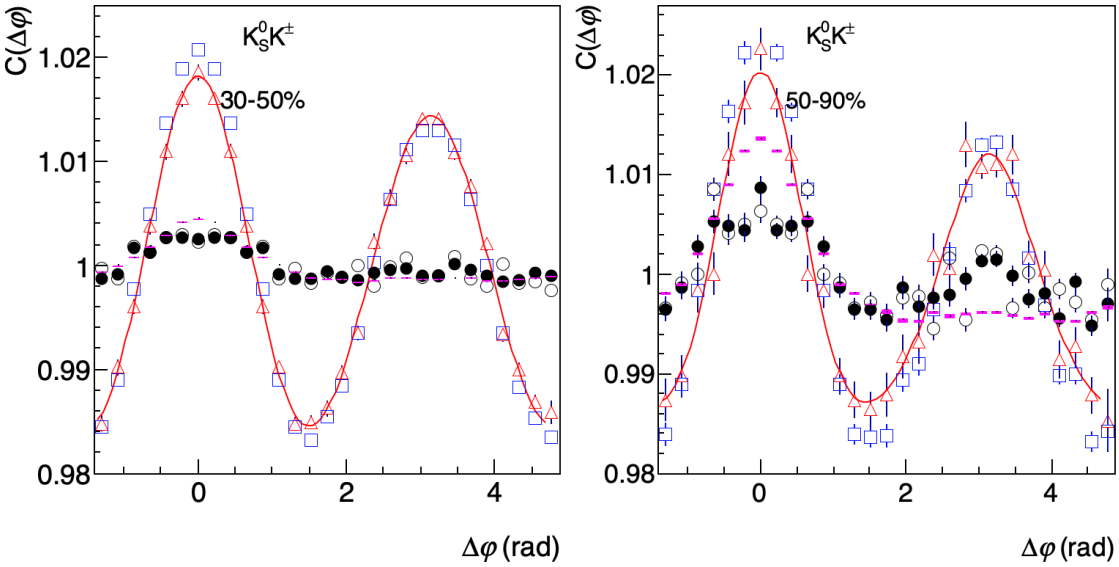

Figure 6.4: The 1D $\Delta\varphi$ $K^0_S K^\pm$ correlation after flow subtraction (black solid and open markers) is compared to HIJING in 30–50% and 50–90% centrality intervals.

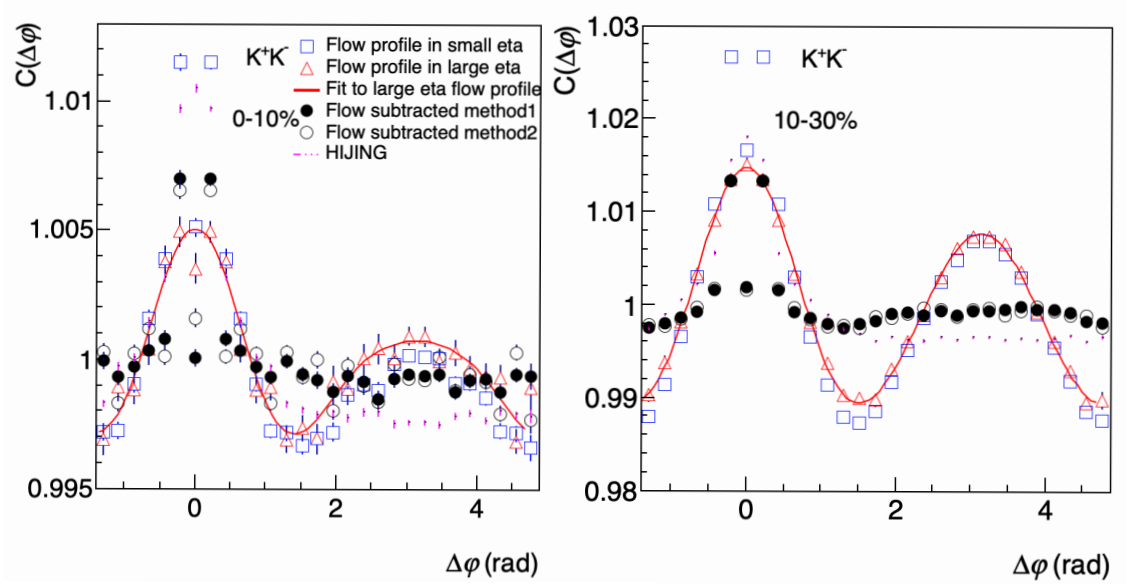

Figure 6.5: The 1D $\Delta\varphi$ K^+K^- correlation after flow subtraction (black solid and open markers) is compared to HIJING model in 0–10%, 10–30% centrality intervals.

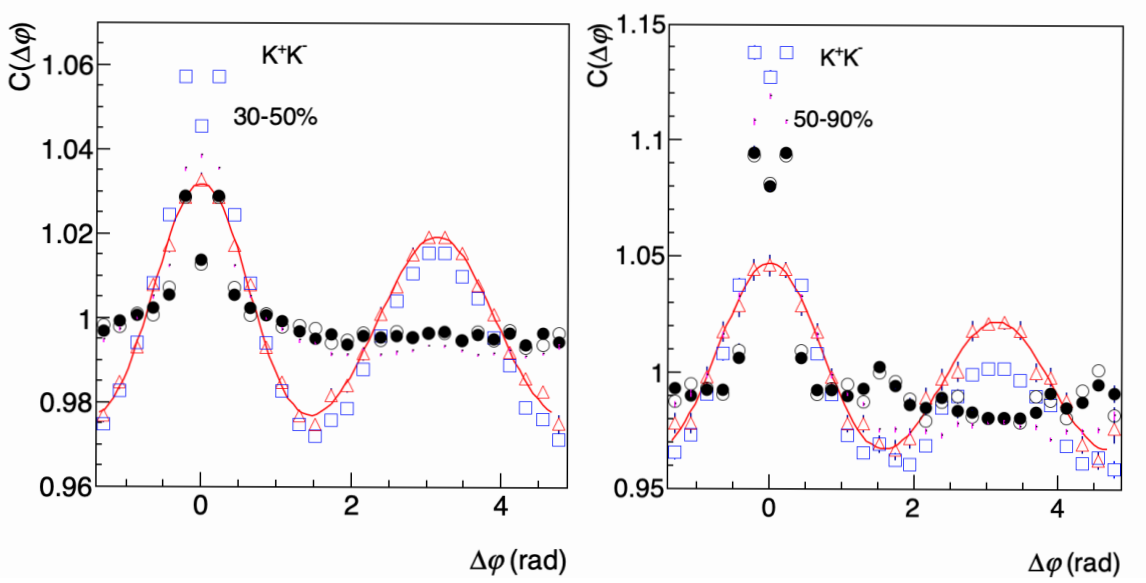

Figure 6.6: The 1D $\Delta\varphi$ K^+K^- correlation after flow subtraction (black solid and open markers) is compared to HIJING model in 30–50% and 50–90% centrality intervals.

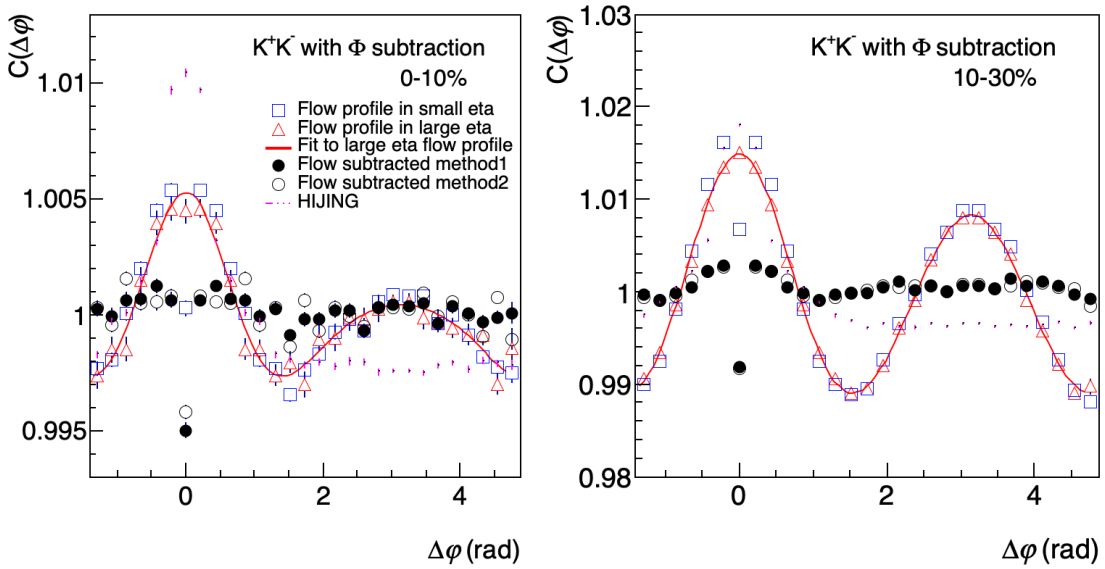

Figure 6.7: The 1D $\Delta\varphi$ K^+K^- correlation after flow and $\Phi(1020)$ meson resonance subtraction (black solid and open markers) is compared to HIJING model in in 0–10% and 10–30% centrality intervals. Note: HIJING data points still contains the contribution from $\Phi(1020)$ meson resonance peak.

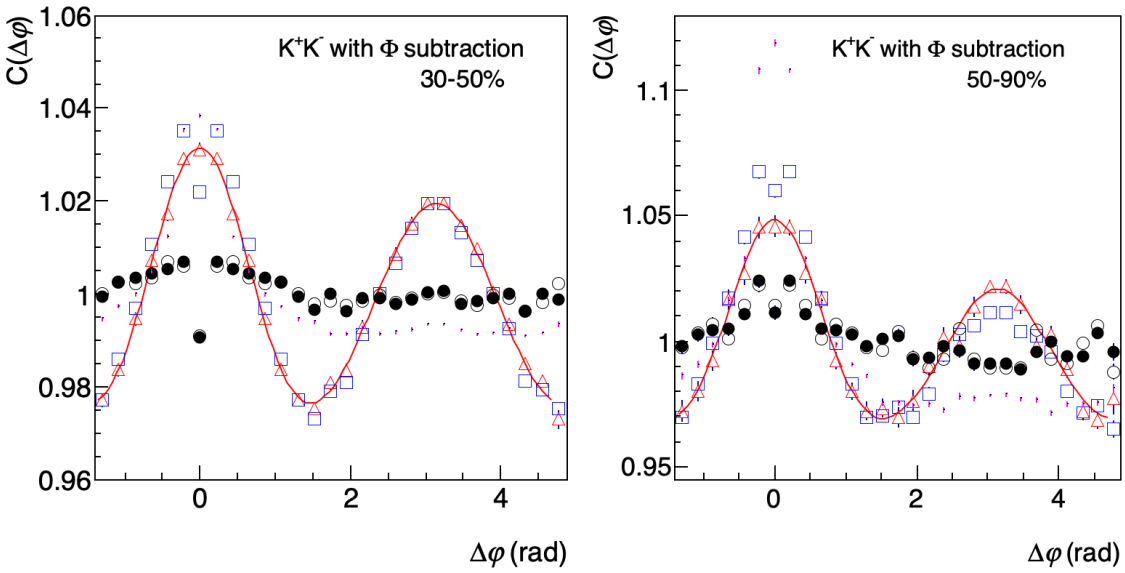

Figure 6.8: The 1D $\Delta\varphi$ K^+K^- correlation after flow and $\Phi(1020)$ meson resonance subtraction (black solid and open markers) is compared to HIJING model in in 30–50% and 50–90% centrality intervals. Note: HIJING data points still contains the contribution from $\Phi(1020)$ meson resonance peak.

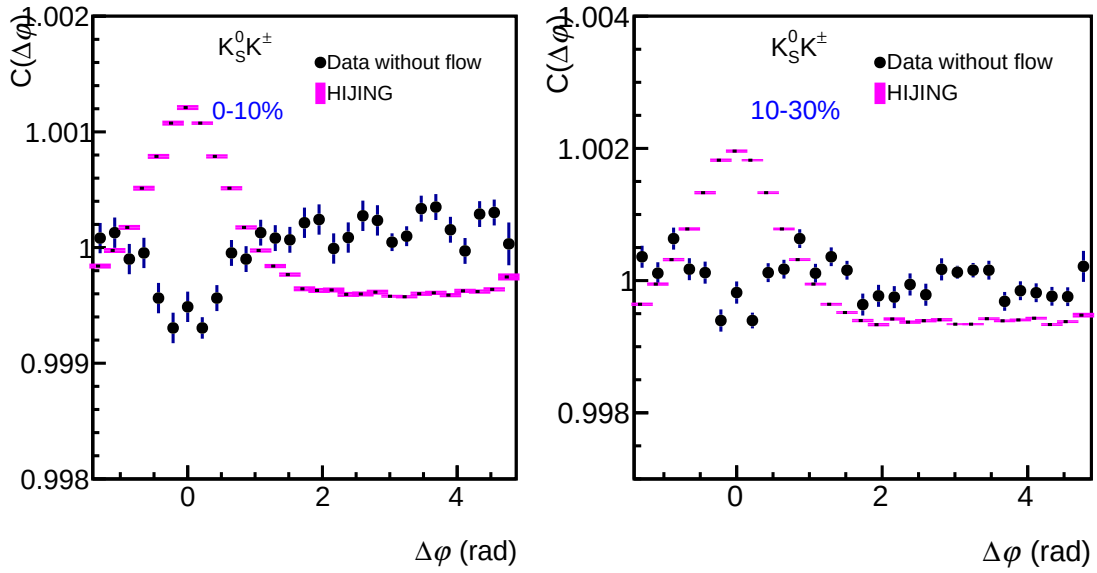

Figure 6.9: The 1D $\Delta\varphi$ $K^0_S K^\pm$ correlation after flow subtraction is compared to HIJING in 0-10% and 10-30% centrality intervals.

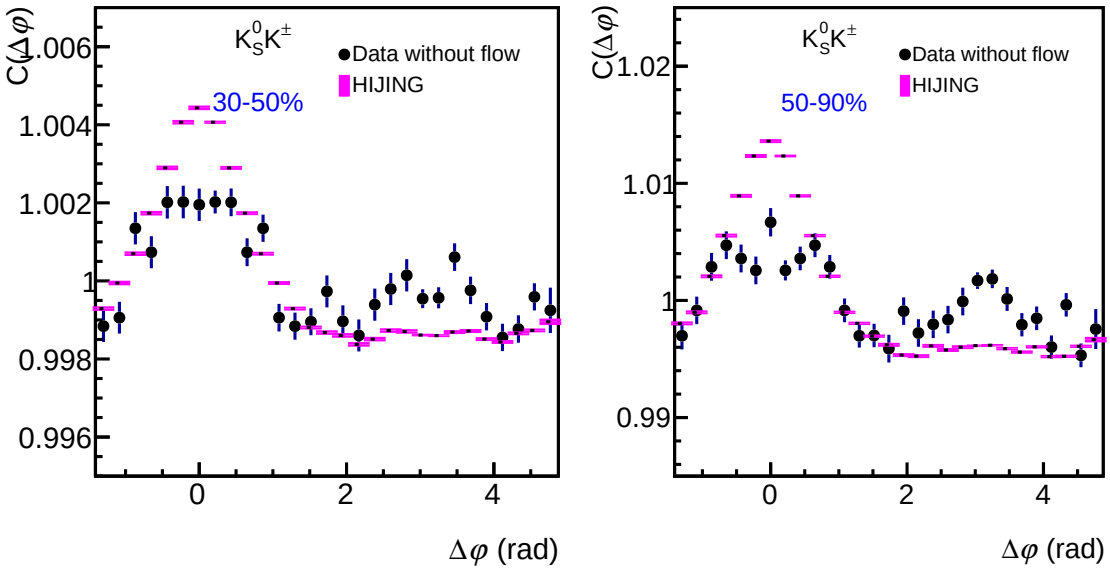

Figure 6.10: The 1D $\Delta\varphi$ $K^0_S K^\pm$ correlation after flow subtraction is compared to HIJING in 30–50% and 50–90% centrality intervals.

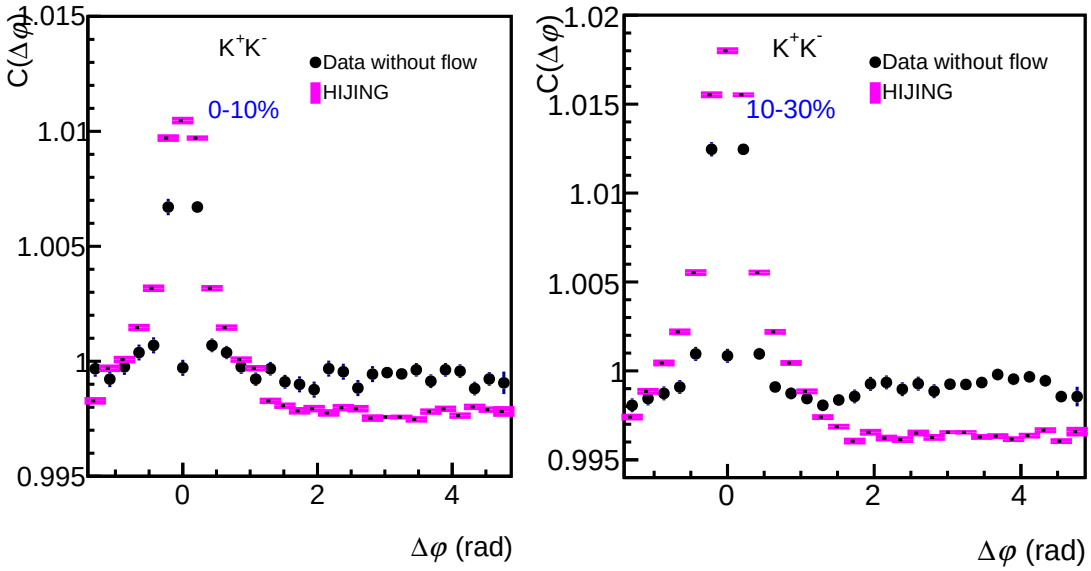

Figure 6.11: The 1D $\Delta\varphi$ K^+K^- correlation after flow subtraction is compared to HIJING model in 0–10%, 10–30% centrality intervals.

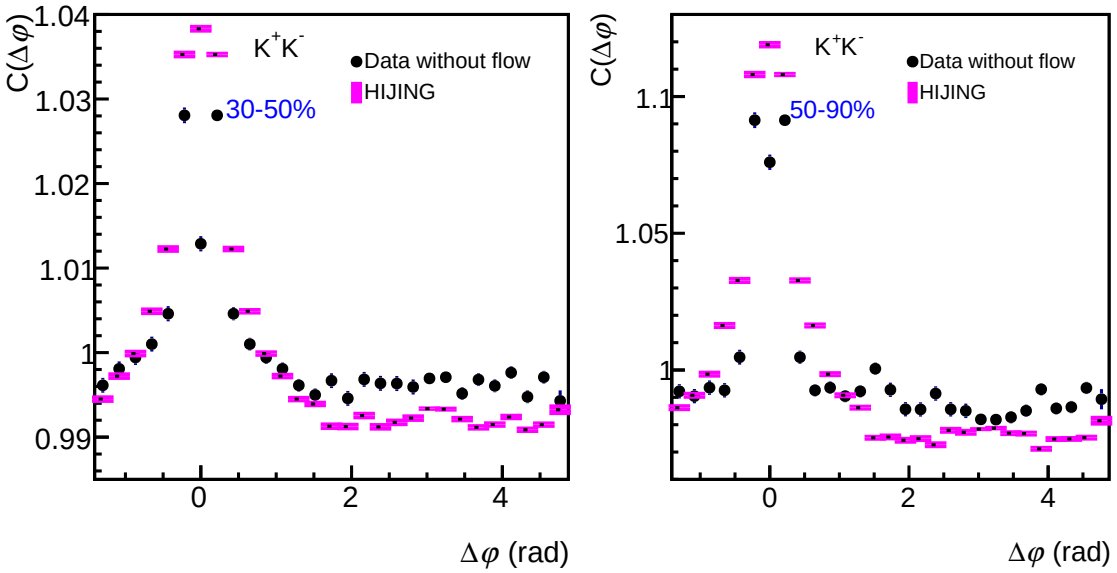

Figure 6.12: The 1D $\Delta\varphi$ K^+K^- correlation after flow subtraction is compared to HIJING model in 30–50% and 50–90% centrality intervals.

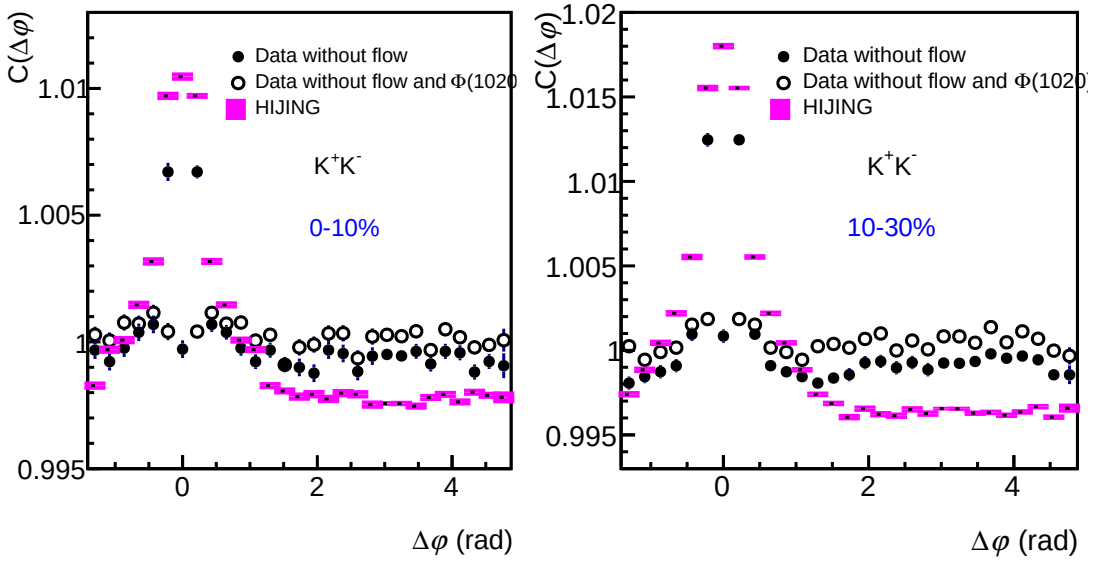

Figure 6.13: The 1D $\Delta\varphi$ K^+K^- correlation after flow and $\Phi(1020)$ meson resonance subtraction is compared to HIJING model in 0–10% and 10–30% centrality intervals. Note: HIJING data points still contains the contribution from $\Phi(1020)$ meson resonance peak.

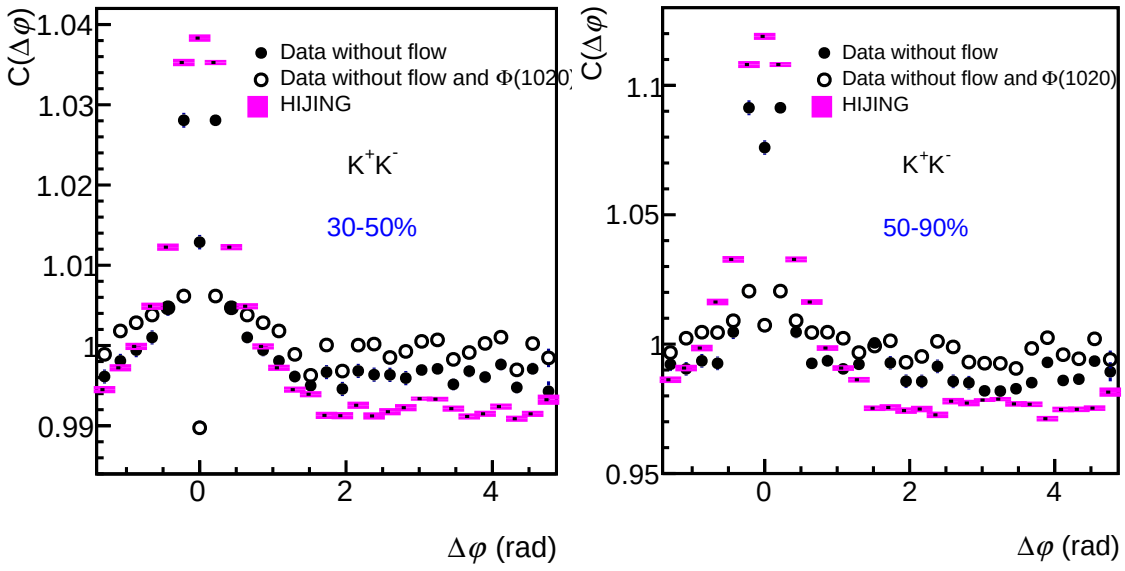

Figure 6.14: The 1D $\Delta\varphi$ K^+K^- correlation after flow and $\Phi(1020)$ meson resonance subtraction is compared to HIJING model in 30–50% and 50–90% centrality intervals. Note: HIJING data points still contains the contribution from $\Phi(1020)$ meson resonance peak.

Bibliography

[1] E. Rutherford. Lxxix. the scattering of α and β particles by matter and the structure of the atom. *Philosophical Magazine Series 6*, 21(125):669–688, May 1911.

[2] H. Geiger and E. Marsden. On a diffuse reflection of the α-particles. *Proceedings of the Royal Society A: Mathematical, Physical and Engineering Sciences*, 82(557):495–500, July 1909.

[3] M. Breidenbach, J. I. Friedman, H. W. Kendall, E. D. Bloom, D. H. Coward, H. DeStaebler, J. Drees, L. W. Mo, and R. E. Taylor. Observed behavior of highly inelastic electron-proton scattering. *Phys. Rev. Lett.*, 23:935–939, Octoberober 1969.

[4] ATLAS Collaboration. Observation of a new particle in the search for the standard model higgs boson with the atlas detector at the lhc. *Physics Letters B*, 716(1):1–29, September 2012.

[5] CDF Collaboration. Observation of top quark production in pbar-p collisions with the collider detector at fermilab. *Physical Review Letters*, 74(14):2626–2631, April 1995.

[6] DONUT Collaboration. Observation of tau neutrino interactions. *Physics Letters B*, 504(3):218–224, April 2001.

[7] H. David Politzer. Reliable perturbative results for strong interactions? *Phys. Rev. Lett.*, 30:1346–1349, June 1973.

[8] David J. Gross and Frank Wilczek. Ultraviolet behavior of non-abelian gauge theories. *Phys. Rev. Lett.*, 30:1343–1346, Juneee 1973.

[9] Alexandre Deur, Stanley J. Brodsky, and Guy F. de Téramond. The qcd running coupling. *Progress in Particle and Nuclear Physics*, 90:1–74, September 2016.

[10] S. Bethke. Experimental tests of asymptotic freedom. *Progress in Particle and Nuclear Physics*, 58(2):351–386, April 2007.

[11] Siegfried Bethke. World summary of $\alpha_s(2012)$. *Nuclear Physics B - Proceedings Supplements*, 234:229–234, January 2013.

[12] Raghunath Sahoo and Tapan Nayak. Possible early universe signals in proton collisions at the large hadron collider. 01 2022.

[13] Christian S. Fischer. Qcd at finite temperature and chemical potential from dyson–schwinger equations. *Progress in Particle and Nuclear Physics*, 105:1–60, 2019.

[14] Y. Aoki, G. Endrődi, Z. Fodor, S. D. Katz, and K. K. Szabó. The order of the quantum chromodynamics transition predicted by the standard model of particle physics. *Nature*, 443(7112):675–678, 2006.

[15] R. Bellwied, S. Borsanyi, Z. Fodor, J. Günther, S. D. Katz, C. Ratti, and K. K. Szabo. The qcd phase diagram from analytic continuation. *Physics Letters B*, 751:559–564, December 2015.

[16] M. A. Stephanov. Qcd phase diagram: an overview, 2006. `https://arxiv.org/abs/hep-lat/0701002`.

[17] M. Stephanov, K. Rajagopal, and E. Shuryak. Signatures of the tricritical point in qcd. *Physical Review Letters*, 81(22):4816–4819, November 1998.

[18] M. A. Halasz, A. D. Jackson, R. E. Shrock, M. A. Stephanov, and J. J. M. Verbaarschot. Phase diagram of qcd. *Physical Review D*, 58(9), September 1998.

[19] Adam Bzdak, ShinIchi Esumi, Volker Koch, Jinfeng Liao, Mikhail Stephanov, and Nu Xu. Mapping the phases of quantum chromodynamics with beam energy scan. *Physics Reports*, 853:1–87, April 2020.

[20] Szabolcs Borsányi, Gergely Endrődi, Zoltán Fodor, Antal Jakovác, Sándor D. Katz, Stefan Krieg, Claudia Ratti, and Kálmán K. Szabó. The qcd equation of state with dynamical quarks. *Journal of High Energy Physics*, 2010(11), November 2010.

[21] A. Bazavov and *et al.* Equation of state in (2+1)-flavor qcd. *Physical Review D*, 90(9), November 2014.

[22] Berndt Müller and Andreas Schäfer. Why does the thermal model for hadron production in heavy ion collisions work? *arXiv*, December 2018.

[23] Alessandro Lovato et al. Long Range Plan: Dense matter theory for heavy-ion collisions and neutron stars. 11 2022.

[24] Sidney Coleman. *Aspects of Symmetry: Selected Erice Lectures*. Cambridge University Press, 1985.

[25] Volker Koch. Aspects of chiral symmetry. *International Journal of Modern Physics E*, 06(02):203–249, 1997.

[26] H. Sazdjian. Introduction to chiral symmetry in qcd. *EPJ Web of Conferences*, 137:02001, 2017.

[27] Y. Nambu and G. Jona-Lasinio. Dynamical model of elementary particles based on an analogy with superconductivity. i. *Phys. Rev.*, 122:345–358, Apr 1961.

[28] Peter W. Higgs. Broken Symmetries and the Masses of Gauge Bosons. *Phys. Rev. Lett.*, 13:508–509, 1964.

[29] J. Goldstone. Field Theories with Superconductor Solutions. *Nuovo Cim.*, 19:154–164, 1961.

[30] Murray Gell-Mann. A Schematic Model of Baryons and Mesons. *Phys. Lett.*, 8:214–215, 1964.

[31] Harald Fritzsch and Murray Gell-Mann. Current Algebra: Quarks and What Else? In J. D. Jackson and A. Roberts, editors, *Proceedings of the XVI International Conference on High Energy Physics, Chicago-Batavia, 1972*, pages 135–165. NAL, 1972.

[32] Arno A. Penzias and Robert G. Wilson. A measurement of excess antenna temperature at 4080-mc/s. *The Astrophysical Journal*, 142:419–421, 1965.

[33] Robert V. Wagoner, William A. Fowler, and F. Hoyle. On the Synthesis of Elements at Very High Temperatures. , 148:3, April 1967.

[34] J. Richard Bond, Lev Kofman, and Dmitry Pogosyan. How filaments of galaxies are woven into the cosmic web. , 380(6575):603–606, April 1996.

[35] Edwin Hubble. A Relation between Distance and Radial Velocity among Extra-Galactic Nebulae. *Proceedings of the National Academy of Science*, 15(3):168–173, March 1929.

[36] I. Arsene and et al. Quark–gluon plasma and color glass condensate at rhic? the perspective from the brahms experiment. *Nuclear Physics A*, 757(1–2):1–27, August 2005.

[37] J. Adams and month=aug pages=102–183 et al, year=2005. Experimental and theoretical challenges in the search for the quark–gluon plasma: The star collaboration's critical assessment of the evidence from rhic collisions. *Nuclear Physics A*, 757(1–2).

[38] B.B. Back and et al. The phobos perspective on discoveries at rhic. *Nuclear Physics A*, 757(1–2):28–101, August 2005.

[39] K. Adcox and et al. Formation of dense partonic matter in relativistic nucleus–nucleus collisions at rhic: Experimental evaluation by the phenix collaboration. *Nuclear Physics A*, 757(1–2):184–283, August 2005.

[40] ALICE Collaboration. The alice experiment – a journey through qcd, 2022.

[41] Johann Rafelski and Berndt Müller. Strangeness production in the quark-gluon plasma. *Phys. Rev. Lett.*, 48:1066–1069, Apr 1982.

[42] ALICE Collaboration. Enhanced production of multi-strange hadrons in high-multiplicity proton–proton collisions. *Nature Physics*, 13(6):535–539, April 2017.

[43] ALICE Collaboration. Multi-strange baryon production at mid-rapidity in pb–pb collisions at at $\sqrt{S_{NN}} = 2.76$ tev. *Physics Letters B*, 728:216–227, January 2014.

[44] Jean-Yves Ollitrault. Anisotropy as a signature of transverse collective flow. *Phys. Rev. D*, 46:229–245, Jul 1992.

[45] Ulrich Heinz and Raimond Snellings. Collective flow and viscosity in relativistic heavy-ion collisions. *Annual Review of Nuclear and Particle Science*, 63(1):123–151, 2013.

[46] Roman Pasechnik and Michal Šumbera. Phenomenological review on quark–gluon plasma: Concepts vs. observations. *Universe*, 3(1), 2017.

[47] S. Voloshin and Y. Zhang. Flow study in relativistic nuclear collisions by fourier expansion of azimuthal particle distributions. *Zeitschrift for Physik C Particles and Fields*, 70(4):665–671, May 1996.

[48] STAR Collaboration. Particle-type dependence of azimuthal anisotropy and nuclear modification of particle production in Au + Au collisions at $\sqrt{s_{NN}} = 200$ GeV. *Phys. Rev. Lett.*, 92:052302, Feb 2004.

[49] ALICE Collaboration. Elliptic flow of identified hadrons in pb–pb collisions at $\sqrt{S_{NN}} = 2.76$ tev. *Journal of High Energy Physics*, 2015(6):1–41, 2015.

[50] ALICE Collaboration. Higher harmonic anisotropic flow measurements of charged particles in pb-pb collisions at $\sqrt{S_{NN}} = 2.76$ tev. *Physical Review Letters*, 107(3), July 2011.

[51] Shreyasi Acharya and *et al.* Neutral to charged kaon yield fluctuations in pb–pb collisions at $\sqrt{S_{NN}} = 2.76$ tev. *Physics Letters B*, 832:137242, September 2022.

[52] Sean Gavin and Joseph I. Kapusta. Kaon and pion fluctuations from small disoriented chiral condensates. *Physical Review C*, 65(5), May 2002.

[53] C. Pruneau, S. Gavin, and S. Voloshin. Methods for the study of particle production fluctuations. *Phys. Rev. C*, 66:044904, October 2002.

[54] B. Mohanty and J. Serreau. Disoriented chiral condensate: Theory and experiment. *Physics Reports*, 414(6):263–358, 2005.

[55] Jean-Paul Blaizot and André Krzywicki. Dynamics of a disoriented chiral condensate. *Physical Review D*, 50(1):442–446, 1994.

[56] Jean-Paul Blaizot and Andre Krzywicki. Soft pion emission in high-energy heavy ion collisions. *Phys. Rev. D*, 46:246–251, 1992.

[57] J. D. Bjorken. Disoriented chiral condensate. *SLAC-PUB-6488*, 1994.

[58] J. D. Bjorken. T864 (minimax): A search for disoriented chiral condensate at the fermilab collider, October 1996.

[59] C. R. A. Augusto, S. L. C. Barroso, V. Kopenkin, M. Moriya, C. E. Navia, and E. H. Shibuya. Observation of centauro events in cosmic rays. *Physical Review D*, 59(5):054001, 1999.

[60] Ewa Gladysz-Dziadus. Are centauros exotic signals of the qgp?, 2012.

[61] C. M. G. Lattes, Y. Fujimoto, and S. Hasegawa. Hadronic interactions of high energy cosmic-ray observed by emulsion chambers. , 65(3):151–229, 1980.

[62] Julien Serreau. Disoriented chiral condensate formation in heavy ion collisions?, 2003.

[63] Krishna Rajagopal and Frank Wilczek. Static and dynamic critical phenomena at a second order qcd phase transition. *Nuclear Physics B*, 399(2–3):395–425, July 1993.

[64] J. Schaffner-Bielich and J. Randrup. Disoriented chiral condensate dynamics with the su(3) linear sigma model. *Physical Review C*, 59(6):3329–3342, June 1999.

[65] STAR Collaboration, L. Adamczyk, and et al. Charged-to-neutral correlation at forward rapidity in au+au collisions at $\sqrt{s_{NN}} = 200$ gev. *Physical Review C*, 91(3):034905, 2015.

[66] Ranjit Nayak. *Event-by-event Fluctuations of Charged and Neutral Kaons in Pb-Pb collisions at $\sqrt{s_{NN}} = 2.76$ TeV with ALICE at the LHC*. PhD thesis, 2020.

[67] Joseph I. Kapusta, Scott Pratt, and Mayank Singh. Confronting anomalous kaon correlations measured in pb-pb collisions at $\sqrt{s_{NN}} = 2.76$ tev. *Phys. Rev. C*, 107:014913, Jan 2023.

[68] Joseph I. Kapusta, Scott Pratt, and Mayank Singh. Disoriented isospin condensates may be the source of anomalous kaon correlations measured in pb-pb collisions at $\sqrt{s_{NN}} = 2.76$ tev. *Phys. Rev. C*, 109:L031902, Mar 2024.

[69] Ranjit Nayak, Sadhana Dash, Basanta Kumar Nandi, and Claude Pruneau. Modeling of charged kaon and neutral kaon fluctuations as a signature for the production of a disoriented chiral condensate in $a - a$ collisions. *Phys. Rev. C*, 101:054904, May 2020.

[70] A. Bazavov, T. Bhattacharya, M. Cheng, C. DeTar, H.-T. Ding, Steven Gottlieb, R. Gupta, P. Hegde, U. M. Heller, F. Karsch, E. Laermann, L. Levkova, S. Mukherjee,

P. Petreczky, C. Schmidt, R. A. Soltz, W. Soeldner, R. Sugar, D. Toussaint, W. Unger, and P. Vranas. Chiral and deconfinement aspects of the qcd transition. *Physical Review D*, 85(5), March 2012.

[71] J. Adam and et al. Insight into particle production mechanisms via angular correlations of identified particles in pp collisions at $\sqrt{s_{NN}} = 7$ tev. *The European Physical Journal C*, 77(8), August 2017.

[72] B. Alver et al. System size dependence of cluster properties from two-particle angular correlations in cu+cu and au+au collisions at $\sqrt{s_{NN}} = 200$GeV. *Physical Review C*, 81(2):024904, February 2010.

[73] B. I. Abelev et al. Long range rapidity correlations and jet production in high energy nuclear collisions. *Physical Review C*, 80(6):064912, December 2009.

[74] B. Alver et al. High transverse momentum triggered correlations over a large pseudo-rapidity acceptance in au+au collisions at $\sqrt{s_{NN}} = 200$GeV. *Physical Review Letters*, 104(6):062301, February 2010.

[75] V. Khachatryan et al. Observation of long-range near-side angular correlations in proton-proton collisions at the lhc. *Journal of High Energy Physics*, 09(091), September 2010.

[76] Measurements of long-range azimuthal anisotropies and associated fourier coefficients for pp collisions at $\sqrt{s} = 5.02$ and 13 tev and p+pb collisions at $\sqrt{s_{NN}} = 5.02$ tev with the atlas detector. *Phys. Rev. C*, 96:024908, Aug 2017.

[77] S. Chatrchyan et al. Long-range and short-range dihadron angular correlations in central pbpb collisions at a nucleon-nucleon center of mass energy of 2.76 tev. *Journal of High Energy Physics*, 07, July 2011.

[78] G. Aad et al. Observation of associated near-side and away-side long-range correlations in $\sqrt{s_{NN}} = 5.02$TeV Proton-Lead Collisions with the ATLAS Detector. *Physical Review Letters*, 110(18):182302, May 2013.

[79] G. Aad et al. Measurement of long-range pseudorapidity correlations and azimuthal harmonics in $\sqrt{s_{NN}} = 5.02$TeV proton-lead collisions with the ATLAS detector. *Physical Review C*, 90(4):044906, 2014.

[80] S. Chatrchyan et al. Centrality dependence of dihadron correlations and azimuthal anisotropy harmonics in pbpb collisions at $\sqrt{s_{NN}} = 2.76$TeV. *European Physical Journal C*, C72:2012, November 2012.

[81] S. Chatrchyan et al. Observation of long-range near-side angular correlations in proton-lead collisions at the lhc. *Physics Letters B*, B718:795–814, January 2013.

[82] V. Khachatryan et al. Evidence for collectivity in pp collisions at the lhc. *Physics Letters B*, B765:193–220, February 2017.

[83] K. Aamodt et al. The ALICE experiment at the CERN LHC. *JINST*, 3:S08002, 2008.

[84] Julie Haffner. The cern accelerator complex. complexe desaccélérateurs du cern. 2013.

[85] Mattia Faggin. Vertexing detectors and vertexing performance in run 2 in alice, 2020.

[86] G. Dellacasa et al. ALICE: Technical design report of the time projection chamber. 1 2000.

[87] G. Dellacasa et al. ALICE technical design report of the time-of-flight system (TOF). 2 2000.

[88] P Cortese et al. ALICE technical design report on forward detectors: FMD, T0 and V0. 9 2004.

[89] The ALICE collaboration. Performance of the alice vzero system. *Journal of Instrumentation*, 8(10):P10016, October 2013.

[90] Performance of the alice experiment at the cern lhc. *International Journal of Modern Physics A*, 29(24):1430044, September 2014.

[91] `https://github.com/asasikum/AliPhysics`.

[92] `https://github.com/alisw/AliRoot`.

[93] Markus for the ALICE Collaboration Zimmermann. The ALICE analysis train system. *J. Phys.: Conf. Ser.*, 608(1):012019, 2015.

[94] M. Maire A.C. McPherson P. Zanarini R. Brun, F. Bruyant. The GEANT3 electromagnetic shower program and a comaprison with a EGS3 code, 1985.

[95] S. Agostinelli et al. GEANT4–a simulation toolkikt. *Nucl. Instrum. Methods Phys. Res., A*, 506(3):250–303, 2003.

[96] B Pastirčák. Fluka monte carlo simulation code as used for radiation studies in the ALICE experiment. *Phys. Part. Nuclei Lett. 5, 301–304*, 2008.

[97] F. Carminati and A. Morsch. Simulation in ALICE, 2003.

[98] Xin-Nian Wang and Miklos Gyulassy. hijing: A monte carlo model for multiple jet production in pp, pA, and AA collisions. *Phys. Rev. D*, 44:3501–3516, Dec 1991.

[99] Miklos Gyulassy and Xin-Nian Wang. Hijing 1.0: A monte carlo program for parton and particle production in high energy hadronic and nuclear collisions. *Computer Physics Communications*, 83(2–3):307–331, December 1994.

[100] Gábor Bíró, Gergely Gábor Barnaföldi, Gábor Papp, Miklos Gyulassy, Péter Lévai, Xin-Nian Wang, and Ben-Wei Zhang. Introducing hijing++: the heavy ion monte carlo generator for the high-luminosity lhc era, 2019.

[101] Bin Zhang, Che Ming Ko, Bao-An Li, and Ziwei Lin. A transport model for heavy ion collisions at rhic, 1999.

[102] Bin Zhang. Zpc 1.0.1: a parton cascade for ultrarelativistic heavy ion collisions. *Computer Physics Communications*, 109(2–3):193–206, April 1998.

[103] Zi-Wei Lin, Che Ming Ko, Bao-An Li, Bin Zhang, and Subrata Pal. Multiphase transport model for relativistic heavy ion collisions. *Physical Review C*, 72(6), December 2005.

[104] Roger Barlow. Systematic errors: facts and fictions, 2002.

[105] Neelkamal Mallick, Suraj Prasad, Aditya Nath Mishra, Raghunath Sahoo, and Gergely Gábor Barnaföldi. Deep learning predicted elliptic flow of identified particles in heavy-ion collisions at the rhic and lhc energies. *Physical Review D*, 107(9), May 2023.